

AN ABSTRACT OF THE DISSERTATION OF

Rawley Brandon Greene for the degree of Doctor of Philosophy in Materials Science
presented on September 6, 2012.

Title: Fatigue Reliability Predictions in Silicon Nitride Ceramics Based on Fatigue
Behavior, Bridging Stresses and Fracture Data

Abstract approved:

Jamie J. Kruzic

Because of its attractive material properties like high hardness, high toughness, and excellent high temperature strength, materials like silicon nitride are becoming more common for use in high performance applications. However, there have been limited studies of the fatigue behavior of small cracks in silicon nitride and other materials toughened by grain bridging mechanisms. This study explores using micro-Raman spectroscopy, fatigue crack growth data and results from static fracture experiments to determine a bridging stress profile for silicon nitride doped with MgO and Y_2O_3 as sintering additives. These bridging stress profiles allow for the creation of a geometry specific fatigue threshold R-curve which can be used to develop a fatigue endurance strength prediction tool to aid in the design of products using the material. Cyclical fatigue experiments conducted on bend beams with induced semi-elliptical surface cracks were conducted to verify the prediction tool. The results show that no bend beams with this crack geometry failed below the predicted endurance

level. It is expected that this method can be extended to create fatigue endurance strength predictions for other materials similarly toughened by grain bridging and other mechanisms.

©Copyright by Rawley Brandon Greene
Septmber 6, 2012
All Rights Reserved

Fatigue Reliability Predictions in Silicon Nitride Ceramics Based on Fatigue Behavior,
Bridging Stresses and Fracture Data

by
Rawley Brandon Greene

A DISSERTATION

submitted to

Oregon State University

in partial fulfillment of
the requirements for the
degree of

Doctor of Philosophy

Presented September 6, 2012
Commencement June 2013

Doctor of Philosophy dissertation of Rawley Brandon Greene presented on September 6, 2012.

APPROVED:

Major Professor, representing Materials Science

Director of the Materials Science Graduate Program

Dean of the Graduate School

I understand that my dissertation will become part of the permanent collection of Oregon State University libraries. My signature below authorizes release of my dissertation to any reader upon request.

Rawley Brandon Greene, Author

ACKNOWLEDGEMENTS

The author expresses sincere appreciation to the following individuals for their support: Jamie J. Kruzic for his advising, knowledge and experience and giving me the opportunity to work with him these past years. Joel Ager for help with Raman spectroscopy experiments and the use of his lab facilities. Sarah Gallops for starting out on this journey together and helping each other through with our own strengths. Nate Stout, Linden Wood, Chad Fell, and Amber Walker for being awesome friends and band-mates. Kathleen Stevens Prudell for being my oldest friend in the area and being the most difficult student I've ever had. Will Beatie for LabView assistance. Ram Ravichandran for assistance with absorption measurements. The Materials Science faculty for random assistance here and there and putting up with me. Also the MIME staff for putting up with me. All my friends for their support and general distraction from school. My mom, and family for their never ending support emotionally and of course financially.

The author would also like to express the utmost appreciation to the National Science Foundation who funded this research under CAREER Award No. 0547394.

CONTRIBUTION OF AUTHORS

Dr. Jamie J. Kruzic wrote the proposal that funded this research. He conceived of this study, provided bridging stress data from a previous study, and supplied interpretation of the data and overall guidance.

Dr. Theo Fett calculated bridging stresses and the R-curves from experimental data collected.

Dr. Stefan Fünfschilling measured the static fracture R-curve for silicon nitride, supplied micrographs of the material and also calculated grain-size distributions in silicon nitride.

Dr. Joel W. Ager III allowed for use of his lab and spectroscopy equipment to conduct the micro-Raman spectroscopy measurements. He offered guidance on spectroscopy data analysis and determination of Raman sampling volume.

TABLE OF CONTENTS

	<u>Page</u>
1 Introduction	1
2 Background.....	3
2.1 Silicon Nitride.....	3
2.1.1 Material Properties	5
2.1.2 Material Synthesis.....	6
2.1.3 Material Processing.....	8
2.1.4 Material Applications.....	11
2.1.5 Material Summary.....	13
2.2 Fracture Mechanics	14
2.2.1 Fracture Mechanics Basics.....	14
2.2.2 Toughening Mechanisms	15
2.2.3 Bridging Stress Distributions	16
2.2.4 Resistance Curves	17
2.2.5 Crack Growth Behavior in Silicon Nitride	20
2.3 Fatigue.....	21
2.3.1 Fatigue Threshold R-Curves	22
2.3.2 Behavior of Fatigue Crack Growth in Silicon Nitride	22
2.4 Micro-Raman Spectroscopy.....	23
3 Fatigue crack growth of Si ₃ N ₄ : Roles of grain aspect ratio and intergranular film composition.....	26
3.1 Abstract.....	26
3.2 Introduction	26
3.3 Procedures	29
3.3.1 Materials.....	29

TABLE OF CONTENTS (Continued)

	<u>Page</u>
3.3.2 Fatigue crack growth testing	30
3.4 Results	33
3.5 Discussion	38
3.5.1 Normalization and comparison of data	38
3.5.2 Role of Grain Morphology	40
3.5.3 Role of Intergranular Film	42
3.6 Conclusions	45
4 A direct comparison of non-destructive techniques for determining bridging stress distributions	47
4.1 Abstract	47
4.2 Introduction	48
4.3 Experimental Methods	54
4.3.1 Materials	54
4.3.2 Bridging stresses from crack opening displacements (CODs)	55
4.3.3 Fatigue threshold experiments	56
4.3.4 Spectroscopy	57
4.4 Results	62
4.4.1 Bridging stresses from crack opening displacements and R-curves (Si ₃ N ₄)	62
4.4.2 Fatigue crack bridging stress results (Si ₃ N ₄)	63
4.4.3 Estimating the fatigue threshold bridging stress distribution for Si ₃ N ₄	65
4.4.4 Sampling volume results	67
4.5 Discussion	69
4.5.1 Effect of the free surface	69
4.5.2 Effect of the T-stress and sample geometry	71
4.5.3 Bridging stresses from spectroscopy methods	78

TABLE OF CONTENTS (Continued)

	<u>Page</u>
4.5.4 Deducing the fatigue bridging stress distribution	81
4.6 Conclusions	82
5 Fatigue Endurance Strength Predictions for Silicon Nitride and Materials Toughened by Grain Bridging Mechanisms.....	86
5.1 Abstract.....	86
5.2 Introduction	86
5.3 Procedure	92
5.3.1 Material	92
5.3.2 Sample Preparation	92
5.3.3 Crack Measurement	93
5.3.4 Endurance Prediction Curve	93
5.3.5 Loading Determination	96
5.3.6 Cyclical Fatigue Experiments	97
5.3.7 Examination of crack shape post-failure.....	97
5.4 Results.....	99
5.4.1 Verifications.....	100
5.4.2 Crack Shape Analysis	101
5.5 Discussion.....	104
5.6 Conclusion.....	106
6 Summary.....	108
7 References	110

LIST OF FIGURES

<u>Figure</u>	<u>Page</u>
Figure 2.1 SEM micrograph of Si_3N_4 elongated grains. Used with permission from Springer.[13]	3
Figure 2.2 Crystal structures of alpha and beta silicon nitride. Used with permission from Wiley.[14].....	4
Figure 2.3: Effect of crack length on the applied stress intensity factor, K_{app}	14
Figure 2.4: Schematic of grain bridging.	15
Figure 2.5: Bridging stress distribution.....	16
Figure 2.6: Process for determining K_{br} from the bridging stress distribution.	18
Figure 2.7: Effect of K_{br} on K_{tip}	19
Figure 2.8: Schematic of an R-Curve demonstrating increased toughness over a non-toughened material.	19
Figure 2.9: Crack extension appearing in the “matrix” material: (a) crack extension with pinning at individual $\beta\text{-Si}_3\text{N}_4$ grains,(b) crack-front dissolution in the case of widely differing crack resistances of the matrix and obstacles forming intact grain bridges. Used with permission from Elsevier. [6].....	20
Figure 3.1 SEM Micrographs of (a) $\text{MgY-Si}_3\text{N}_4$ (b) $\text{MgLa-Si}_3\text{N}_4$ (c) $\text{MgLu-Si}_3\text{N}_4$ (d) $\text{AlY-Si}_3\text{N}_4$	32
Figure 3.2 Silicon nitride fatigue crack growth rate data.....	33
Figure 3.3 Fatigue crack growth rate data normalized contribution of bridging stress intensity to the R-curve for fracture toughness at 150 microns, K_{BR}	36
Figure 3.4 Comparison of crack paths in Si_3N_4 , (a) MgY , (b) MgLa , (c) MgLu and (d) AlY	37
Figure 3.5 Distribution of grain length and aspect ratio of Si_3N_4 , (a) MgY , (b) MgLa , (c) MgLu and (d) AlY [55]	41

LIST OF FIGURES (Continued)

<u>Figure</u>	<u>Page</u>
Figure 4.1 a) Schematic representation of a crack in a material exhibiting crack surface interactions by bridging stresses, b) bridging stress distribution versus crack opening displacement, δ	49
Figure 4.2 Fatigue crack bridging stress distribution for a 99.5% pure Al_2O_3 calculated from weight functions and the fatigue threshold R -curve (solid line). Also plotted are bridging stresses measured using fluorescence spectroscopy (solid circles) with error bars indicating ± 1 standard deviation based on the standard deviation of the linear calibration fit. Figure reproduced with permission from [7]......	53
Figure 4.3 a) COD results at the surface of a crack in a C(T) specimen (circles: measurements, dashed curve: applied displacements, solid curve: result of eq.(3) matched to the measured data), b) bridging stresses for the different test specimens.	63
Figure 4.4 a) Bridging stress distribution data determined for a single specimen along with the associated fit using Eq. 5. Error bars indicate the standard deviation for the calibration constant. b) Fits of the bridging stress data for all specimens showing the difference in peak stress between the light-grey and black specimens.	64
Figure 4.5. The deduced best estimate of the fatigue threshold crack bridging stress distribution for Si_3N_4	66
Figure 4.6 A comparison of the average Raman determined fatigue threshold crack bridging stress distributions for Si_3N_4 . Averages for the black samples (solid line), light grey samples (dashed line), and all samples (dash-dot line) are shown. Also shown is the deduced best estimate from Fig. 4.5 (dash-triple-dot line).	66
Figure 4.7 a) A comparison of the Raman spectroscopy sampling volumes for the black and light grey Si_3N_4 samples. b) A comparison of the Raman sampling volume for the Si_3N_4 samples with the fluorescence sampling volume for the Al_2O_3 samples.	68
Figure 4.8 Influence of a reduced compressive stress normal to a β -crystal. Debonding lengths under the same externally applied load for a) bulk material, b) grains located near a free surface, c) crack surface interaction due to a local frictional bridging event.	71
Figure 4.9 Influence of T-stress on debonding, a) crack kinking at the interface grain/grain-boundary phase, b) effect of $T \neq 0$ on debonding length.....	75

LIST OF FIGURES (Continued)

<u>Figure</u>	<u>Page</u>
Figure 4.10 T-stress for small cracks emanating from narrow notches in a bending bar according to [117].	77
Figure 5.1 Scanning electron micrograph of silicon nitride doped with Mg-Y	88
Figure 5.2 Fatigue Threshold R-curve for semi-elliptical surface cracks in silicon nitride bend beams.	89
Figure 5.3 Fatigue endurance strength based on the half-initial surface flaw size, the dashed line represents a material that is not toughened by bridging, and the solid line represents the worst case cyclical fatigue loading for the Si_3N_4 Mg-Y doped toughened material assuming an a/c ratio of 1.	90
Figure 5.4 Depiction of dimensions of a bend beam with schematic of a semi-elliptical surface crack.....	91
Figure 5.5 Schematic of the process of solving the system of equations 1 and 2 for the prediction curve.....	95
Figure 5.6 Chart depicting maximum and minimum shape and correction factors for the stress intensity in a semi-elliptical surface crack in a bend beam.	96
Figure 5.7 Plot showing the results of the four-point bending experiments to verify the developed fatigue strength endurance prediction tool for semi-elliptical surface cracks in silicon nitride bend beams. The failure below the best-case fatigue threshold line is due to a v-shaped crack.	99
Figure 5.8 Secondary electron micrograph of a post-experiment fracture surface with the initial semi-elliptical surface crack having an a/c ratio of 0.51.	102
Figure 5.9 Optical image of a fracture surface from a specimen that did not fail during the experiment using the Olympus stereomicroscope with the DinoEye capture device, the specimen was statically fractured post-experiment.....	103
Figure 5.10 Optical image taken using the Leica microscope of the fracture surface of the specimen that was loaded below the endurance curve. This specimen failed due to the v-shaped surface crack.	104

LIST OF TABLES

<u>Table</u>	<u>Page</u>
Table 3.1 Mean ΔK_{th} (MPa \sqrt{m}) and Paris Law Exponent, m , values for each material with standard deviation in parenthesis. Homogeneous groups were statistically indistinguishable..	38
Table 3.2 Normalized threshold results summary with standard deviation in parentheses. K_{I0} values were taken from Ref. [1, 2]. Homogeneous groups were statistically indistinguishable ..	38

Fatigue Reliability Predictions in Silicon Nitride Ceramics Based on Fatigue Behavior, Bridging Stresses and Fracture Data

1 Introduction

Recently demands for higher performance materials have made ceramics such as silicon nitride highly sought after. These materials exhibit excellent high temperature properties and resistance to thermal shock. They also are high strength, resistant to fracture, wear resistant, and exhibit excellent dielectric properties.[3-5] Much work has been done to understand the behavior of silicon nitrides and similar materials subjected to cyclical fatigue. The importance this study brings is the ability to incorporate a prediction method for silicon nitride and similar materials subjected to cyclical fatigue.

Silicon nitride is a material toughened by the mechanism of grain bridging. As a crack grows in silicon nitride, elongated grains in the material form bridges that span the wake of the crack. These bridging zones form up to a certain point where the grains can no longer effectively carry load across the crack. Cracks in these materials behave differently based on whether they are shorter than a fully developed bridging zone or long enough to have developed a full bridging zone.[1, 6-10] These shorter cracks will exhibit less resistance to crack propagation than a longer crack, thus breaking classic assumptions like the concept of similitude.[11] These materials exhibit a rising toughness behavior in response to crack extension which can be illustrated with a resistance or R-curve. Measuring R-curves in silicon nitride is a difficult process due to their relatively short bridging zones ($\sim 100\text{ }\mu\text{m}$).[10]

The goal of this project is to better understand the fatigue behavior and develop a design tool for predicting the fatigue failure of ceramics toughened by bridging such as these silicon nitrides doped with rare-earth oxides. Microstructure plays an important role in determining the fatigue behavior in these materials and a correlation will be sought to better understand its impact. In order to accomplish this, the geometry independent bridging stress profile will need to be determined. This will be accomplished two ways. One, by using previously determined fracture data and effectively reducing it to account for lower performance in fatigue due to degradation of grain bridges, and two verifying these results via micro-Raman spectroscopy. Briefly, using micro-Raman spectroscopy allows for micron-scale resolution of stresses being conveyed through bridges across the wake of the crack in a specimen subjected to in situ loading.

The R-curve will then be determined by reducing the magnitude of the static fracture R-curve[1] based on the fatigue threshold stress intensity measured from cyclical fatigue threshold experiments. Computing the fatigue R-curve then allows for the creation of a plot of fatigue endurance strength vs. initial flaw size that can be used for guiding design considerations and safety inspection applications.

2 Background

2.1 *Silicon Nitride*

Silicon nitride, Si_3N_4 , is a highly covalent material with rigid silicon-nitrogen bonds exhibiting a very low coefficient of self-diffusion, this serves as the basis for superior high temperature materials.[12] It has a density of less than 3.44 gm/cm^3 which makes it useful for applications where weight is an issue.[3]

This research focuses on a monolithic, self-reinforced form of silicon nitride, designated as YM- Si_3N_4 . This material is composed of 5 wt. % Y_2O_3 and 2 wt. % MgO as sintering additives. It is particularly of interest because it contains elongated reinforcing grains (Fig. 2.1) with a mean diameter of $0.28 \mu\text{m}$ and a length of about $2 \mu\text{m}$. These grains help to form bridges in the crack wake and increase the toughness of the material by relieving some of the stresses felt at the crack tip.

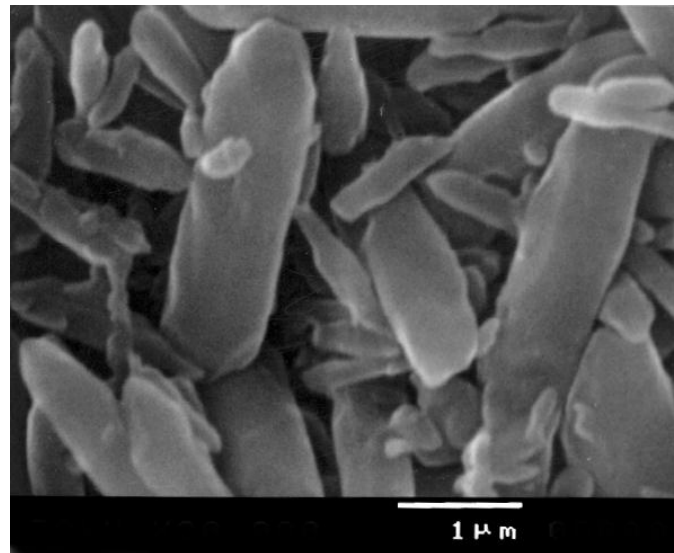


Figure 2.1 SEM micrograph of Si_3N_4 elongated grains. Used with permission from Springer.[13]

Silicon nitrides have two polymorphic crystal structures designated as α - Si_3N_4 and β - Si_3N_4 . (A third phase, gamma, has been identified, but it only occurs under very high nitrogen pressures.) The alpha phase is trigonal while the beta phase is hexagonal (Figure 2.2).

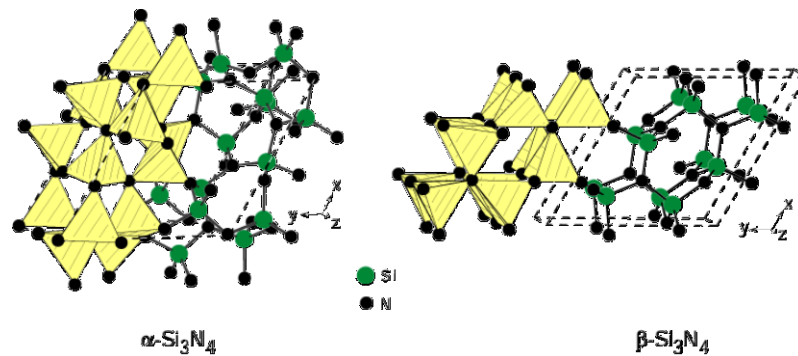


Figure 2.2 Crystal structures of alpha and beta silicon nitride. Used with permission from Wiley.[14]

Interestingly, the α -phase transforms irreversibly into the β -phase at elevated temperatures (greater than 1400°C) through liquid-phase formation during sintering. The most important feature of this phase change is the morphological change in the grains—the α grains are equiaxed while the β grains are elongated.[13] The sintering additives do not form a solid solution with Si_3N_4 so they remain as a bulk grain boundary phase. This grain boundary phase can be either amorphous or partially crystalline. The two-grain junctions, or intergranular films, are always amorphous and contain some sintering additives.[12]

2.1.1 Material Properties

Silicon nitride is a great material for high temperature applications. It exhibits high strength ranging from 500 to 900 MPa in bending depending on the processing method used. It retains these properties up to a temperature around 1000°C where the properties start to decrease. For most silicon nitrides made with sintering additives, the highest functional temperature is about 1400°C, for those without sintering additives, that temperature can approach 1900°C before the silicon and nitride decompose into silica and nitrogen gas.[3]

Silicon nitride also exhibits great thermal shock resistance making it useful for applications where heating is cyclic, like material processing ovens. It also has a relatively low thermal expansion of $3.3 \times 10^{-6} \text{ }^{\circ}\text{C}^{-1}$ and higher thermal conductivity than other ceramics of 30 W/m-K.⁶ It also exhibits heightened creep resistance, some forms of silicon nitride can last over 4800 hours at 1370°C under a 100 MPa stress.[3]

Because of the nature of its microstructure silicon nitride has a higher fracture resistance and a higher fatigue resistance than many ceramic materials. Depending on the processing methods and additives used the fracture toughness can range from 5 to 10 MPa√m.[3, 4] This combined with a hardness of 1600 kg/mm², and a low coefficient of friction make silicon nitride very useful for bearings and other wear applications.[4] It also has a great resistance to oxidation and chemical corrosion making it useful for applications in harsh environments.[5]

Besides having great mechanical properties, silicon nitride also has some uses in the electronics industry. The dielectric for the material ranges from around 5 for amorphous silicon nitride to 9.4 for crystalline silicon nitride. The dielectric constant rates how well the material performs as a dielectric compared to having no dielectric at all. In comparison, amorphous silica has a dielectric of 3.9. Aiding in its dielectric abilities is the high breakdown field constant (when it will cease being a dielectric and start conducting) of 10^7 V/cm. The material also has a high resistivity of 10^{15} ohm-cm.[15]

2.1.2 Material Synthesis

The creation of silicon nitride products, like most other ceramics, begins with powder synthesis. The first of these is direct nitridation. This begins with silicon powder being heated above 1100°C in a nitrogen atmosphere for 5 to 20 hours. A high purity can be achieved by allowing the nitridation to continue for a long time and by controlling the amount of the constituents. This process forms chunks of alpha phase silicon nitride and milling is necessary to break this down into a fine powder form. The powder can be purified using a wet milling method to remove unreacted silicon. This can be a cheap process if the purification step is avoided and if milling time is reduced.[16]

Direct nitridation can also be used to create a final product with little shrinkage. The product is also very porous which leads to mediocre properties of only

100 to 300 MPa in bending. There is an advantage—the absence of sintering additives gives the material the ability to sustain its properties above 1400°C.[16]

Another method of powder synthesis is carbothermal nitridation. This process begins with silica powder and carbon powder in a nitrogen, ammonia, nitrogen/hydrogen or nitrogen/carbon monoxide atmosphere. The powder is heated up to 800°C where oxidation of the carbon occurs, the oxygen is supplied by the silica powder. After this process is complete, the remaining silica powder is brought up to 1400°C where nitridation occurs. This process has the advantage of cheap raw materials but purity may suffer from left-behind carbon and oxygen. Milling is necessary to break down the clumps that form for a finer powder. Purification of the final powder is also necessary.[16]

A method that allows for higher purity and high fineness of the produced powder is diimide decomposition. This begins by reacting silicon tetrachloride and ammonia to form silicon diimide and ammonium chloride.



This reaction can be carried out in liquid form in a number of solvents, such as cyclohexane or toluene or also in gaseous phases. The ammonium chloride is then removed by a calcination step in inert gas at 900°C. After this step, amorphous Si-N-compounds are left in various forms, $\text{Si}(\text{NH})_2$ - $\text{Si}_2\text{N}_3\text{H}$ - Si_3N_4 . These are then heated to

above 1250°C where crystallization takes place. Milling may be used to reduce the size of the particles.

A fourth powder synthesis method is called vapor phase reaction. This is done by reacting vaporous silicon tetrachloride and ammonia together at 1100 to 1350°C. The products are silicon nitride and hydrogen chloride. The process is done in a tube furnace where the raw materials enter and are heated, after the reaction the products exit the tube furnace and silicon nitride is collected. A heat treatment to ensure crystallization is carried out after this process. The final powder is often of high purity and fine.[16]

For microelectronic applications, direct deposition methods can be used. A direct nitridation process is possible where silicon is deposited on a substrate then reacted with nitrogen. Vapor deposition is also possible which follows a similar process to above. Also sputtering methods are possible, either originating from silicon and nitrogen or silicon nitride.[15]

2.1.3 Material Processing

Silicon nitride is a strongly bonded material having a low-diffusivity allowing for it to decompose at 1900°C, solid-state sintering methods are not suitable for a fully dense product. To achieve the densities and properties that make silicon nitride highly sought after, sintering aids that form a liquid phase are needed. These additives also lower the sintering temperature of silicon nitride (as low as 1400°C). The most

popular sintering additives are oxides such as alumina, magnesia, yttria, and rare-earth oxides like lutetium oxide, and lanthanum oxide. MgO and rare-earth oxides are insoluble in silicon nitride so they collect in the intergranular spaces.[12] With alumina, Al-O groups replace some of the Si-N groups in the crystal structure, the final product is known as SiAlON.[3] The rare-earth oxides can affect the aspect ratio of the beta-phase silicon nitride; this depends on the ionic size and binding energy of the rare-earth cation in relation to silicon.[12]

The sintering of silicon nitride can be accomplished by several methods. Pressureless sintering can be useful when a complicated part is desired, perhaps one that has been formed by extrusion, injection molding or tape casting.[17] The silicon nitride green body is then placed in the sintering furnace between temperatures of 1700 and 1900°C. The sintering time is highly dependent on the size of the product and the temperature. This method requires a relatively large amount of sintering additives to achieve good densification and good properties. A nice advantage however, is that the lack of applied pressure gives a uniform density throughout the finished product preventing residual stresses and cracking arising from the sintering process.[18]

Pressure sintering comes in many varieties, the most basic being the hot pressing method. In this method, silicon nitride powder is placed in a graphite die and compressed axially with punches, commonly at pressures near 30 MPa). The whole punch assembly is placed in a furnace. The temperature can be lower than

pressureless sintering, about 1600 to 1800°C, while reaching high densities. The time is reduced also, on average around 30 minutes to an hour depending on part size. A drawback to the hot press method is limited part complexity.[17, 18]

Similar to hot pressing is spark plasma sintering. In this method, a DC current is applied across the material that creates heating directly at the punch surfaces and in some cases in the material itself. This greatly reduces sintering times while achieving good properties.

Another type of pressure sintering is hot isostatic pressing where isostatic pressure is applied with high-pressure gas or liquid. To start, the silicon nitride green body is encased in glass that acts as a gas barrier. This is placed in a furnace which is then placed in a pressure vessel filled with an inert gas, such as argon. An advantage to this process is that complex shapes can be created and sintering temperatures can be lowered. Afterwards, the glass coating must be removed, which can be error-prone. The whole process is rather costly and complicated but good results are obtained.[17]

Gas pressure sintering is similar to HIP in concept, except the sintering is carried out in a nitrogen atmosphere under high pressures at up to 100 atm. The advantage to this method is that the sintering temperatures can be raised well above 1900°C thus shifting the stoichiometry of the system and preventing decomposition. A few downsides are that this process is also more complicated and costly, and also nitrogen gas can become trapped in the bulk creating pressurized bubbles that affect

the fracture toughness. Often a gas pressure sintered part will be heat treated afterwards to help remove these trapped bubbles.[12, 17, 18]

2.1.4 Material Applications

Because of the great properties of silicon nitride, it has found a wide variety of uses in the world, from mechanical and industrial applications to microelectrical applications. The use of silicon nitride in cutting tool inserts was one of its first widely used applications. It is good for this because it has a higher toughness than alumina ($3.5 \text{ MPa}\sqrt{\text{m}}$) and alumina-TiC ($4 \text{ MPa}\sqrt{\text{m}}$). It also retains its strength and hardness to high temperatures. It has a high thermal conductivity that allows heat to be conducted away from the cutting surface and lower thermal expansion that allows more precise cutting. The main material that it is used to cut is cast iron for use in the automotive industry; this it can cut at a rate of 3500 feet per minute.[19]

Silicon nitride also has an important use in bearings for gas turbine engines. These engines have a very high rotational speed and metal bearings can fail by spallation caused by fatigue. Metals also have a higher specific gravity causing very high stresses in the outer race of a metal bearing. Silicon nitride has a lower specific gravity meaning it will experience lower stresses throughout. It also has a higher hardness and strength contributing to a life of upwards of 12 million cycles at 700 MPa—8 times longer than that of steel bearings. A bonus is that silicon nitride is very corrosion resistant so it is useful in harsh environments.[20]

There are also uses for silicon nitride in reciprocating diesel engines. One is for use in glow plugs. The lower heat capacity of silicon nitride means that the glow plugs will heat up quicker, giving improved start-up, improved combustion characteristics, better control of timing, and better compression ratios. The total power output can be increased by 10% and particulate emissions can be reduced by up to two-thirds. Another use is for lining swirl chambers; doing so also reduces emissions, makes start-up faster and helps lower noise.[20]

Silicon nitride can also be used to create turbocharger rotors. The lower specific gravity means a lighter rotor with a smaller stress distribution and a 16% faster response time. This lower inertia means less engine lag contributing to better performance. The material is used for this application because of the high temperature strength and resistance to creep; also the thermal expansion is low enabling design to higher tolerances.[20]

The material also has many applications in manufacturing. It is useful for fixtures that transfer parts during heating and welding and crucibles for molten metals. It is also useful for spouts and nozzles carrying a variety of materials, most notably its wear resistance makes it great for sandblasting nozzles. It has found use in rollers for creating wire from high performance alloys.[21, 22] High thermal shock and good electrical insulating properties make it suitable for arc welding nozzles. It can also make a great thermocouple sheath.[5]

Silicon nitride also has many applications for microelectronics products. Most notably, it is great as a capacitor dielectric. Its high dielectric constant and high breakdown voltage help to make smaller capacitors with high capacitances and high voltage capabilities. It can also effectively be used for isolation; this application electrically separates components. Silicon nitride is suited for this because it is non-polarized preventing the buildup of electrical fields between components. For this property it can substitute silicon dioxide insulating layers in integrated circuits. It also makes an excellent diffusion mask. This prevents the diffusion of dopants from an n-type to p-type (or vice-versa) preserving the functionality and extending the lifetime of components.[15]

Silicon nitride can also play an important part in the creation of composites. It has been used as the matrix or filler phase in composites. As the filler phase, beta-phase elongated grains behave as whiskers. Adding silicon carbide whiskers to silicon nitride can increase its fracture toughness to values above $10 \text{ MPa}\sqrt{\text{m}}$.

2.1.5 Material Summary

Silicon nitride is a very interesting and useful material. Its unique chemical characteristics give it great high temperature properties. Its microstructure also gives it great fracture and fatigue resistance. It has found many uses in manufacturing, mechanical and micro-electronics applications. The large amount of research available on the material is daunting and there seems to be little limit to discovering new applications and engineering a better silicon nitride.

2.2 Fracture Mechanics

2.2.1 Fracture Mechanics Basics

Fracture mechanics studies the effects of cracks in materials. A crack in a material basically creates a flaw with an atomically sharp radius. The effect of this flaw creates a stress concentration that can be quantified with the stress intensity factor, K . [23] For an applied stress, σ_{app} , the applied stress intensity factor, K_{app} (in $MPa\sqrt{m}$), can be expressed as,

$$K_{app} = Y\sigma_{app}\sqrt{\pi a}, \quad (1)$$

where Y is the geometric factor specific to the specimen geometry and a is the length of the crack. The effect of varying crack length with a constant applied stress on K_{app} can be visualized in Fig. 2.3.

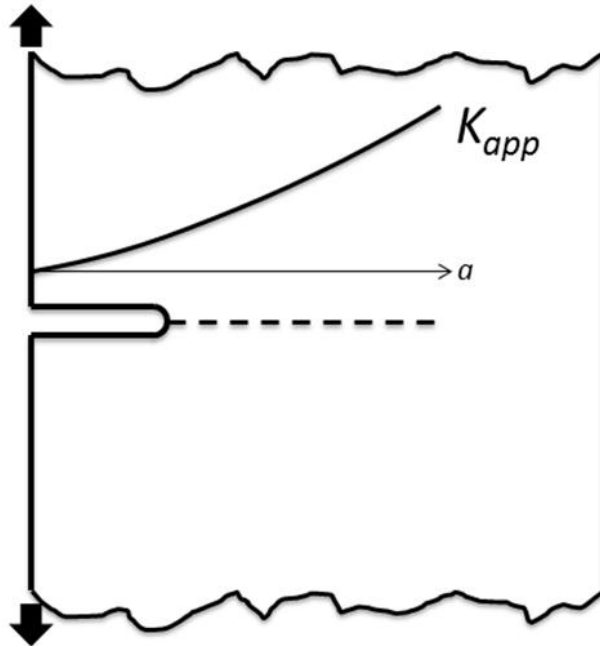


Figure 2.3: Effect of crack length on the applied stress intensity factor, K_{app} .

The resistance of a material to brittle crack growth is a material property known as the fracture toughness or critical stress intensity. This value is denoted as K_{IC} , where the subscript, I , denotes mode I or opening displacement loading.

2.2.2 Toughening Mechanisms

Materials can be toughened by many mechanisms but of interest to this study are intergranular fracture and grain bridging in brittle ceramics. Intergranular fracture is encouraged by an intergranular film that is weaker than the grains in the material, otherwise transgranular fracture would occur. The crack deflection and kinking around grains in the material requires more energy and thus increases resistance to crack growth. The intergranular fracture also leads to the creation of grain bridges. These bridges span the crack wake and are able to carry load thus reducing the stress intensity felt at the crack tip. [23] A simple schematic illustrating this mechanism can be seen in Fig. 2.4.

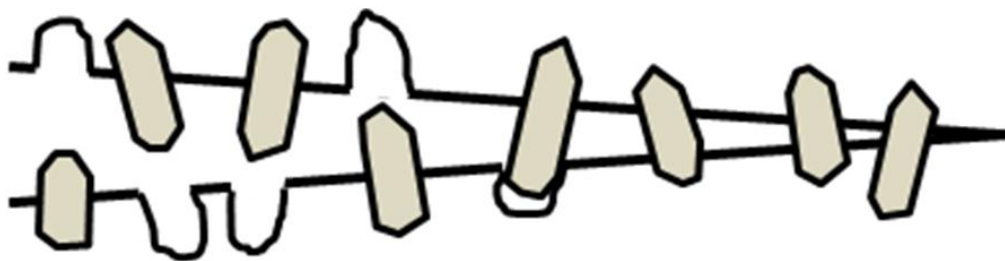


Figure 2.4: Schematic of grain bridging.

It can also be inferred from the schematic that as the crack grows, bridges further behind the crack tip are no longer functional due to being fully pulled out of their original sockets, in the case of frictional grain bridges, or broken, in the case of ligament grain bridges. The effective area of bridging is referred to as the bridging zone, it moves along with the crack tip as it propagates.[23, 24]

2.2.3 Bridging Stress Distributions

The stresses carried by the grain bridges can be represented by a bridging stress distribution, $\sigma_{br}(x)$, where x is the distance behind the crack tip. The distribution can be seen in Fig. 2.5.

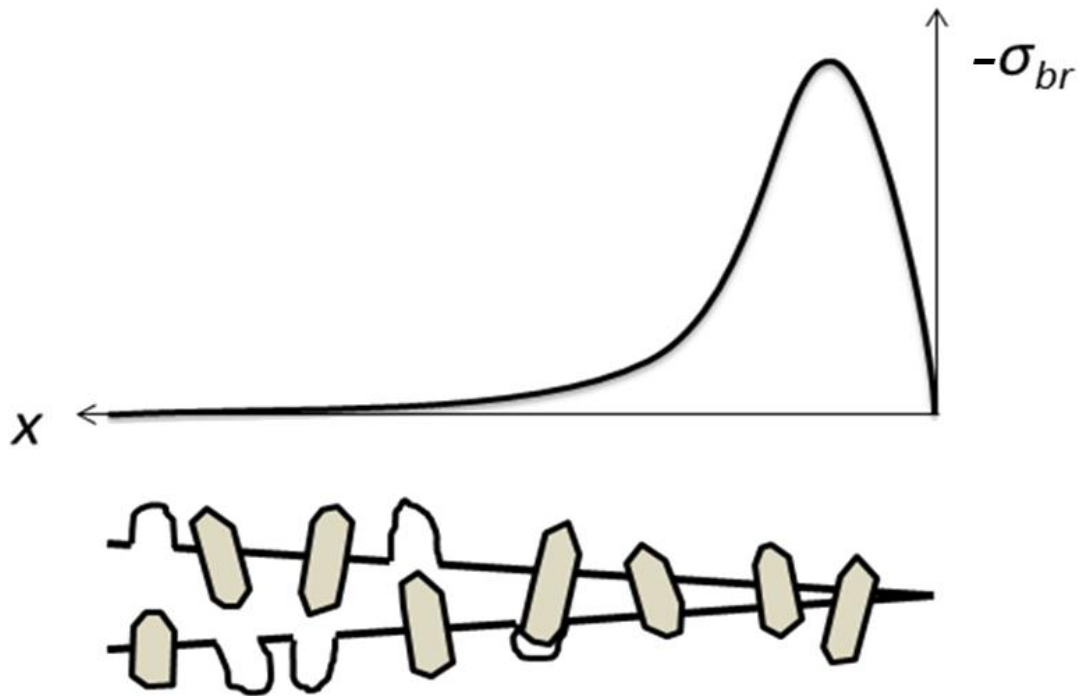


Figure 2.5: Bridging stress distribution.

While bridges themselves are a discrete phenomenon, modeling of the bridges is treated as a continuum. The crack tip is treated as if no bridges are present and thus no bridging stresses are expressed there. It is assumed that through the thickness of a crack this is an appropriate assumption.[25] In analyzing the bridging stress distribution it can be noted that the full effect of crack bridging is not reached if the crack is shorter than the effective bridging zone length. This is referred to as a functionally short crack. When the crack has grown long enough to where the bridging zone is fully developed it is referred to as a functionally long crack. [9]

2.2.4 Resistance Curves

As a crack toughened by grain bridging grows it exhibits increasing resistance to crack growth. To visualize this effect we can use the bridging stress distribution for a material and express it in terms of stress intensity. The resulting distribution dependent on crack length is the stress intensity due to bridging, K_{br} . [26] K_{br} can be determined by,

$$K_{br} = \int_0^a h(x,a) \sigma_{br} dx, \quad (2)$$

where $h(x,a)$ is a geometric factor depending on sample type, total crack length, a , and distance behind the crack tip, x . [27] The process is illustrated in Fig. 2.6.

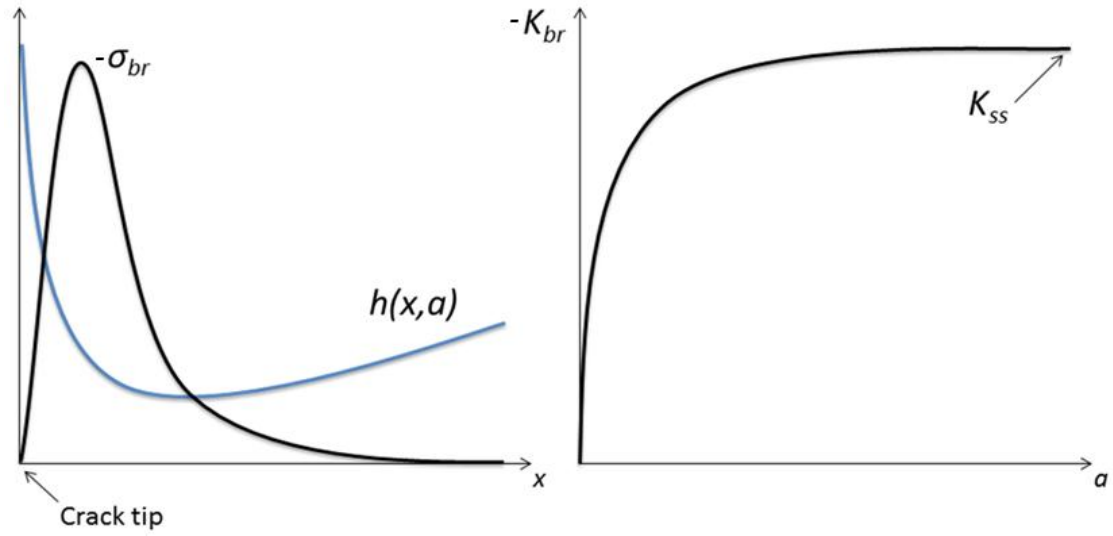


Figure 2.6: Process for determining K_{br} from the bridging stress distribution.

For a crack of minimal length the contribution of bridging stresses is zero. As a crack develops a full bridging zone the stress intensity due to bridging reaches a steady state value, K_{ss} . The overall effect that this has on the stress intensity felt at the crack tip can be seen in Fig. 2.7 and is expressed as the following,

$$K_{tip} = K_{app} + K_{br}. \quad (3)$$

This increasing resistance behavior for a material can be illustrated by what is known as an R-curve, or resistance curve. The R-curve (Fig. 2.6) is created by adding the contribution of bridging stress intensity to the intrinsic fracture toughness of the material, K_{I0} ,

$$K_R = K_{I0} - K_{br}. \quad (4)$$

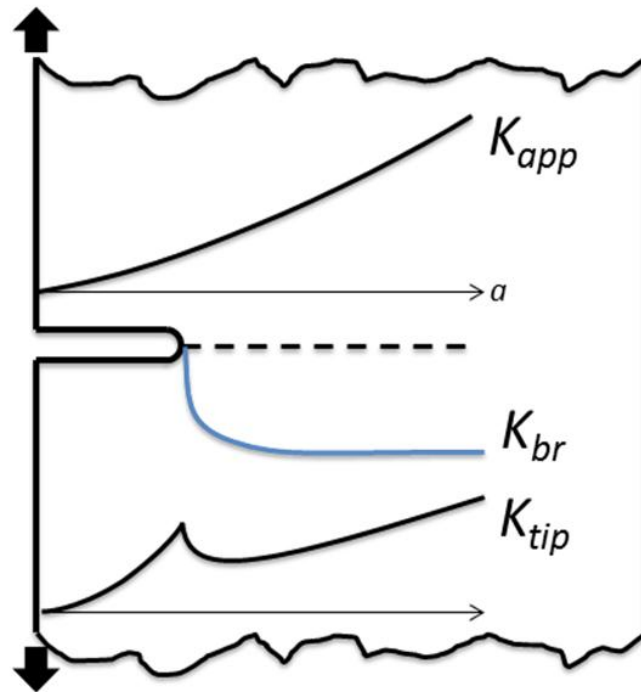


Figure 2.7: Effect of K_{br} on K_{tip} .

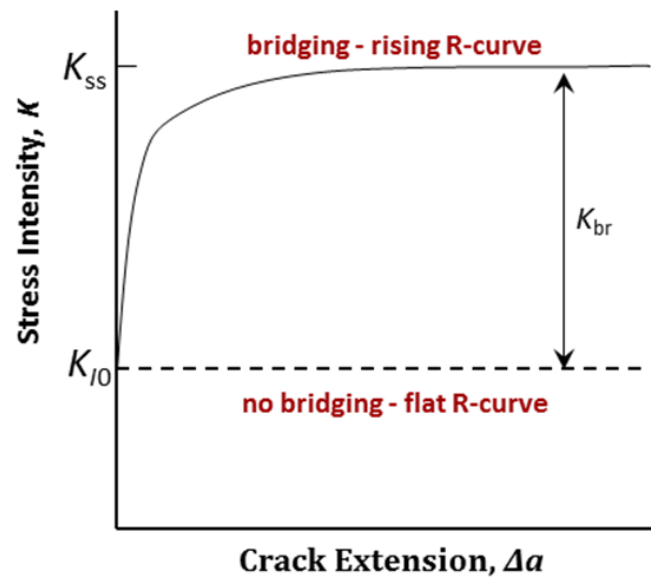


Figure 2.8: Schematic of an R-Curve demonstrating increased toughness over a non-toughened material.

2.2.5 Crack Growth Behavior in Silicon Nitride

Crack growth in silicon nitride can be divided into four different regions. These regions are also exhibited in the change in shape the R-curve for the material. [6] Stage I occurs at the beginning of crack growth and is represented by the sharply rising portion of the R-curve in the first $\sim 10 \mu\text{m}$. The toughness reached in this stage is mainly due to the amount of elastic bridges present. The intergranular film allows for the crack to extend through the material discouraging intergranular fracture for a fraction of the grains depending on angle to the crack plane and strength of the film.[6] This subsequently encourages the formation of elastic bridges that are fully connected to the bulk of the material but span the crack as it grows. These fully intact grains also act as pinning locations impeding the elongation of the crack (Fig. 2.9). [6]

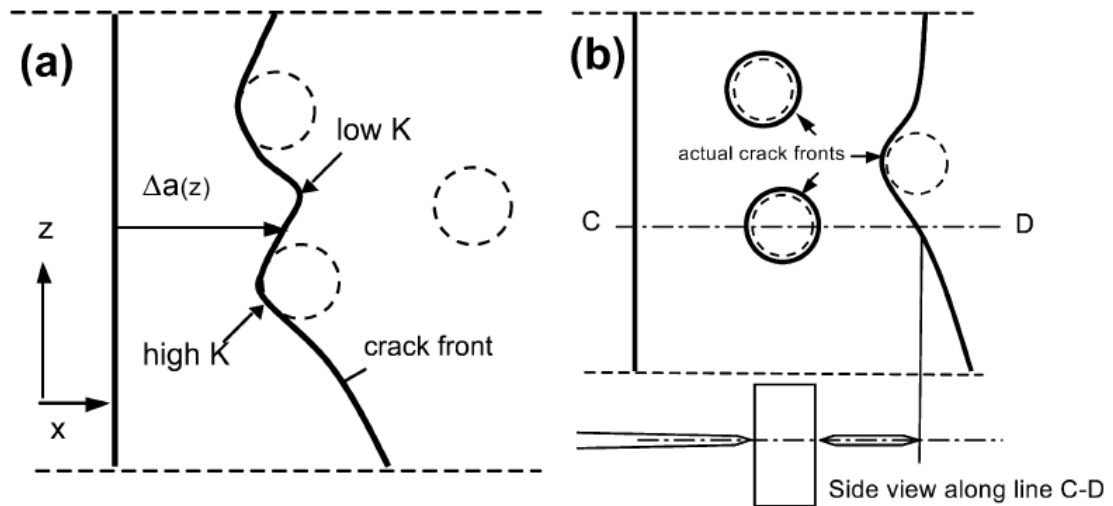


Figure 2.9: Crack extension appearing in the “matrix” material: (a) crack extension with pinning at individual $\beta\text{-Si}_3\text{N}_4$ grains, (b) crack-front dissolution in the case of widely differing crack resistances of the matrix and obstacles forming intact grain bridges. Used with permission from Elsevier. [6]

Stage II of crack development is represented by the region where the slope of the R-curve begins to decrease rapidly. In this region, previously formed elastic bridges start to debond from the surrounding bulk material and pull out of their sockets. In Stage III, represented by the slowly increasing plateau-like region on the R-curve, the previously debonded grain bridges either experience frictional contact between their sides and the bulk material or a mechanical interaction that still allows for force to be carried by them across the crack. [6]

Finally stage IV occurs when all bridging effects are saturated. Old bridges (those far beyond the crack tip) are completely destroyed and new ones form as the crack propagates. Here the R-curve has reached its plateau value and no additional toughening can be achieved. [6]

2.3 *Fatigue*

Cyclic fatigue occurs when a material is subject to repeated loading and unloading. [23] The stress intensity range for this type of loading is denoted as ΔK . ΔK is the difference between the maximum and minimum applied stress intensities, $K_{max} - K_{min}$. The fatigue loading ratio, R is equal to K_{min}/K_{max} . The fatigue threshold, ΔK_{th} , is the value where a crack ceases growth under fatigue loading at a certain loading ratio. This is often taken as the stress intensity range at a crack growth rate of less than $10^{-10} m/cycle$. [28]

2.3.1 *Fatigue Threshold R-Curves*

The idea of resistance curves for static loading can be extended to cyclic loading. The effect of fatigue on the material acts to degrade the grain bridges reducing their effectiveness thus reducing the overall toughness in fatigue. [24, 29, 30]

2.3.2 *Behavior of Fatigue Crack Growth in Silicon Nitride*

Previous research into the mechanisms of cyclic fatigue crack growth has focused their analyses on several possibilities. It was previously theorized by Okazaki et al. (1991) that wedging observed in the crack wake was responsible for the formation of microcracks at the crack tip upon closure. Upon the loading cycle the microcracks would join to contribute to the average crack advance. [31] Later work by Glibert et al. (1995) showed that this is not the case for silicon nitrides—elastic bridges near the crack tip are still under elastic load during the unloading phase preventing possible wedging effects. [30]

It was observed that the main cause behind sub-critical cyclic fatigue crack growth in silicon nitride is dependent on the loading ratio, R , and the maximum stress intensity, K_{max} . Bridges under cyclic loading are continuously being degraded by sliding contact between the matrix/grain interface. This reduces their effectiveness thus increasing stress intensity felt at the crack tip (Eq. 3) allowing for subcritical crack advance. Higher loading ratios decrease the sliding distance of the bridges. This has the effect of reducing the wear on frictional bridges which then allows for a higher maximum stress intensity.[30]

Experiments by Jacobs and Chen (1994) aimed to characterize the effects of differing environments on fatigue crack growth in silicon nitride ceramics. This study found a strong sensitivity to moisture in the environment to increased crack growth rates. This mechanism is correlated to similar behavior in silicon dioxide glasses where water is absorbed at the crack tip encouraging intergranular grain growth. However, in dry environments crack growth still occurs but at a much lower rate.

2.4 *Micro-Raman Spectroscopy*

Micro-Raman spectroscopy is the application of Raman spectroscopy on a micrometer-scale. The basic theory behind Raman spectroscopy is that when molecules are excited with incident monochromatic laser light that light is inelastically scattered by interacting with the electron cloud and the bonds of the material.[32] An example of a simple case is a molecule being modeled as a two body system attached with a spring. In the quantum world, this system is vibrating between two energy states, the ground and the first excited state. Raman scattering occurs when a photon of light strikes the bonding electron when the molecule is transitioning from ground level to the first energy state or the reverse. The photon is briefly absorbed resulting in the bonding electron being transferred to a higher “virtual” energy level and then emitted when the molecule settles into the new vibrational state. The emitted photons correspond to bond energy levels specific to different compounds, thus each material has its own Raman spectrum. [32]

Micro-Raman spectroscopy can be used to measure strain and thus stresses at a micron-size scale. Specimens can be subjected to loading and a laser is used to cause the Raman scattering. Silicon nitride exhibits a high-frequency Raman-active shift-peak at 862 cm^{-1} . [33] This peak exhibits linear stress dependence so that the amount of shift in the peak can directly be used to determine the amount of stress present in the material being sampled. [26, 34]

Fatigue crack growth of Si_3N_4 : Roles of grain aspect ratio and intergranular film composition

R. B. Greene, S. Fünfshilling, T. Fett, M. J. Hoffmann, J. J. Kruzic

3 Fatigue crack growth of Si_3N_4 : Roles of grain aspect ratio and intergranular film composition

3.1 *Abstract*

The role of microstructure in affecting the fatigue crack growth resistance for grain bridging silicon nitride ceramics doped with rare earth ($\text{RE} = \text{Y}, \text{La}, \text{Lu}$) oxide sintering additives is investigated. Three silicon nitride ceramics were prepared with $\text{MgO-RE}_2\text{O}_3$ and results were compared with a commercial $\text{Al}_2\text{O}_3\text{-Y}_2\text{O}_3$ doped material. Decreasing stress intensity range (ΔK) fatigue tests were conducted using compact tension specimens to measure steady state fatigue crack growth rates. Specimens doped with $\text{MgO-RE}_2\text{O}_3$ additives showed a significantly higher resistance to crack growth than those with $\text{Al}_2\text{O}_3\text{-Y}_2\text{O}_3$ additives and this difference was attributed to the much higher grain aspect ratio for the $\text{MgO-RE}_2\text{O}_3$ doped ceramics. When the crack growth data was normalized with respect to the total contribution of toughening by bridging determined from the monotonically loaded R -curves the differences in fatigue resistance were greatly reduced with the data overlapping considerably. Finally, all of the $\text{MgO-RE}_2\text{O}_3$ silicon nitrides displayed similar steady state fatigue crack growth behavior suggesting they are relatively insensitive to the intergranular film.

3.2 *Introduction*

Monolithic ceramics can now be developed to exhibit superior strength and fracture toughness properties by creating microstructures that promote significant extrinsic toughening by mechanisms such as crack bridging or transformation

toughening.[35, 36] One successful approach is to sinter ceramics, such as Si_3N_4 , SiC , or Al_2O_3 , with additives that give: i) sufficiently weak grain boundaries and ii) bimodal grain distributions and/or high aspect ratio self-reinforcing grains.[37-44] Cracks propagate through these microstructures intergranularly, which leads to extrinsic toughening via crack deflection and crack bridging. However, one tradeoff is that such bridging ceramics are prone to premature failure due to cyclic fatigue loading.[45-49]

Overall, the improved properties of toughened ceramics result in a wider range of potential commercial applications. For example, silicon nitride ceramics doped with rare-earth oxides exhibit excellent hardness, toughness, and strength at elevated temperatures making them attractive materials for replacing cemented carbides in a variety of manufacturing applications such as cutting and rolling tools. Indeed, it has been shown that for steel wire rolling under moderate loading silicon nitride rolls can give >10 times longer life and improved wire surface quality compared to cemented carbides.[21] However, it has also been shown that silicon nitride rolls can suffer fatigue failure at higher loadings, for example when rolling Ni-base superalloy wires with high deformation resistance.[21, 22] Similarly, silicon nitride is an attractive ball bearing material for many applications and avoiding fatigue failures and making life predictions of the Si_3N_4 balls are engineering concerns.[50]

Early studies on the mechanism of fatigue crack growth in Si_3N_4 ceramics proposed that a wedging effect observed in the crack wake was responsible for the formation and linking of microcracks at the crack tip contributing to the average crack

advance;[51, 52] however, later work by Choi suggested crack face contact actually causes a crack closure effect that retards the crack growth.[53] It is now generally accepted that fatigue cracks propagate due to frictional bridges being continuously degraded by sliding contact between the matrix/grain interface.[46] This increases the stress intensity, K , felt at the crack tip allowing for subcritical crack advance. Generally, the crack growth rate is found to be more sensitive to the maximum stress intensity, K_{\max} , than the stress intensity range, $\Delta K = K_{\max} - K_{\min}$. [46] Because of the low dependence on K_{\min} , crack closure only plays a minor role and it cannot explain the effect of changing load ratios, $R = P_{\min}/P_{\max}$, on fatigue crack growth rates like it can in metals.[46] Rather, higher loading ratios are thought to decrease the sliding distance and reduce the wear on frictional bridges thus giving slower crack growth at a given K_{\max} . [46] Silicon nitrides are also sensitive to moisture in the environment which cause increased crack growth rates; however, in dry environments crack growth still occurs but at a much lower rates.[51, 54]

Based on the well-known mechanisms of fatigue crack growth it can be assumed that the microstructural features affecting crack bridging will also affect the fatigue crack growth properties. Although the basic microstructural features which promote crack deflection, bridging, and high toughness have been extensively studied in Si_3N_4 , [35, 44, 55, 56] there is relatively little available information about how those microstructural features relate to the fatigue behavior. For Si_3N_4 ceramics to be used more frequently as moving components in dynamic mechanical systems the relations between fatigue behavior and microstructure must be better understood. Accordingly,

the purpose of this paper is to better understand the roles of different grain aspect ratios and grain boundary phases in affecting the fatigue crack growth behavior of several rare-earth (RE) doped silicon nitrides.

3.3 Procedures

3.3.1 Materials

Four different silicon nitride, Si_3N_4 , ceramics were used in this study containing different rare-earth oxide (Y_2O_3 , La_2O_3 , and Lu_2O_3) and main group metal oxide (MgO , Al_2O_3) combinations as dopants.

- A hot- isostatically- pressed silicon nitride with 5 wt% Y_2O_3 and 2 wt% MgO as sintering aids (denoted as MgY),
- A hot- isostatically- pressed silicon nitride with 8.5 wt% Lu_2O_3 and 1.93 wt% MgO as sintering aids (denoted as MgLu),
- A hot- isostatically- pressed silicon nitride with 7.1 wt% La_2O_3 and 1.96 wt% MgO as sintering aids (denoted as MgLa),
- A commercial silicon nitride with Y_2O_3 and Al_2O_3 content SL200BG (CeramTec, Plochingen, Germany) (denoted as AlY)

The first three materials (Figs. 3.1a-c) were consolidated in a two-step sintering process to achieve similar microstructures despite their different rare earth (RE) sintering additives. Full details on the preparation of the experimental materials (MgY, MgLu, and MgLa) may be found in Satet and Hoffmann (2005).[57] Briefly,

powders were prepared by attrition milling in isopropanol and the slurries were subsequently dried and the powders sieved. Green bodies were uniaxially pressed and then subsequently cold-isostatically pressed with 400 MPa. The three different compositions were sintered at different temperatures and dwell times in order to tailor the microstructures to similar grain sizes and morphologies.[57] The samples were sintered in a hot-isostatic-press (HIP) with a two-step sinter-HIP process, where closed porosity was obtained at low N_2 pressures during the first sintering step and full density was achieved during the subsequent HIP step at a maximum nitrogen pressure of 10 - 20 MPa. Full density (water immersion method) is defined here for relative densities greater than 99% of theoretical density, which was calculated by the rule of mixture based on the starting compounds. The fourth material (Fig. 3.1d) was a commercial silicon nitride containing 3 wt.% Y_2O_3 and 3 wt.% Al_2O_3 (SL200BG, CeramTec, Plochingen, Germany).

3.3.2 *Fatigue crack growth testing*

Standard compact-tension, C(T), specimens were prepared from each ceramic with width, $W \approx 19$ mm, and thickness, $B \approx 3.5$ mm.[58] After machining was completed, the surfaces were ground and polished to ~ 1 μm final finish so fatigue cracks could be easily observed. Additionally, the machined notches were extended by razor micro-notching to achieve root radii, ρ , of less than 10 μm in order to aid crack initiation. This was accomplished using a custom machine that slides a razor blade coated with a 1 μm diamond paste over the machined notch using $\sim 1 - 3$ N of applied force.

The samples were then pre-cracked by applying cyclic loads with a computer controlled servo-hydraulic test machine using a 25 Hz sine wave and ratio of minimum to maximum load of, $R = P_{\min}/P_{\max} = 0.1$. The stress intensity range, $\Delta K = K_{\max} - K_{\min}$, was held constant for a time interval of >3600 s, where K_{\max} and K_{\min} are the maximum and minimum stress intensity experienced on each cycle, respectively. After each time interval, if no crack growth was detected the ΔK level was step increased $\sim 0.1 \text{ MPa}\sqrt{\text{m}}$ and the process repeated until a crack grew from the notch. Crack growth was detected by an increase in the sample compliance, measured as the slope of the back-face strain vs. load curve. Back face strain was measured using a strain gage mounted centered on the back of the C(T) specimen. The sample was periodically removed for measurement of the pre-crack using an optical microscope. Pre-cracks were grown until the crack was 1) significantly long enough for bridging zones to develop (i.e., greater than $100 \text{ }\mu\text{m}$)[59, 60] and 2) the crack front was straight (e.g. length on each side within $<10\%$ of each other).

Decreasing ΔK fatigue tests were then conducted using the above fatigue test conditions in general accordance with ASTM standard E647.[58] An initial stress intensity range, ΔK_i , was chosen so that the per-cycle crack growth rate was near 10^{-8} m/cycle. As the crack length, a , increased, the rate of force shedding was controlled to maintain the desired applied stress intensity range, ΔK , by using a normalized ΔK -gradient of $\gamma = -0.08 \text{ mm}^{-1}$ such that

$$\Delta K = \Delta K_i \exp[\gamma (a - a_0)], \quad (1)$$

where a_0 is the pre-crack length. Crack lengths were constantly monitored using standard C(T) compliance calibrations for back face strain.[61] Data points were collected at a nominal crack growth interval of 10 μm . After the experiments crack profiles and fracture surfaces were examined using scanning electron microscopy (SEM).

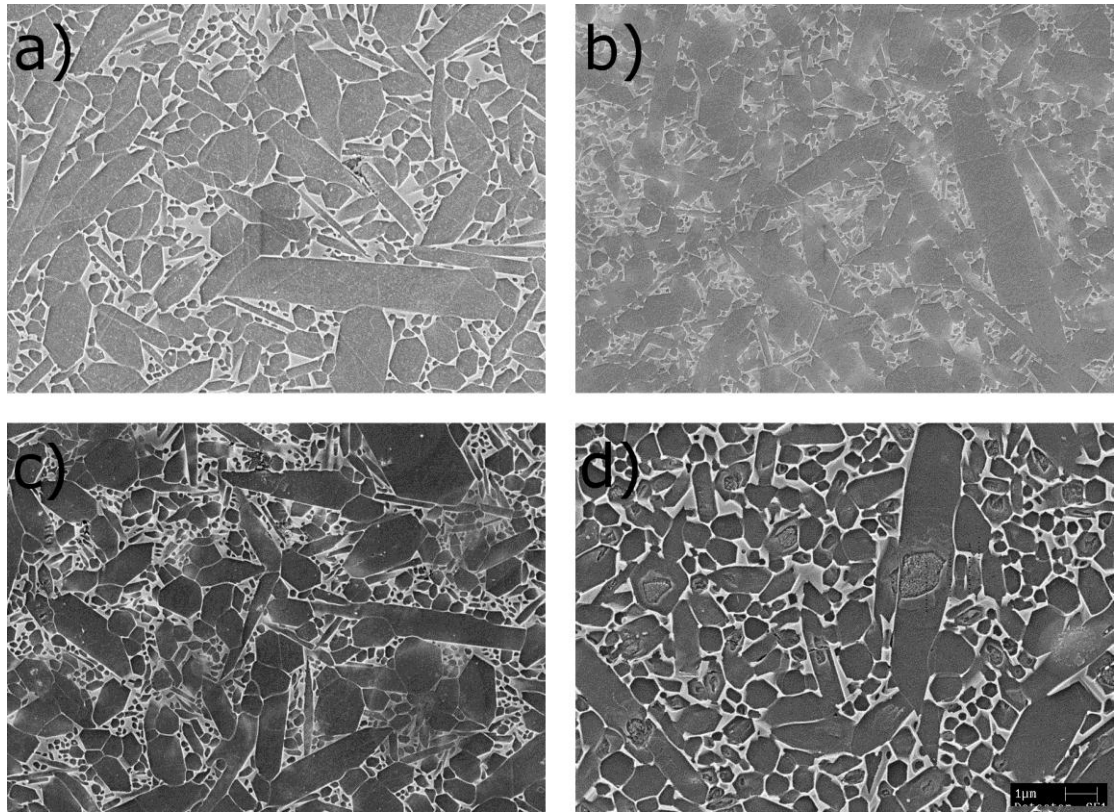


Figure 3.1 SEM Micrographs of (a) MgY-Si₃N₄ (b) MgLa-Si₃N₄ (c) MgLu-Si₃N₄ (d) AlY-Si₃N₄

3.4 Results

Crack growth rates, da/dN , were determined by calculating a linear fit over ~ 100 μm increments of the crack length, a , versus cycle, N , data. The corresponding ΔK values were taken as averages calculated over that same range of data. Log-log plots of the crack growth rate, da/dN , versus ΔK data for all samples are presented in Fig. 3.2. Significant overlap in the data is observed for the three MgRE materials while the AlY silicon nitride exhibits significantly lower fatigue crack growth resistance.

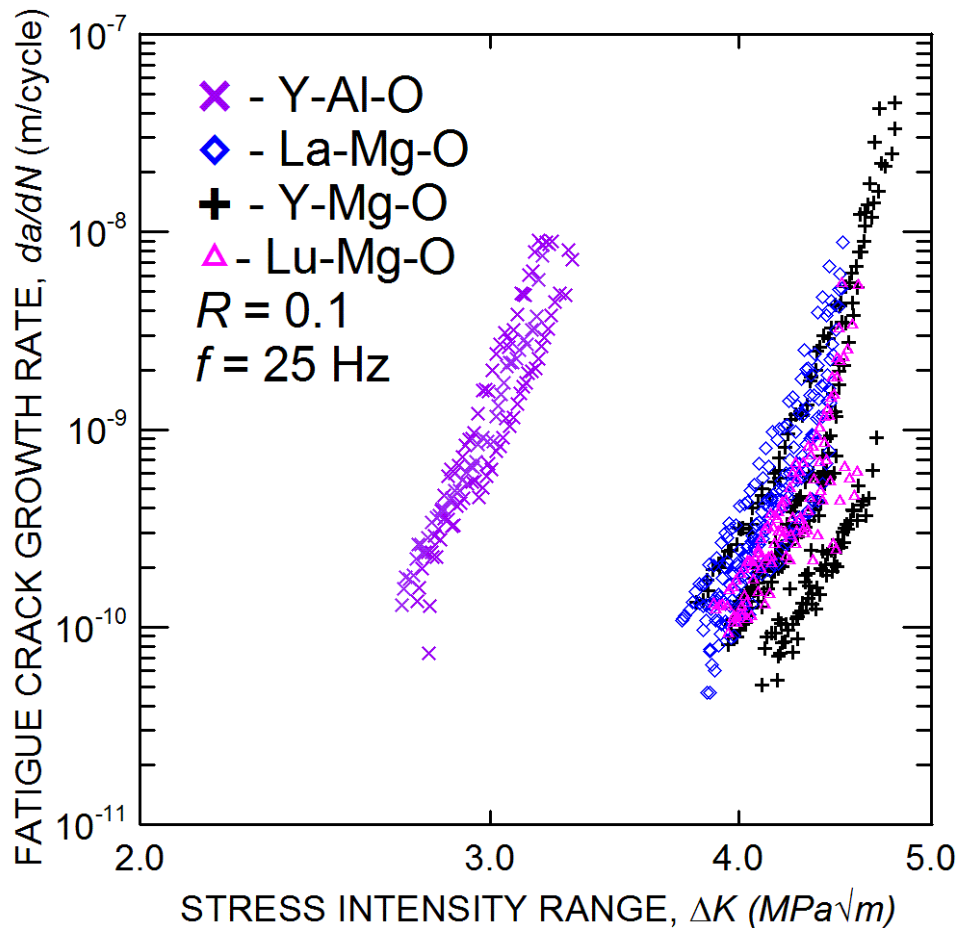


Figure 3.2 Silicon nitride fatigue crack growth rate data

The material constants, C and m , from the Paris Law equation,

$$da/dN = C\Delta K^m, \quad (2)$$

were determined for each sample by fitting the da/dN - ΔK data over the growth regime from 10^{-10} to 10^{-9} *m/cycle* (Table 1). Furthermore, the fatigue threshold, ΔK_{th} , was determined as the point where the growth rate drops below 10^{-10} *m/cycle*. A one way analysis of variances (ANOVA) was performed using Tukey's honestly significant difference (HSD) procedure to compare the fatigue threshold means for the different materials with $p < 0.05$ defined as statistically significant. There was no statistically significant difference among the MgRE materials, while the AlY material had a significantly lower fatigue threshold. This is also represented in Table 1 where there are two homogeneous groups that are statistically different from each other. Within each group there is no significant difference between the means ($p > 0.05$). Based on these results it is seen that AlY shows the least resistance to crack growth while the three MgRE microstructures show a higher resistance that is indistinguishable between the various RE dopants.

Since fatigue crack growth arises from the degradation of crack bridging, the data was normalized by the toughening contribution due to bridging, K_{br} , for cracks with no degradation. To determine the K_{br} values the plateau fracture toughness values from the R -curves, K_R , and intrinsic toughness values, K_{I0} , were taken from data in the literature (Table 2).[1, 2, 55] Since the literature R -curves were determined for 3-point bend beams and R -curves are sample geometry dependent, the K_R values were determined by calculating the R -curves for the C(T) specimen geometry using the

reported bridging stress distributions, σ_{br} , for the respective materials.[55] The bridging stress distribution is considered a geometry independent material property when it adequately represents the through thickness bridging behavior of the crack without a significant T-stress contribution.[25] The bridging stress distribution can be related to K_R :[27]

$$K_{br} = \int_0^{\Delta a} h(r, a) \sigma_{br}(r) dr . \quad (3)$$

using the specific geometrical weight function, h , for C(T) specimens.[27] The upper limit of the integral was taken to be $\Delta a = 150 \mu\text{m}$ of crack extension, which is essentially on the plateau of the R -curves. K_{br} and K_R are related according to:

$$K_{br} = K_{I0} - K_R, K_{br} < 0 . \quad (4)$$

Fig. 3.3 shows the fatigue crack-growth data normalized to K_{br} . Additionally, Table 2 shows the deduced values of K_{br} for C(T) specimens and the normalized ΔK_{th} values.

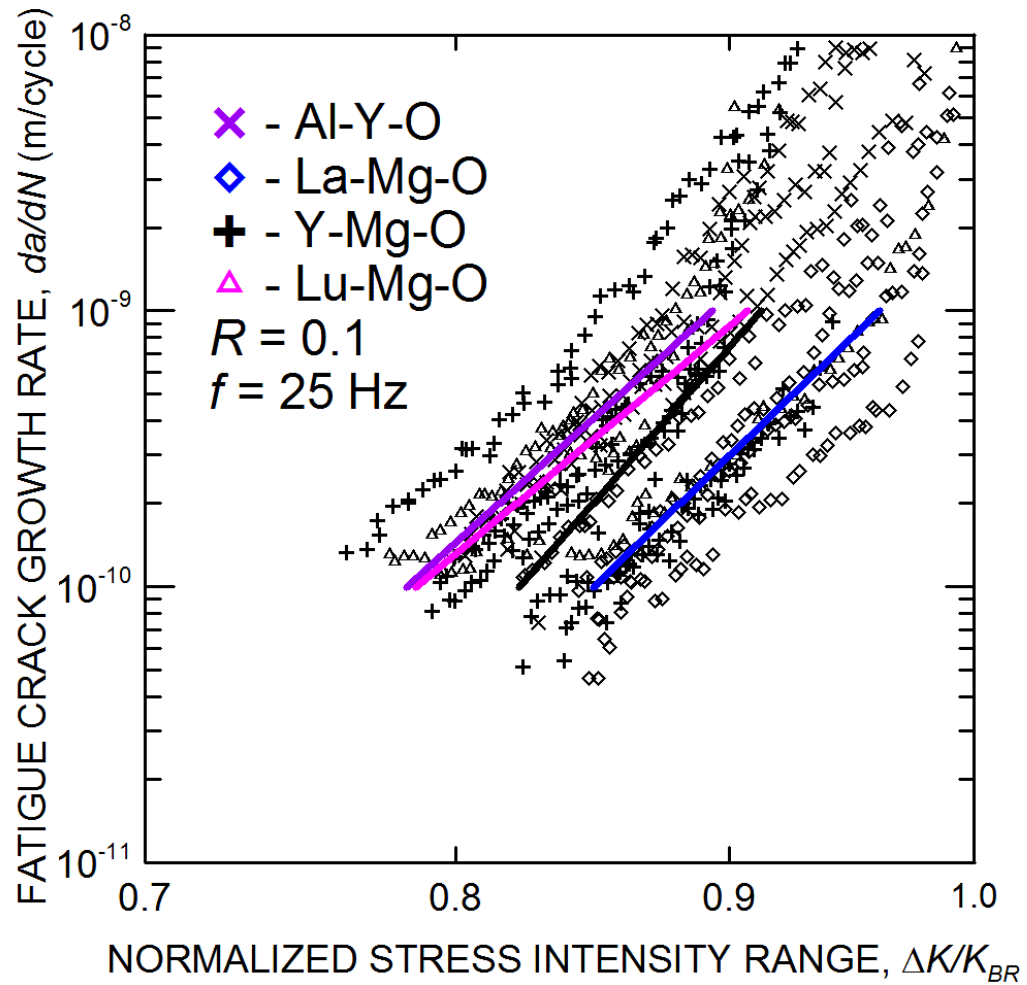


Figure 3.3 Fatigue crack growth rate data normalized contribution of bridging stress intensity to the R-curve for fracture toughness at 150 microns, K_{BR} .

Again using a one-way ANOVA and Tukey's HSD procedure the normalized means for the different materials were compared. Table 2 shows the statistical test results. There are two overlapping homogeneous groups that are statistically different from each other ($p < 0.05$); each material is marked with an X in the group column to denote which to groups it belongs. Finally, the crack profile morphologies can be seen

for each sample in Fig. 4. In Fig. 4 each crack profile shown was taken a similar distance of $\sim 150\text{ }\mu\text{m}$ behind the crack tip of a crack grown to the fatigue threshold.

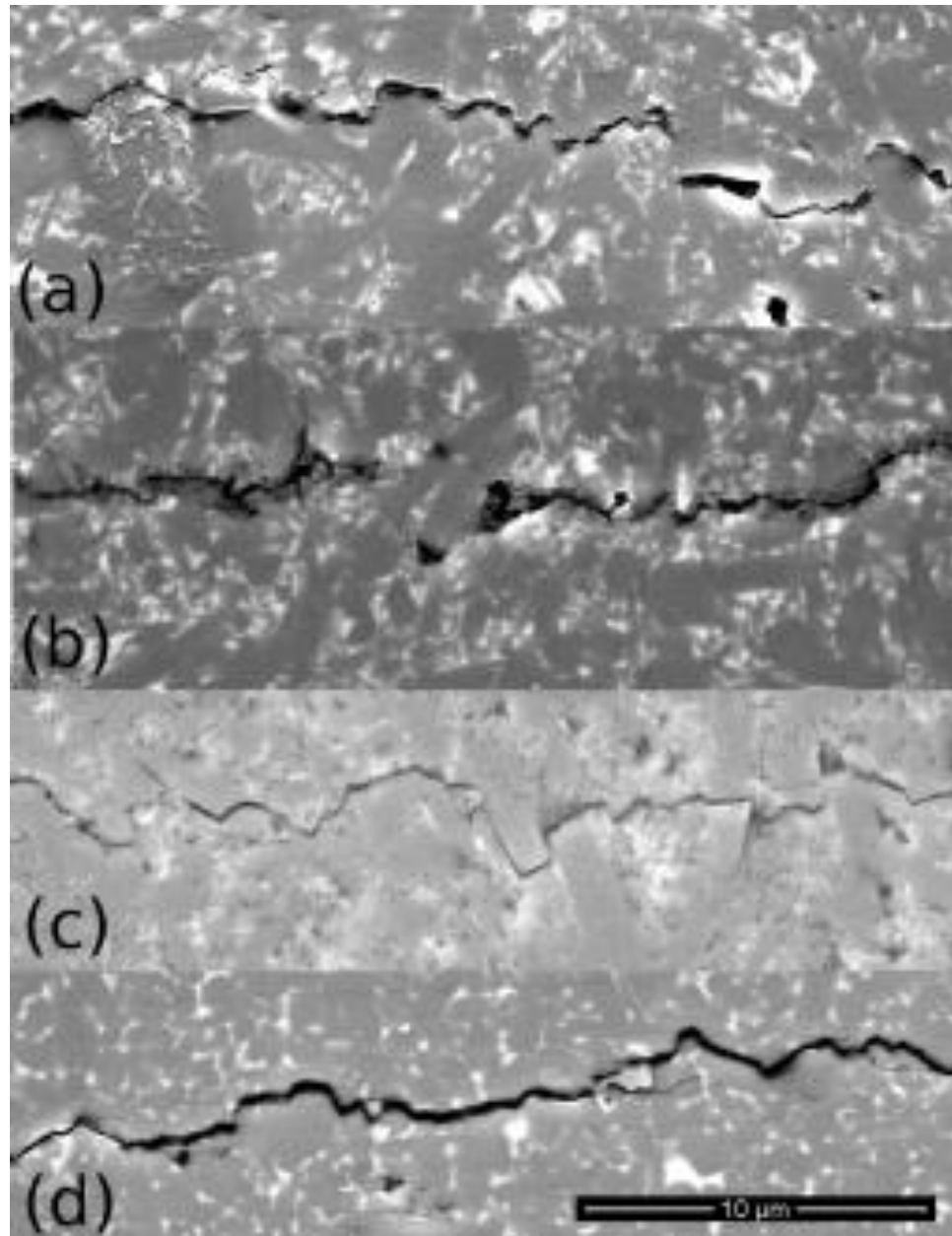


Figure 3.4 Comparison of crack paths in Si_3N_4 , (a) MgY, (b) MgLa, (c) MgLu and (d) AlY

Table 3.1 Mean ΔK_{th} (MPa \sqrt{m}) and Paris Law Exponent, m , values for each material with standard deviation in parenthesis. Homogeneous groups were statistically indistinguishable.

Material	# of Samples	K_{IR} (MPa \sqrt{m})	ΔK_{th} (MPa \sqrt{m})	m	Homogeneous Groups ΔK_{th}	
					1	2
AlY	3	5.57	2.64 (0.02)	18.0 (4.1)	X	
MgY	3	7.32	4.08 (0.22)	20.3 (2.6)		X
MgLu	5	7.00	3.93 (0.06)	16.2 (1.3)		X
MgLa	5	6.55	3.86 (0.09)	19.0 (2.2)		X

Table 3.2 Normalized threshold results summary with standard deviation in parentheses. K_{I0} values were taken from Ref. [1, 2]. Homogeneous groups were statistically indistinguishable.

Material	K_{I0}	K_{br}	$\Delta K_{th}/K_{br}$	Homogeneous Groups $\Delta K_{th}/K_{br}$	
				1	2
				(MPa√m)	
AlY	2.20	3.37	0.783 (0.007)	X	
MgLu	2.00	5.00	0.787 (0.011)	X	
MgY	2.33	4.99	0.817 (0.044)	X	X
MgLa	2.00	4.55	0.849 (0.020)		X

3.5 Discussion

3.5.1 Normalization and comparison of data

Due to the high Paris exponent values in silicon nitride materials (Table 1), growing cracks may accelerate quickly to cause failure. Thus, the use of fatigue crack growth data in mechanical component design should generally focus on avoiding any loadings that would cause stress intensities above the fatigue threshold. Accordingly, the following discussion is centered on comparisons of the fatigue thresholds, ΔK_{th} .

In this study, the materials doped with MgRE showed superior fatigue crack growth resistance compared to the material doped with AlY (Fig. 3.2). Indeed, the threshold stress intensity ranges, ΔK_{th} , differ by more than $1.3 \text{ MPa}\sqrt{\text{m}}$ (Table 1). The data falls into three statistically different, homogeneous groups. The largest apparent difference exists between the materials doped with Al_2O_3 versus those doped with MgO. Within those doped with MgO there are two significantly different groups; however, MgLu is a common member of both groups and the thresholds are all similar ranging from $3.9 - 4.1 \text{ MPa}\sqrt{\text{m}}$. Thus, the apparent difference may result simply from number of the samples in these groups being rather low (3-5). The major differences between the AlY and MgRE materials can largely be explained by differing levels of toughening due to grain bridging. When the data was normalized by the contribution of bridging stress intensity to their *R*-curve, it is observed that the data mostly overlap. The statistical analysis shows the normalized fatigue thresholds for the AlY doped silicon nitride is indistinguishable from the MgY and MgLu silicon nitrides. The MgY and MgLa silicon nitrides were also shown to have no significant difference in their normalized thresholds.

Various normalization parameters have been proposed to produce a roughly universal cyclic fatigue curve for different microstructures of various bridging toughened ceramics including Vickers indent toughness[54] and *R*-curve peak toughness.[48, 62, 63] In this study the best agreement of the data for various microstructures was found when normalizing to the peak bridging stress intensity from the *R*-curve, K_{br} . While all such normalization parameters are somewhat arbitrary,

here it is argued that because degradation of bridging is the fundamental physical process at work, a physically meaningful normalizing parameter should be related solely to that mechanism. Accordingly, normalization with respect to the peak bridging stress contribution represents 100% of the available toughening that can be degraded by cyclic loading.

3.5.2 *Role of Grain Morphology*

The much lower fatigue resistance of the AlY doped silicon nitride can be explained by analysis of the microstructure and how it contributes to the toughening of each material. As can be seen in Figs. 3.1a-d, there is quite a difference in grain morphology of the β -Si₃N₄ grains, especially when comparing the MgO-RE to Al₂O₃ doped AlY silicon nitrides used in this study. Microstructural analysis of the grain distribution of the various microstructures has been published previously (Fig. 3.5a-d)[55] and the large difference between the MgRE and AlY containing silicon nitrides is clearly seen. For the MgRE silicon nitrides the distributions are all similar with large concentrations of long slender grains of length of $\sim 1\ \mu\text{m}$ with high aspect ratios ranging from 7 to 10. There are also more grains of considerably longer length and aspect ratio than in the AlY doped material which, on average, contains grains with smaller aspect ratios mostly in the range of 2-4.

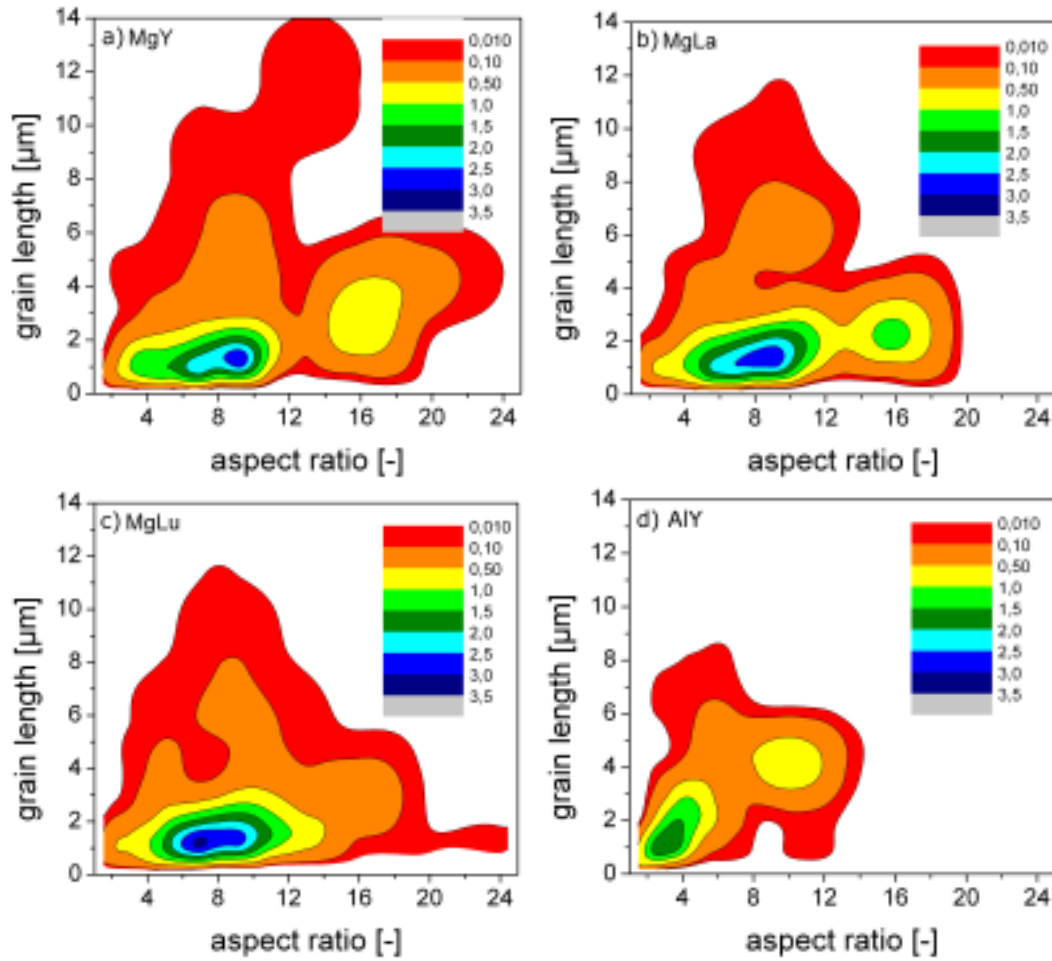


Figure 3.5 Distribution of grain length and aspect ratio of Si₃N₄, (a) MgY, (b) MgLa, (c) MgLu and (d) AlY [55]

As a crack propagates through the material there are generally considered to be three types of bridges that may form to carry loads across the crack wake.[55] The first to form and the most resistant to fatigue are fully intact elastic bridges. Additionally, partially debonded elastic bridges form when a crack deflects but stalls and is unable to propagate around the back side of the grain.[64] Finally, frictional bridges are those that carry stress across the crack solely from frictional contact between the grains. Frictional bridges may form directly from crack deflections and

also when elastic bridges fail. They are also the most prone to wear by the fatigue process. For the macroscopic long crack experiments conducted in the present study the bridging zone is in a steady state condition with older bridges being destroyed while new ones are formed.

The largest contribution to K_{br} is thought to derive from the elastic bridges that are left in the crack wake.[55] Furthermore, it has been reported that the ends of the elongated reinforcing grains have significant shear stress along the boundary making debonding easier.[55] The shear stresses are only significant within 1-2 grain diameters of the end; this, the higher aspect ratio grains in the MgRE silicon nitrides are more likely have a crack intersect them in the middle where shear stresses between the grain and interface are low. This makes formation of elastic bridges more likely. The AlY doped material has a shorter aspect ratio making intersection of the crack closer to the end of the grain where debonding is easier, which will result in a higher fraction of frictional bridges. Fig. 3.4 shows crack paths through each type of material at the same magnification where the more tortuous crack path and larger number of elastic bridge fractures and pullouts can be clearly seen for the MgRE silicon nitrides.

3.5.3 *Role of Intergranular Film*

In addition to affecting the aspect ratio of the β -Si₃N₄ grains, the rare-earth oxide dopants also affect the composition of the intergranular film (IGF). These differences in composition affect the strength and toughness of the intergranular film which in turn affects the *R*-curve behavior and strength of the bulk material.[55, 65] The relative strengths and toughnesses of the IGF and β -Si₃N₄ grains determines the

ease of crack deflection and thus the relative percentage of frictional and elastic bridges that are formed in the wake of the crack. The critical angles of incidence for debonding to occur between the glassy interface and beta-phase grains have been determined in a previous study to be 40° and 60° for the MgLu and MgLa silicon nitrides, respectively.[65] The smaller the critical angle between the advancing crack and β - Si_3N_4 grains, the less likely that crack deflections will occur in the bulk ceramic. Furthermore, these two Si_3N_4 ceramics have approximately identical grain distributions (Fig. 3.5) so the IGF differences should be the only significant factor affecting the crack deflection behavior. Based on the critical angles, it has been estimated that for MgLu doped Si_3N_4 36% of the grains will form elastic bridges without debonding while that number falls to 14% for the MgLa doped Si_3N_4 . [55] These intact grains act as pinning events impeding the growth of the crack and are considered the most potent toughening bridges.

Despite this large difference in critical angle for debonding, both the MgLu and MgLa silicon nitrides have identical fatigue thresholds of $3.9 \text{ MPa}\sqrt{\text{m}}$ for long, macroscopic cracks. Similarly, their reported peak *R*-curves toughness values are also identical after $\sim 50 \text{ }\mu\text{m}$ of crack extension.[55] Unfortunately there is no critical angle data for the AlY silicon nitride because the sample cannot be prepared due to Si_3N_4 and Al_2O_3 reacting to form SiAlON phases. However, based on the results for the MgRE silicon nitrides it is concluded that the IGF plays little role in affecting the fatigue behavior of the silicon nitride ceramics at macroscopic crack sizes with steady state bridging zones.

While the peak *R*-curve toughness values for the MgLu and MgLa silicon nitrides are identical, significant differences are reported in the initial rise of the *R*-curve which also affects their relative strengths.[55, 65] Similarly, it has been reported for an Al_2O_3 ceramic that the *R*-curve becomes more steep with increasing grain boundary adhesion although they reach identical toughness values after some amount of extension.[66] Furthermore, while the steady state, long crack fatigue behavior for that Al_2O_3 was found to be unaffected by the grain boundary phase toughness the behavior at short crack sizes was found to be significantly different.[66, 67] Those studies suggest the tougher IGF leads to a shift in the proportions of the various types of bridges, fully bonded elastic, partially deboned elastic, and frictional. While their summed toughening contribution at long crack sizes may be identical, the different bridges develop at different rates with crack extension affecting the fracture and fatigue behavior at short crack lengths.[55, 65-67]

Overall, it is concluded that the lower grain aspect ratio, and not the differing intergranular film composition, is the dominant factor governing the lower macroscopic, steady state fatigue crack growth resistance observed for the AlY silicon nitride in this study. However, it is expected that the intergranular film may play a significant role in affecting the fatigue crack growth behavior during the transient regime of bridging zone development. However, because the bridging zone is very short in silicon nitrides (10s of micrometers), fatigue behavior of such short cracks is not easily investigated due to challenges initiating, and monitoring the growth rates of, cracks on that size scale.

3.6 Conclusions

Based on a study of the fatigue long crack growth behavior of four silicon nitride ceramics with different sintering additives and microstructures the following conclusions can be made:

- 1) In this study it was found the best normalization for uniting the data into a single universal crack growth curve for all microstructures was achieved by normalizing to the bridging stress intensity, K_{br} . This normalization recognizes that bridging degradation is the fundamental physical process causing crack growth and K_{br} is physically meaningful in that it represents 100% of the available toughening that can be degraded.
- 2) The fatigue crack growth resistance of long cracks with steady state bridging zones is higher for silicon nitrides doped with $\text{MgO-RE}_2\text{O}_3$ ($\text{RE} = \text{Y, La, Lu}$) sintering additives than the one doped with $\text{Al}_2\text{O}_3\text{-Y}_2\text{O}_3$ additives. This difference was attributed to the higher grain aspect ratio observed for all of the $\text{MgO-RE}_2\text{O}_3$ doped silicon nitrides.
- 3) The intergranular film has little effect on the fatigue crack growth resistance of long cracks with steady state bridging zones of silicon nitrides. However, this conclusion may not be true for shorter cracks with developing bridging zones due to the different rates at which various types of bridges develop.

**A direct comparison of non-destructive techniques for determining
bridging stress distributions**

R. B. Greene, S. Gallops, S. Fünfshilling, T. Fett, M. J. Hoffmann, J. W. Ager III,
J. J. Kruzic

Journal of the Mechanics and Physics of Solids

4 A direct comparison of non-destructive techniques for determining bridging stress distributions

4.1 *Abstract*

Crack bridging is an important source of crack propagation resistance in many materials and the bridging stress distribution as a function of crack opening displacement is widely believed to represent a true material property uninfluenced by sample geometry, loading conditions, and other extrinsic factors. Accordingly, accurate measurement of the bridging stress distribution is needed and many non-destructive methods have been developed. However, there are many challenges to accurately determining bridging stresses. A comparison of bridging stresses measured using *R*-curve, crack opening displacement (COD), and spectroscopy methods has been made. The COD method is surface sensitive and gives a lower peak bridging stress compared to the *R*-curve technique which samples through the entire material thickness. This is attributed to a more compliant near surface bridging zone. Conversely, when *R*-curves rise steeply over the first few microns of growth from a notch, an effect of negative T-stress is expected to raise the *R*-curve determined peak bridging stress. Spectroscopy methods were only found to yield reliable bridging stress results if a reasonable through thickness volume of material is sampled. It was found that 2.5% of the specimen thickness achieved using fluorescence spectroscopy appears adequate for Al_2O_3 while 0.1 – 0.2% of the sample thickness achieved using Raman spectroscopy for Si_3N_4 appears inadequate. Overall it is concluded that in the absence of T-stresses a bridging distribution can be determined that is a true material

property. Also, a new method is proposed for determining the bridging stresses of fatigue cracks from 1) the bridging stress distribution for monotonically loaded cracks and 2) experimental fatigue data.

4.2 Introduction

Crack bridging is an important source of crack propagation resistance in many engineering materials including reinforced brittle and ductile matrix composites [68, 69], laminated composites [70], grain bridging monolithic ceramics [35, 71], and multi-phase metallic/intermetallic alloys [72, 73]. It is also important in many biological materials such as bone and dentin [74, 75]. When modeling the effects of bridging on the fracture behavior it is generally useful to adopt a continuum approach. This effectively smoothens out the many discrete load bearing bridges into a continuous bridging stress distribution, $\sigma_{br}(\delta)$ (Fig. 4.1), where the bridging stresses depend on the local crack opening displacement, δ [76-78]. This relationship is widely believed to represent a true material property uninfluenced by sample geometry, loading conditions, and other extrinsic factors. As such, it substantially controls the mechanical properties of these materials and can be used in conjunction with fracture mechanics weight functions to evaluate mechanical properties that are dependent on geometry and loading conditions such as fracture resistance curves (*R*-curves) for different crack geometries [79].

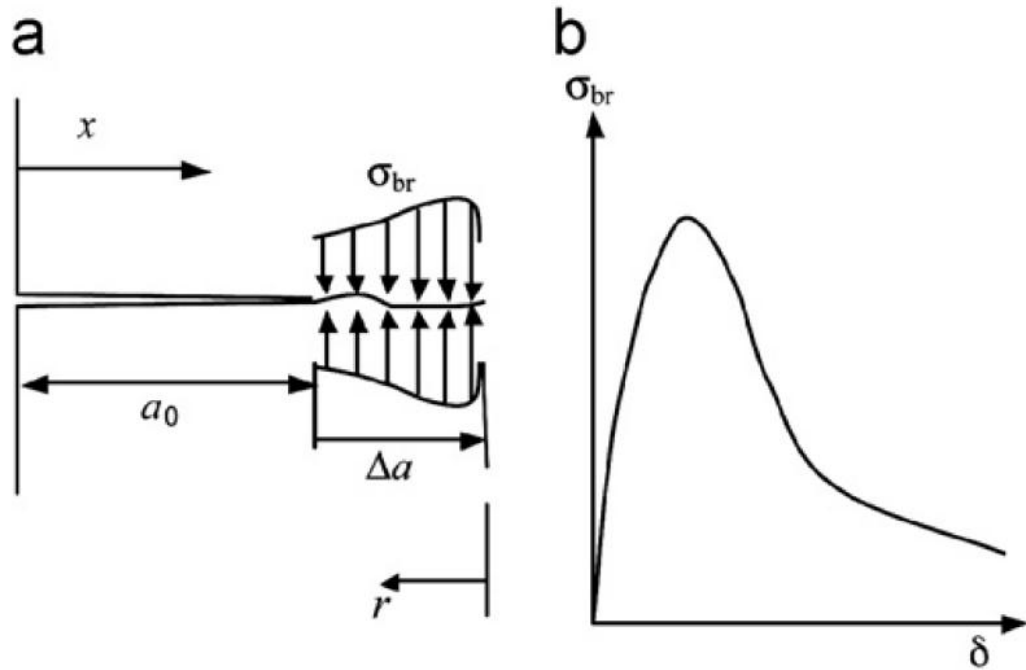


Figure 4.1 a) Schematic representation of a crack in a material exhibiting crack surface interactions by bridging stresses, b) bridging stress distribution versus crack opening displacement, δ .

Many techniques have been employed to measure bridging stress distributions and they may be broadly classified as non-destructive or destructive. The multi-cutting compliance technique is destructive and involves measuring the compliance after incremental saw cuts are made into the wake of a bridged crack [9, 80, 81]. Another destructive approach is to machine small post fracture tensile specimens by sectioning larger cracked ceramic or fiber composite specimens [82-85]. The post fracture specimens are oriented such that they span the crack wake of the larger specimen and thus each one contains a portion of the original bridged, through-thickness, crack which can then be tensile tested. In addition to these techniques being destructive,

another limitation is their spatial resolution which is limited by the size scale of the micromachining needed to make the incremental cuts or post fracture specimens.

Conversely, several non-destructive techniques for determining bridging stresses involve calculations using weight functions [78, 86, 87]. The relationship between crack opening displacement and stress allows bridging stress profiles to be computed from crack opening displacement (COD) profiles [86], which can be measured using various methods such as with a scanning electron or atomic force microscope. Similar to the non-destructive methods described above, the sample must be held under an applied crack opening load which leads to several instrumentation difficulties. Another limitation of the COD based methods is that COD profiles can be difficult to accurately measure—especially for small or tortuous cracks.

The relation between the stress intensity factor and the bridging stresses also allows the bridging stress profile to be determined directly from the measured *R*-curve [78, 87]. While such methods have been traditionally very computationally expensive, recently approximations have been developed that significantly reduce the computational time [55, 88]. The accuracy of *R*-curve based methods can be limited by the ability to accurately measure the most important initial portion of steeply rising *R*-curves [1, 65]. Overall, weight function based techniques have been applied to a wide range of fiber reinforced composites and monolithic ceramics [9, 86, 87, 89-96].

Light spectroscopy methods (e.g., Raman or fluorescence based) are also non-destructive and have been frequently used to measure bridging stresses in various ceramics, composites, and even bone where specific spectrum peaks are affected by

stress. Fluorescence spectroscopy is a common method for determining stresses in Al_2O_3 containing materials by measuring the shift from their stress-free position in the characteristic R1 and R2 Cr^{3+} optical fluorescence lines produced by chromium impurities [97, 98]. Since chromium is a ubiquitous substitutional impurity in alumina and sapphire, microprobe fluorescence spectroscopy has been used successfully for measuring bridging stresses in alumina and alumina-containing composites by moving a focused laser along the bridging zone of the crack [91, 99-102]. A limitation of this technique is that the material to be studied must fluoresce and to date studies have been generally limited to alumina-containing materials.

Similarly, certain Raman spectrum peaks shift to lower wave numbers by the application of tensile stress. Accordingly, Raman microprobe spectroscopy has been employed in a manner similar to fluorescence techniques to determine bridging stress profiles in a wider range of materials including fiber reinforced polymer and ceramic matrix composites, Si_3N_4 ceramics, and even bone [8, 34, 103-107]. Some limitations of Raman spectroscopy are that it cannot generally be used for metallic materials because fluorescence signals from the material or impurities hide the relatively weak Raman signal. Another challenge is that data collection times can be long relative to fluorescence potentially causing data scatter due to thermal drift of the peak.

Finally, another non-destructive technique involves using synchrotron X-ray micro-diffraction to measure local crystal lattice strains, such as has been used in titanium matrix composites [108]. A major advantage of this technique is that any crystalline material can be studied; however, the necessity for a synchrotron X-ray

source makes this technique impractical for day-to-day measurements of bridging stress distributions. Also, common to X-ray diffraction and light spectroscopy microprobe methods is that the sample must be held under an applied crack opening load which requires specialized in-situ testing stages and may result in subcritical crack growth affecting the results.

Despite the large amount of research on bridging stresses, to date there is a scarcity of information on how the results from various methods compare to one another. One recent comparison of independently measured bridging stresses for an Al_2O_3 ceramic is very encouraging [7]. Indeed, bridging stresses for a fatigue crack were determined by fluorescence spectroscopy and from the *R*-curve and the results agreed well (Fig. 4.2).

However, there are many challenges to accurately determining bridging stresses that will be addressed in the present paper. Accordingly, it is the goal of this paper to compare results from several non-destructive techniques that are relatively easy to implement in most laboratories, including the calculation of bridging stresses from *R*-curves and CODs and both fluorescence and Raman micro-spectroscopy. New results are presented for Si_3N_4 and Al_2O_3 ceramics and are compared with published results for both *R*-curve and fatigue generated cracks. Furthermore, a new method is proposed for deducing the bridging stress distribution for fatigue cracks in situations where other methods have been found to be problematic. The results of this study provide new insight into the limitations and advantages of the various techniques and will aid researchers in choosing appropriate methods for given situations.

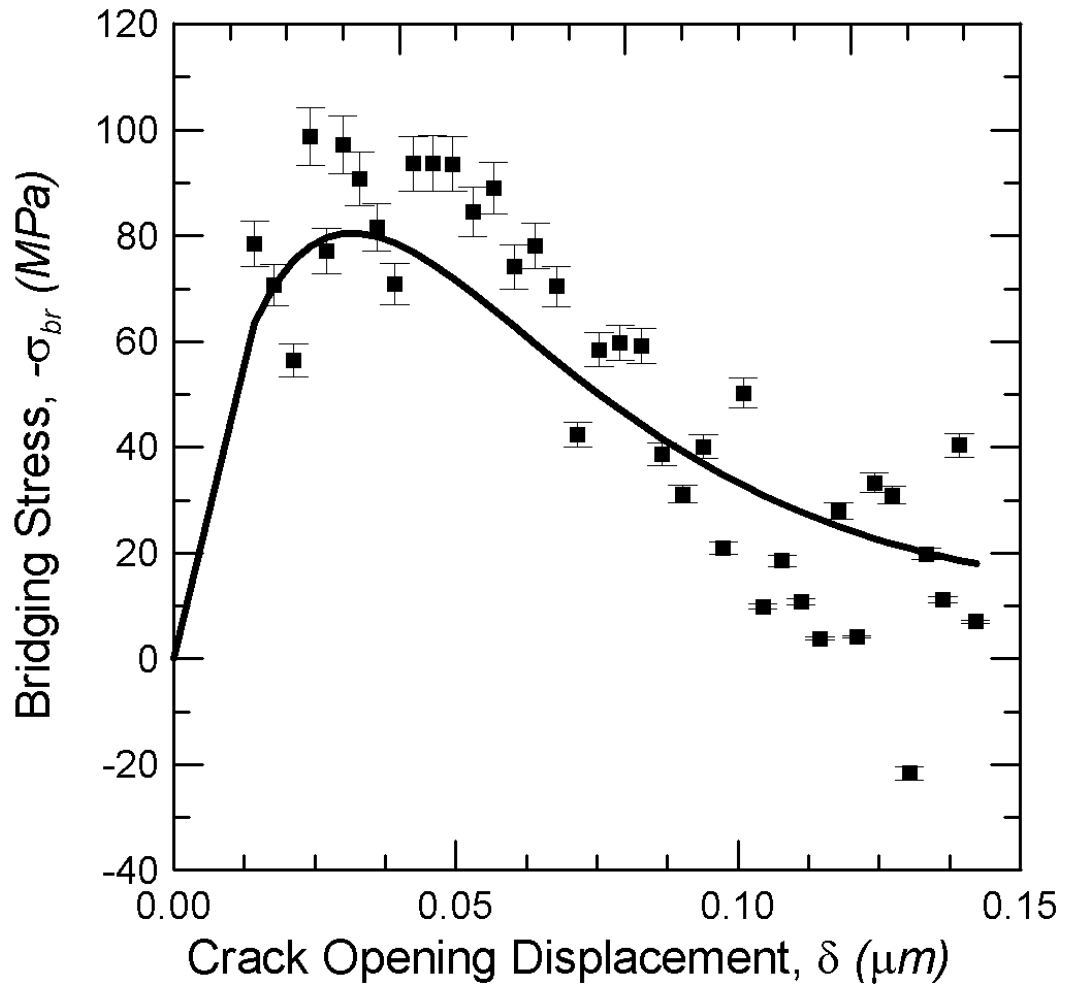


Figure 4.2 Fatigue crack bridging stress distribution for a 99.5% pure Al_2O_3 calculated from weight functions and the fatigue threshold R -curve (solid line). Also plotted are bridging stresses measured using fluorescence spectroscopy (solid circles) with error bars indicating ± 1 standard deviation based on the standard deviation of the linear calibration fit. Figure reproduced with permission from [7].

4.3 *Experimental Methods*

4.3.1 *Materials*

Bridging stresses are examined for two different materials: a hot-isostatically pressed silicon nitride containing 5 wt% Y_2O_3 and 2 wt% MgO as sintering aids and a commercial 99.5% pure Al_2O_3 (CoorsTek AD995). Full details on the processing of the silicon nitride may be found elsewhere [57], but briefly, powders were prepared by attrition milling in isopropanol and the slurries were subsequently dried and the powders sieved. Green bodies were uniaxially pressed and then subsequently cold-isostatically pressed at a pressure of 400 MPa. The samples were sintered in a hot-isostatic-press (HIP) with a two-step sinter-HIP process, where closed porosity is obtained at low N_2 pressures during the first sintering step and full density was achieved during the subsequent HIP step at a maximum nitrogen pressure of 10 - 20 MPa. Full density (water immersion method) is defined here for relative densities greater than 99% of theoretical density, which was calculated by the rule of mixture based on the starting compounds. The silicon nitride features elongated β -phase grains with an average diameter of 0.28 μm with an aspect ratio of ~ 7 . The alumina ceramic is the same as in Fig. 4.2 and in [7, 67]. It has nominally equiaxed grains widely ranging in size with a majority having cross-sectional areas of $< 63 \mu\text{m}^2$ (or diameter of $< 9 \mu\text{m}$). Information on the grain size distribution may be found in [67].

4.3.2 Bridging stresses from crack opening displacements (CODs)

A procedure that allows the bridging stresses to be determined from crack opening displacement (COD) measurements was developed previously [86]. The bridging stresses, σ_{br} , acting against crack opening depend on the opening displacements, δ . From the measured R -curves the bridging stress intensity factor, K_{br} , is known since

$$K_R = K_{I0} - K_{br}, K_{br} < 0 \quad (1)$$

Any stress intensity factor can be represented by a stress distribution acting in the wake of the crack (Fig. 4.1a). Accordingly, using the weight function representation the bridging stress intensity factor is given by

$$K_{br}(Da) = \int_0^{Da} h(r, a) S_{br}(r) dr \quad (2)$$

with the fracture mechanics weight function, h , for the appropriate geometry [109], the distance, r , from the tip, the initial crack length, a_0 , free of bridging, and the crack extension, $\Delta a = a - a_0$. The total crack opening displacement, δ , can be computed as the sum of the displacement that would occur due to an applied load for non-bridging specimen, δ_{appl} , and the displacement (which is a negative value) due to the effects of the bridging toughening mechanism, δ_{br} , by

$$\delta = \frac{1}{E'} \int_{a-r}^a h(r, a') K_{appl}(a') da' + \frac{1}{E'} \int_{a-r}^a h(r, a') \left[\int_{a-r}^{a'-a_0} h(r', a') S_{br}(r') dr' \right] da' \quad (3)$$

Using Equations 1-3 the bridging stress distribution $\sigma_{br}(\delta)$ may be determined.

For this purpose the simple set-up for the unknown relation can be made by

$$S_{br} \gg \underset{(n)}{\ddot{a}} S_n \frac{d}{d_n} \exp[-d/d_n] \quad (4)$$

This bridging stress relation is inserted into Eqs. (2) and (3). A solution of this system of integral equations is found by systematic variation of the free parameters in (4) under the condition that the resulting $\delta(r)$ function must coincide with the measured CODs and thus provide the best set of unknown parameters σ_n and δ_n .

To compare with bridging stress results determined from fracture R -curves published in the literature for notched bend beams [55, 60], the above procedure was used to determine $\sigma_{br}(\delta)$ for a Si_3N_4 compact tension sample used to measure a fracture toughness R -curve in a previous paper [65]. The K_{I0} value used ($2.3 \text{ MPa}\sqrt{\text{m}}$) was taken from the published literature and determined from the crack tip opening displacements of Vickers indent cracks [110].

4.3.3 Fatigue threshold experiments

New fatigue threshold experiments were conducted for the Si_3N_4 material using standard compact-tension, C(T), specimens (width, $W \approx 19 \text{ mm}$; thickness, $B \approx 3.5 \text{ mm}$) in general accordance with ASTM standard E647 [111]. More complete details of the fatigue-crack growth procedures are in [8, 9] while a brief summary of issues pertinent to the measurement of fatigue thresholds is presented here. Fatigue cracks were initiated from straight machined notches (length $a_0 \approx 4 - 5 \text{ mm}$) under cyclic loading conditions ($\nu = 25 \text{ Hz}$ frequency sine wave, load ratio, $R = P_{\max}/P_{\min} = 0.1$), after which the cracks were grown to a specified length, as monitored using back-face strain compliance methods [112]. Specimens were razor micro-notched to have

root radii, $\rho < 10 \text{ }\mu\text{m}$. This was done by repeatedly sliding a razor blade over the notch in the presence of a $1 \text{ }\mu\text{m}$ diamond paste. Data collection did not begin until the crack was growing evenly (both sides within 10% of each other) and the amount of fatigue-crack extension from the notch, Δa_f , exceeded ρ , at which point the influence of the notch field on the stress intensity could be considered to be negligible [113, 114].

Fatigue crack growth rates were measured as a function of the applied stress intensity range, $\Delta K = K_{\max} - K_{\min}$, where K_{\max} and K_{\min} are the maximum and minimum stress intensity experienced during the loading cycle. In order to measure the fatigue threshold, the applied stress-intensity range was reduced at a roughly constant ΔK -gradient ($= [d\Delta K/da] / \Delta K$) of -0.08 mm^{-1} . In this manner the fatigue threshold ΔK_{TH} was taken as the lowest stress intensity at which the fatigue-crack growth rate could be measured and does not exceed $\sim 10^{-10} \text{ m/cycle}$. For this Si_3N_4 material the bridging zone is known to be only 10s of micrometers in length [55, 60] and a determination of fatigue thresholds during the bridging zone development and the fatigue threshold R -curve $\Delta K_{\text{TH}}(\Delta a)$, as was done in [7] for Al_2O_3 , was impossible. Rather, the steady state fatigue threshold, ΔK_{TH} , was determined for a fully developed bridging zone.

4.3.4 Spectroscopy

4.3.4.1 Bridging Stress Measurements

The Raman microprobe technique was used to measure bridging stresses for C(T) fatigue samples that were last tested near the fatigue threshold. The specimens were re-loaded *in situ* to $\sim 95\%$ of the K_{\max} value at the measured fatigue threshold,

K_{\max}^{TH} . A 488-nm laser was focused using an optical microscope with a 50X objective to a $\sim 1 \mu\text{m}$ spot size on the sample surface. Laser power at the surface was kept below 7 mW to avoid measurement drift due to sample heating. Scattered light was directed through a holographic laser line filter and into a 640 mm single spectrometer using a liquid-nitrogen cooled, back-thinned CCD camera. There were two different colors of silicon nitride specimens: black and light-grey. Their mechanical properties were unaffected by color but the optical properties deemed that longer exposures were required for the darker specimens. For the darker specimens 360 s exposures were used while for the lighter color specimens only 120 s exposures were required to get equivalent peak intensity.

Peak shifts in silicon nitride were first measured along the crack wake at small increments of $2 \mu\text{m}$ starting ahead of the crack tip to focus on the detail of the peak bridging stresses. Larger increments of 4 and $6 \mu\text{m}$ were used as measurements progressed along the crack wake until bridging stresses decreased to zero after about $200 \mu\text{m}$. Effects due to ambient temperature variations and/or instrument drift were minimized by recalibrating using an internal zero stress reference (a part of the sample far away from the crack). These zero points were taken after every ~ 5 measurements.

Results were analyzed in an identical fashion. First, any spikes in the spectra due to cosmic rays were removed manually and then a seven-point, third-order Savitsky-Golay smoothing method was applied. A rolling-ball technique was then adopted to remove the background [115]. Next, the peak of interest was isolated from the rest of the spectrum and a Gaussian curve-fit was used to determine the peak

location in cm^{-1} . In order to calculate the peak-shift, the zero stress peak position corresponding to each bridging stress measurement was determined by simple linear interpolation between the associated calibration points before and after the measurement. The peak-shift was then the difference of the measured peak location and its associated zero calibration. The bridging stress at each point was determined by dividing the calculated shift by a calibration factor and then linearly scaling the stress up to 100% to account for loading the sample to only 95% of the maximum load at threshold. A series of experiments were conducted at different loading levels to verify that this liner extrapolation was a reasonable approximation.

The resulting bridging stress values from Raman results were fitted according to

$$\sigma_{br} = \sigma_0 \frac{r}{r_0} \exp\left(\frac{-r}{r_0}\right) + \sigma_1 \frac{r}{r_1} \exp\left(\frac{-r}{r_1}\right), \quad (5)$$

and then converted to terms of δ using the Irwin approximation for the near-tip behavior ($r \rightarrow 0$)

$$d_{tip} = \sqrt{\frac{8r}{\rho} \frac{K_{I0}}{E'}} \quad (6)$$

4.3.4.2 Stress Calibration

Because the stress dependence of the Raman shift of the 862 cm^{-1} peak for Si_3N_4 can be affected by changes in chemical composition [104] a calibration was performed for our sample composition using a 2 mm by 3 mm cross-section beam in three-point bending at a peak stress of $\pm 500 \text{ MPa}$. The laser was moved in $160\text{-}\mu\text{m}$ increments along the bend beam to record the peak shift with changing stress, again

using an internal zero stress reference, as described above, which was recalibrated every five measurements. This calibration gave an average piezo-spectroscopic coefficient, Π_{avg} , of $-1.57 \pm 0.22 \text{ cm}^{-1}/\text{GPa}$. This value falls near those obtained by Pezzotti *et al.* for Si_3N_4 materials sintered with Al_2O_3 which contain SiAlON phases (-1.63 to -1.69 $\text{cm}^{-1}/\text{GPa}$) [34, 104].

4.3.4.3 Sampling Volume Determination

To allow a comparison of the present Raman spectroscopy results for Si_3N_4 with the fluorescence spectroscopy results shown in Fig. 4.2 from [7] the laser sampling volumes were determined for both materials. The sampling volumes were calculated based on the absorption coefficients measured using thin samples. To analyze the absorption of the silicon nitride a green laser ($\lambda = 533 \text{ nm}$) was used. This laser is near both the probe wavelength (488 nm) and the wavelength of the Raman peak (510 nm) to give a reasonable estimate of the absorption coefficient. For the absorption of alumina both the green light absorption and red light absorption was examined. The fluorescence peak of alumina occurs at about 677 nm and the second laser used had a wavelength of about 680 nm. It was determined that the absorption at 533 nm was the limiting factor; accordingly, that laser was used for both materials.

The intensity of the transmitted laser light was measured after passing through thin sections of material. For Si_3N_4 , which is opaque, thin sections of 42 – 79 μm were used. For Al_2O_3 , which is translucent, thicker sections of 813 and 1096 μm were used. The absorption coefficient was calculated from the relation,

$$\frac{I}{I_0} = e^{-\alpha t} \quad (7)$$

where I is the intensity of the incident light, I_0 is the intensity of the transmitted light, α is the absorption coefficient, and t is the thickness of the specimen. The Raman probe depth is then calculated by the simple relation

$$depth = \frac{1}{2\alpha} . \quad (8)$$

By applying a Gaussian beam approximation the shape of the sampling volume of the laser in the material was estimated. The shape of the beam spread into the material, $w(z)$, was calculated using the following,

$$w(z) = w_0 \sqrt{1 + \left(\frac{z\lambda}{\pi w_0^2} \right)^2} , \quad (9)$$

where w_0 is the beam waist, or half the spot diameter focused on the surface of the sample, z is the depth into the sample, and λ is the wavelength of the probe laser. The shape of the maximum penetration of the laser was assumed to be a simple circular arc. Sampling volume was determined by integration of the beam profile about the axis of penetration.

4.4 Results

4.4.1 Bridging stresses from crack opening displacements and R -curves (Si_3N_4)

Figure 4.3a shows crack opening displacement measurements on the side surface of an C(T) specimen previously used in [65] to measure a fracture R -curve under a monotonically increasing load. The open circles represent the CODs for a sample held at roughly 97.5% of the maximum load where $K_R=6.76 \text{ MPa}\sqrt{\text{m}}$, i.e. at $6.59 \text{ MPa}\sqrt{\text{m}}$. For the evaluation of these data, the weight function for the C(T) specimen was used in Eq.(3) as available from fracture mechanics handbooks (e.g. [109]).

The measured surface data are obtained under plane stress conditions. The dashed curve in Fig. 4.3a shows δ_{appl} . Solution of Eq.(3) yields the displacements given by the solid curve in Fig. 4.3a that matches the experimental data (circles). The final result of the computations, namely $\sigma_{br}(\delta)$, is represented in Fig. 4.3b as the solid curve. In addition, Fig. 4.3b shows the result directly from the R -curve measured using a notched four-point bend beam specimen [55, 60]. Analysis for the C(T) R -curve from [65] was not conducted because that R -curve rises very steeply and the C(T) technique did not measure the rising portion adequately. This shortcoming prompted the development of new R -curve methods using bend beams described in detail in [1].

The comparison of the bridging laws exhibits rather strong differences. The peak bridging stress from COD measurements is significantly lower than with the the R -curve evaluation. The peak stresses are -1700MPa for the notched bending bar and -

1200MPa for the CT-specimen. In this context, it has to be mentioned that the bridging stresses from the R -curve evaluation was considered more sensitive than the COD evaluation due to the higher spatial resolution of the data collection that was possible for the smallest opening displacements.

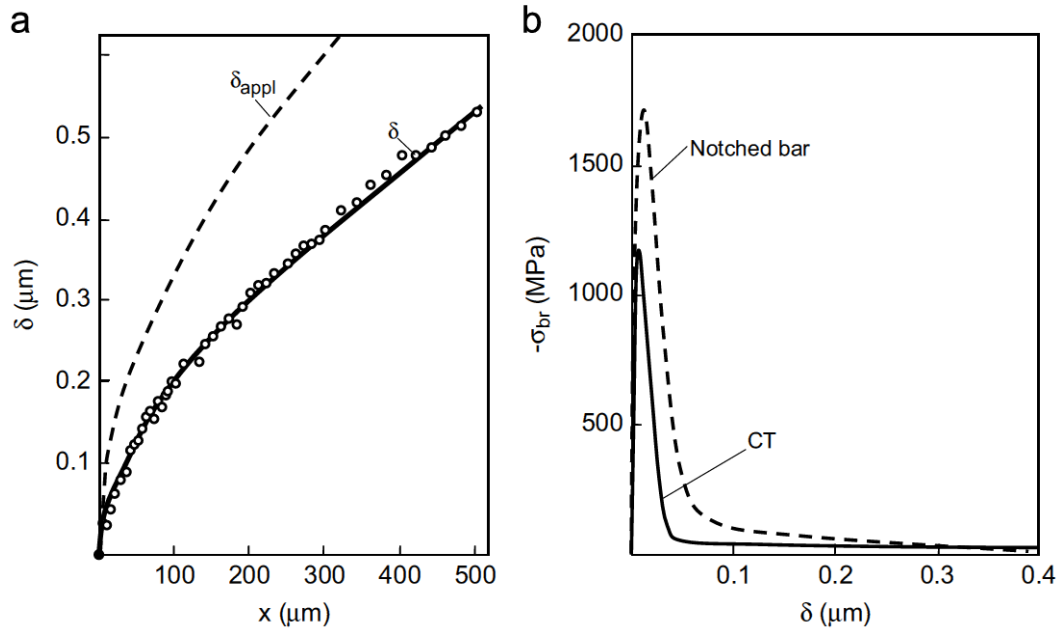


Figure 4.3 a) COD results at the surface of a crack in a C(T) specimen (circles: measurements, dashed curve: applied displacements, solid curve: result of eq.(3) matched to the measured data), b) bridging stresses for the different test specimens.

4.4.2 Fatigue crack bridging stress results (Si_3N_4)

Based on six fatigue threshold experiments using five C(T) samples a mean \pm standard deviation fatigue threshold of $\Delta K_{\text{TH}} = 4.1 \pm 0.2 \text{ MPa}\sqrt{\text{m}}$ was determined. There was no significant difference between the differently colored samples. Fig. 4.4a shows example Raman bridging stress data collected for an individual black silicon nitride fatigue specimen along with its curve fit using Eq. (5). Fig. 4.4b shows all

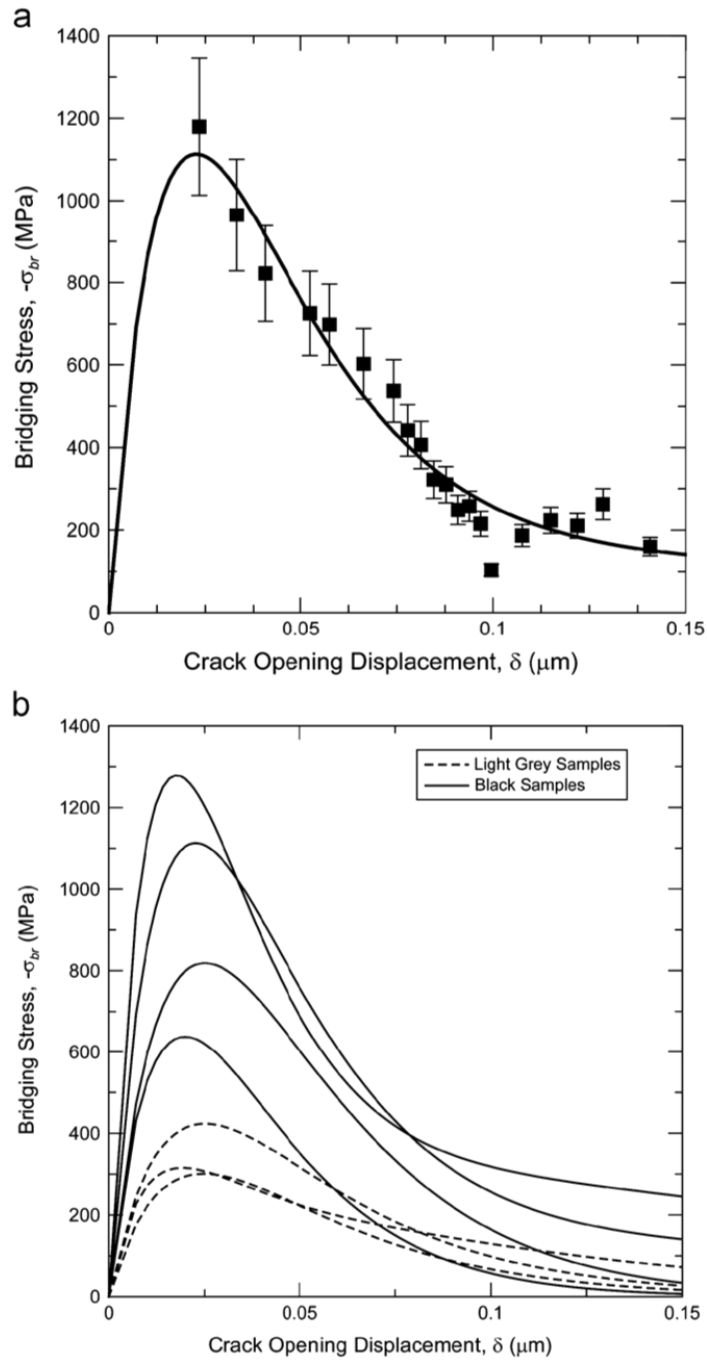


Figure 4.4 a) Bridging stress distribution data determined for a single specimen along with the associated fit using Eq. 5. Error bars indicate the standard deviation for the calibration constant. b) Fits of the bridging stress data for all specimens showing the difference in peak stress between the light-grey and black specimens.

curve fits for the black and light-grey silicon nitride fatigue samples. As can be seen, all of the black sample data lies at much higher stress values than the light-grey specimens. The light-grey specimens also exhibit much less scatter.

4.4.3 Estimating the fatigue threshold bridging stress distribution for Si_3N_4

Due to the high degree of scatter in the stress distributions shown in Fig. 4.4b, a best estimate of bridging stresses for fatigue in silicon nitride was deduced as shown in Fig. 4.5. This distribution was obtained by reducing the peak magnitude of the published bridging stress distribution obtained from *R*-curve *fracture* experiments [1] to account for the *fatigue* degradation of the bridging stresses in the present case. It was decided to use these data because they were collected using the most sensitive measurement method for the smallest crack openings and thus it is expected the distribution shape is most accurate. Also, as will be discussed below the *R*-curve method gives a better through thickness average of the bridging stresses than the surface sensitive COD method. Since the peak stress is being lowered, the differences in peak magnitudes between methods are not a significant concern. The maximum stress intensity of the loading cycle at the fatigue threshold,

$$K_{TH}^{\max} = DK_{TH} / (1 - R), \quad (10)$$

was calculated and used as a known value to decrease the magnitude the bridging stress distribution until the correct value of K_{br} was achieved via Eq. (2) noting that

$$K_{br} = K_{I0} - K_{TH}^{\max} \quad (\text{where } K_{br} < 0) \quad \text{according to Eq. (1).}$$

The crack tip toughness, K_{I0} , was again taken to be $2.3 \text{ MPa}\sqrt{\text{m}}$.

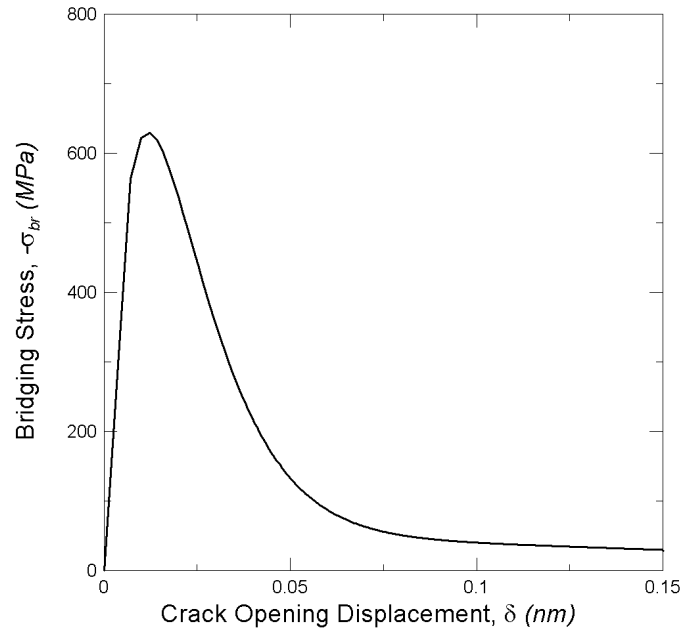


Figure 4.5. The deduced best estimate of the fatigue threshold crack bridging stress distribution for Si_3N_4 .

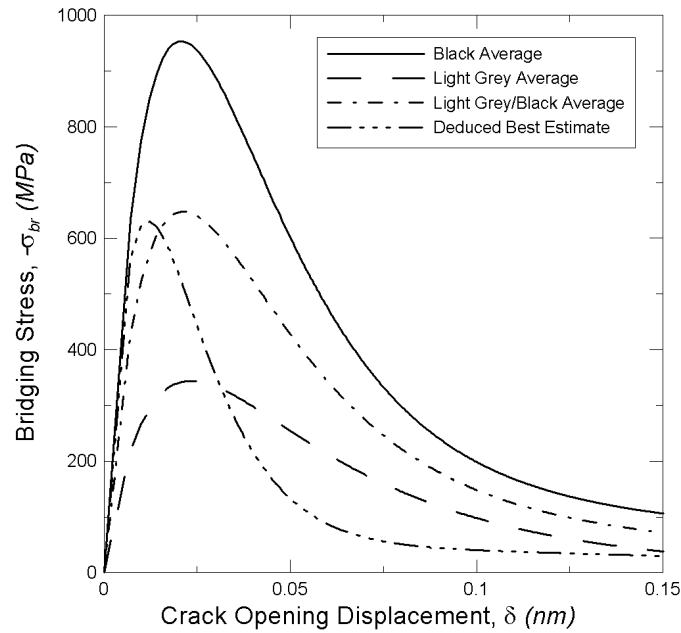


Figure 4.6 A comparison of the average Raman determined fatigue threshold crack bridging stress distributions for Si_3N_4 . Averages for the black samples (solid line), light grey samples (dashed line), and all samples (dash-dot line) are shown. Also shown is the deduced best estimate from Fig. 4.5 (dash-triple-dot line).

Fig. 4.6 compares the averages for the light-grey, black, and all specimens as well as the deduced best estimate of the fatigue-threshold bridging stress distribution from Fig. 4.5. Of interest to note is that the best estimate and the total sample average have a similar peak stress values, while the best estimate and light-grey average have similar areas under their curves.

4.4.4 *Sampling volume results*

The sampling volume for silicon nitride differed based on the color of the material. The volume for the white specimens was determined to be $56 \mu\text{m}^3$ with a depth of $7.2 \mu\text{m}$ equating to ~ 25 average grain diameters. For the black specimens the volume was $30 \mu\text{m}^3$ with a depth of $5.0 \mu\text{m}$ equating to ~ 18 average grain diameters. These depths of penetration correspond to only $\sim 0.1 - 0.2\%$ of the total sample thickness. The sampling volume for alumina was calculated to be $23,645 \mu\text{m}^3$ with a depth of $84 \mu\text{m}$, or $\sim 2.5\%$ of the total sample thickness. Fig. 4.7a shows the laser sampling volume cross-section for the silicon nitride samples and Fig. 4.7b shows the sampling volume cross-section for the alumina samples compared to that of the silicon nitride samples. For the alumina samples the percentage of the thickness sampled was more than an order of magnitude higher than for the Si_3N_4 samples.

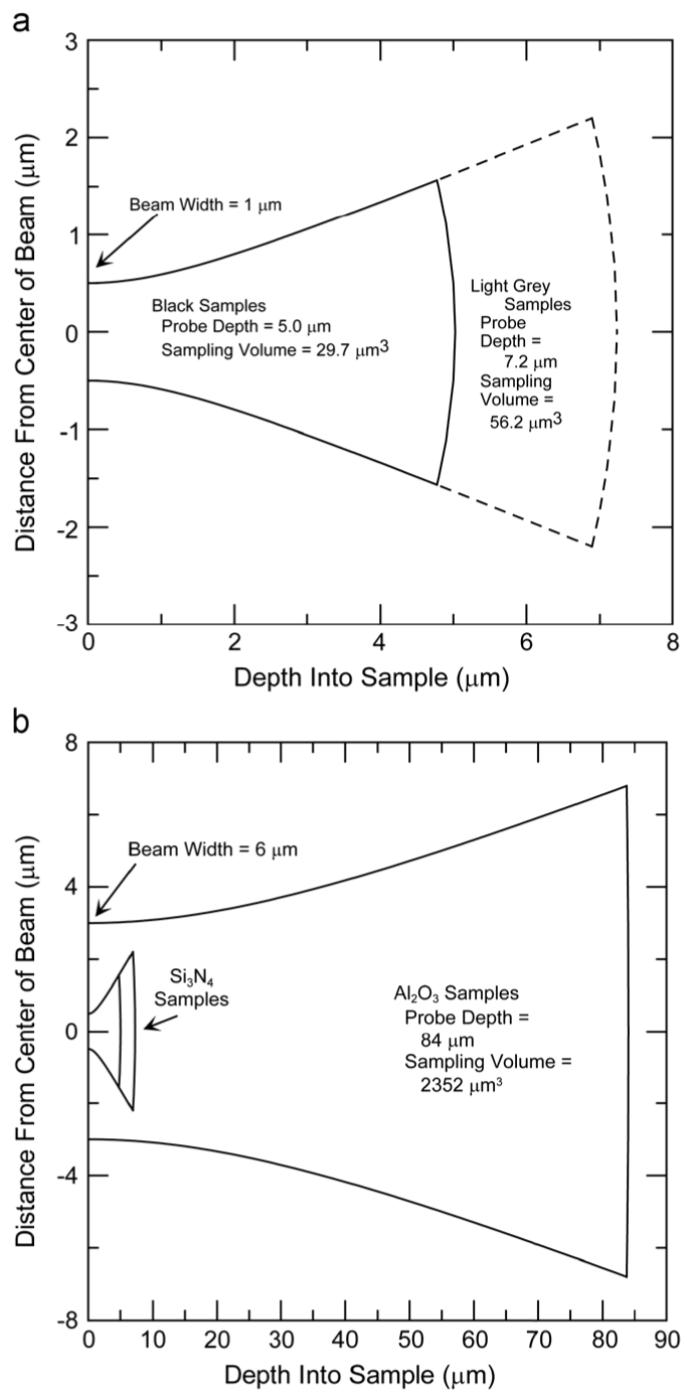


Figure 4.7 a) A comparison of the Raman spectroscopy sampling volumes for the black and light grey Si_3N_4 samples. b) A comparison of the Raman sampling volume for the Si_3N_4 samples with the fluorescence sampling volume for the Al_2O_3 samples.

4.5 Discussion

Two types of cracks have been examined in this study, those produced under monotonically increasing loading conditions and those produced under cyclic fatigue loading conditions. From the perspective of bridging stresses the fatigue cracks should always show lower peak bridging stress magnitudes due to the cyclic degradation of bridges. A quick comparison of Figs. 4.4b and 4.6 demonstrate this clearly. However, it is expected that bridging stress results should be consistent for a specific type of crack, as has been shown for alumina in Fig. 4.2 [7].

From the present results it is apparent that several difficulties can occur when determining the bridging stresses for Si_3N_4 . Firstly, two different peak stresses were obtained for bend and C(T) samples for cracks grown under monotonically increasing loading conditions. Secondly, the bridging stresses measured using Raman spectroscopy were highly scattered in peak stress from sample to sample, especially for the darker samples. The following discussion will focus on explaining these phenomena.

4.5.1 Effect of the free surface

A model for the bridging mechanism in silicon nitrides with very steep R -curves was proposed in [55]. These Si_3N_4 ceramics consist of 100% β -phase crystals with needle-like grains of high aspect ratio. Such a needle with length axis oriented at an angle of Θ relative to the plane of a crack terminating at the elongated crystal is schematically shown in Fig. 4.8a. A free surface must have an important influence on the bridging stresses because the grains located close to this surface undergo a reduced

“clamping” force by residual stresses caused by thermal expansion anisotropy of the grains. The consequence is increased debonding and the generation of a free neck around the crystal circumference which results in a more compliant structure at the surface.

Due to the missing thermal mismatch stress component normal to the free surface (Fig. 4.8b) also the pull-out resistance of the frictional bridges is reduced as can be concluded from the friction model by [40], Fig. 4.8c. Note that the illustration in Fig. 4.8c shows a $\Theta = 90^\circ$ oriented pullout for simplicity while most actual pullouts will be at an inclined angle.

According to the theorem of Saint Venant, the reduction of mismatch stresses is restricted to a very thin zone of only a few grain diameters in thickness. Therefore, COD measurements at the surface must yield excessive displacements that will underestimate the bridging stresses according to Eq. (3). This factor can, in part, explain the lower bridging stresses deduced from the COD method relative to the *R*-curve method (Fig. 4.3b).

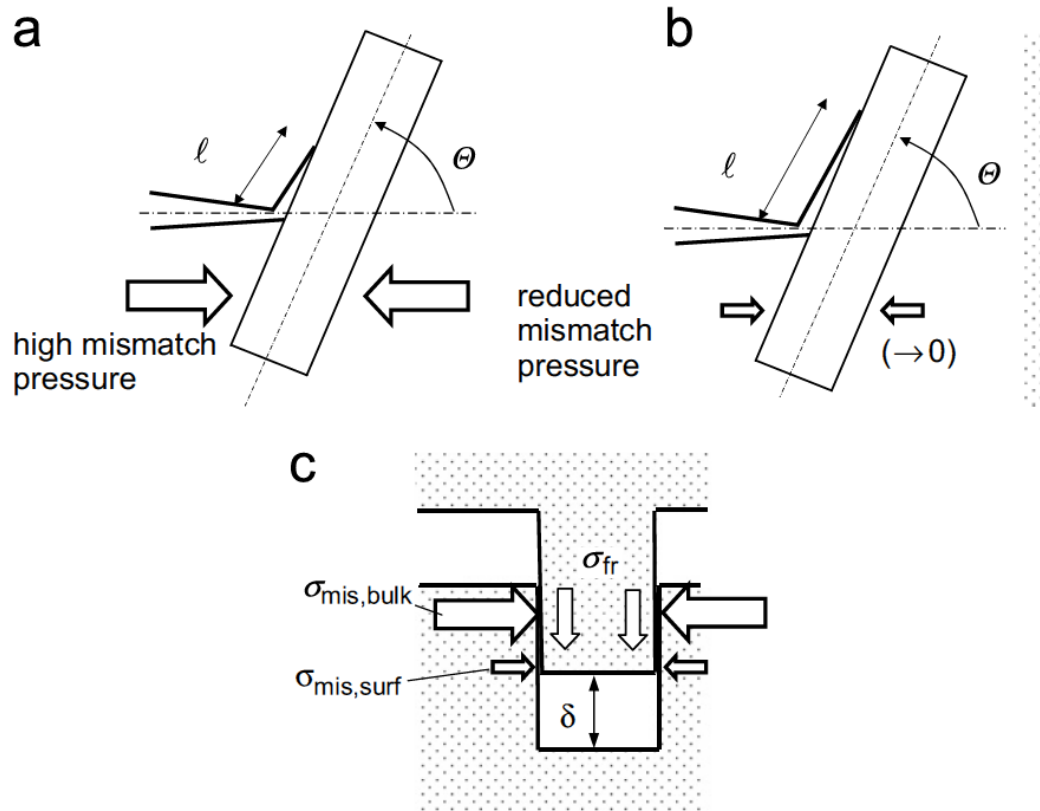


Figure 4.8 Influence of a reduced compressive stress normal to a β -crystal. Debonding lengths under the same externally applied load for a) bulk material, b) grains located near a free surface, c) crack surface interaction due to a local frictional bridging event.

4.5.2 Effect of the T -stress and sample geometry

Considering the expected influence of the free surface on bridging stresses determined from COD method, the R -curve method provides an attractive alternative since a through thickness averaged bridging stress distribution is determined. Accordingly, it is expected highly accurate results are obtained when the crack not influenced by the starter notch, as for the alumina data shown as the solid line in Fig. 4.2. However, for the special case of materials with steeply rising R -curves (e.g., Si_3N_4) the R -curve measurements must be made while the crack is still under the

influence of the starter notch stress field. In that case there can be effects of the T-stress on the determined bridging stress distribution, as described below.

If K_I denotes the mode-I stress intensity factor, the crack-parallel near-tip stresses σ_x represented by the singular and the first regular stress terms are written as

$$\sigma_x = \frac{K_{tip}}{\sqrt{2\pi r}} \cos \frac{1}{2} \varphi (1 - \sin \frac{1}{2} \varphi \sin \frac{3}{2} \varphi) + T + O(r^{1/2}) \quad (11)$$

where r is the crack-tip distance and φ the polar coordinate angle. In the wake of the crack where the bridging interactions are active $\varphi=\pi$ and only T , the crack-parallel so called “T-stress,” remains fully present. Its influence may be discussed using a simplified model.

Due to the anisotropy and non-homogeneity of a Si_3N_4 -ceramic, the computation of stress intensity factors for the kink situation in Fig. 4.8a is very complicated. The K -values are complex numbers. In order to allow a simple understanding of the trends caused by the T-stress, an approximation may be made by assuming a unique isotropic and homogeneous Young’s modulus and Poisson’s ratio.

The effect of a debond of length ℓ occurring for an angle of $\Theta < \Theta_{cr}$ is shown in Fig. 4.9a. Θ_{cr} is the critical angle that defines the debonding versus non-debonding conditions. The crack may terminate in the center of a β -grain where shear-mismatch disappears due to symmetry. Kinks into the weaker direction of the grain boundary can develop under the superimposing normal component of the thermal mismatch stress, $\sigma_{mis} < 0$, and the T-stress T resulting in a kink of length ℓ . The stress intensity factors at the tip of the kink can then be written

$$K_I(\ell) = K_I(a) \cos^3(\tfrac{1}{2}\Theta) + \sigma_{mis} \sqrt{\ell} \sqrt{\frac{8}{\pi}} + T \sqrt{\ell} \sqrt{\frac{8}{\pi}} \sin^2 \Theta \quad (12a)$$

$$K_{II}(\ell) = K_I(a) \cos^2(\tfrac{1}{2}\Theta) \sin(\tfrac{1}{2}\Theta) - T \sqrt{\ell} \sqrt{\frac{8}{\pi}} \sin \Theta \cos \Theta \quad (12b)$$

where the mode-I stress intensity factor $K_I(a)$ and the T-stress T are computed for the straight unkinked crack (i.e. for $\ell \rightarrow 0$). The energy release rate for crack extension by ℓ can be represented by an effective stress intensity factor K_{eff}

$$G = K_{eff}^2 / E', \quad E' = E / (1 - \nu^2) \quad (13a)$$

$$K_{eff} = \sqrt{K_I(\ell)^2 + K_{II}(\ell)^2} \quad (13b)$$

A kink along the interface must grow until K_{eff} equals the “fracture toughness” $K_{Ic,int}$ of the interface. The kink length ℓ can be quantified in terms of the two parameters $\sigma_{mis}/K_I(a)$ and T/σ_{mis} by solving the equation

$$\begin{aligned} \left(\frac{K_{Ic,int}}{K_I(a)} \right)^2 = & \left(\cos^3(\tfrac{1}{2}\Theta) + \frac{\sigma_{mis}}{K_I(a)} \sqrt{\ell} \sqrt{\frac{8}{\pi}} \left(1 + \frac{T}{\sigma_{mis}} \sin^2 \Theta \right) \right)^2 + \\ & + \left(\cos^2(\tfrac{1}{2}\Theta) \sin(\tfrac{1}{2}\Theta) - \frac{\sigma_{mis}}{K_I(a)} \frac{T}{\sigma_{mis}} \sqrt{\ell} \sqrt{\frac{8}{\pi}} \cos \Theta \sin \Theta \right)^2 \end{aligned} \quad (14)$$

For $\ell=0$ the critical incidence angle Θ_{cr} results from

$$\frac{K_{Ic}}{K_I(a)} = \cos^2(\tfrac{1}{2}\Theta_{cr}) \quad (15)$$

For any given incidence angle Θ the kink length ℓ can be determined as the zeros of

$$\begin{aligned}
\cos^4(\tfrac{1}{2}\Theta_{cr}) = & \left(\cos^3(\tfrac{1}{2}\Theta) + \frac{\sigma_{mis}}{K_I(a)} \sqrt{\ell} \sqrt{\frac{8}{\pi}} \left(1 + \frac{T}{\sigma_{mis}} \sin^2 \Theta \right) \right)^2 + \\
& + \left(\cos^2(\tfrac{1}{2}\Theta) \sin(\tfrac{1}{2}\Theta) - \frac{\sigma_{mis}}{K_I(a)} \frac{T}{\sigma_{mis}} \sqrt{\ell} \sqrt{\frac{8}{\pi}} \cos \Theta \sin \Theta \right)^2
\end{aligned} \tag{16}$$

For a critical incidence angle of $\Theta_{cr}=65^\circ$, the kink length as a function of the kink angle is plotted in Fig. 4.9b for the case $T=0$ by the bold line. This result was obtained from Eq. (16) with a parameter of $\sigma_{mis}/K_I(a) = -73/\sqrt{\text{m}}$ that matches the value $\ell=5.3\mu\text{m}$ at $\Theta=18^\circ$ as found by [65] for a Si_3N_4 -ceramic with similar microstructure but La doping instead of Y. The thin lines represent the effect of the T-stress. Since the mismatch stress is negative, the ratio T/σ_{mis} is positive for a negative T-stress. The linear extrapolation of the lower curve parts to $\ell \rightarrow 0$ defines effective critical kink angles indicated by the circles. With increasing T/σ_{mis} these effective critical kink angles, designated now as $\Theta_{cr,eff}$, decrease.

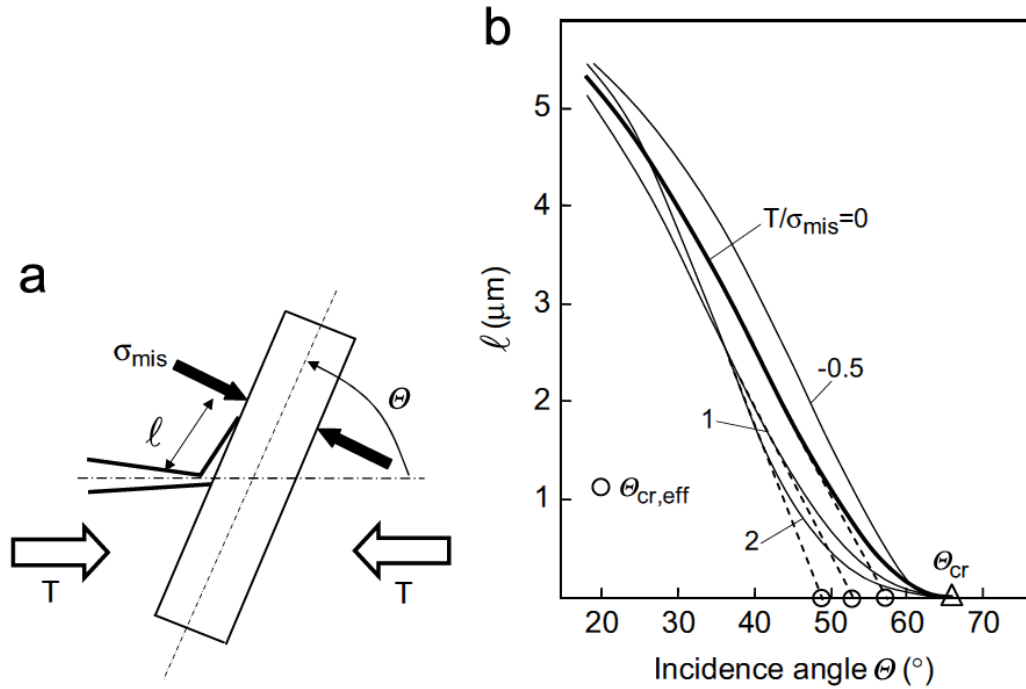


Figure 4.9 Influence of T-stress on debonding, a) crack kinking at the interface grain/grain-boundary phase, b) effect of $T \neq 0$ on debonding length.

Since $K_I(a)$ should be in the order of $5 < K_R < 7 \text{ MPa}\sqrt{\text{m}}$ [1], it results $-\sigma_{mis} \approx 350\text{--}500 \text{ MPa}$. It should be noted that rather large T-stress values are necessary for the computed shift of the curves in Fig. 4.9b. It has to be emphasized that the results obtained in this study can only give rough estimations due to the isotropic model used. T-stresses in mechanical test specimens are mostly negligible. There are only a small number of tests exhibiting strongly negative T-stresses. Most important are the double cleavage drilled compression (DCDC) specimen [116], the cone crack and, generally, notched specimens showing very small notch radii. It has been shown in [117, 118] that for slender notches in notched bending bars, as were used in [1, 59] for the R -curve determination, very strong compressive T-stresses occur. It can be concluded

that during the first few micrometers of crack extension from a notch in a bending bar, maximum negative values of

$$\frac{T}{\sigma_{bend}} = -1.052F(a_0)\sqrt{\frac{a_0}{R}} \quad (17)$$

occur, where $F(a_0)$ is the geometric function for the stress intensity factor of a crack of depth a_0 and σ_{bend} is the outer fiber bending stress.

For the R -curve experiments on silicon nitride with Y_2O_3 and MgO content [1], bending bars of $W = 4$ mm width were used with starter notches of $a_0 \approx 2.5$ mm depth having notch radii of $R = 6 - 10$ μm . The applied bending stresses were about 30-40 MPa. As can be seen from Fig. 4.10, only the first crack extensions of $\Delta a < 3$ μm are affected by the T-stress term. For these small crack extensions an effect on debonding must be expected.

From Fig. 4.10 it can be concluded that the T-stress after about $\Delta a = 1$ μm crack extension ($T/\sigma_{bend} \cong -18$) is on the order of $T \approx -650$ MPa. After 2 μm crack growth ($T/\sigma_{bend} \cong -8$), the T-stress drops to about $T \approx -280$ MPa. In terms of Fig. 4.9b, this gives a shift of the critical kink angle from 57° to 51° and 54° for $T \approx -650$ MPa and $T \approx -280$ MPa, respectively.

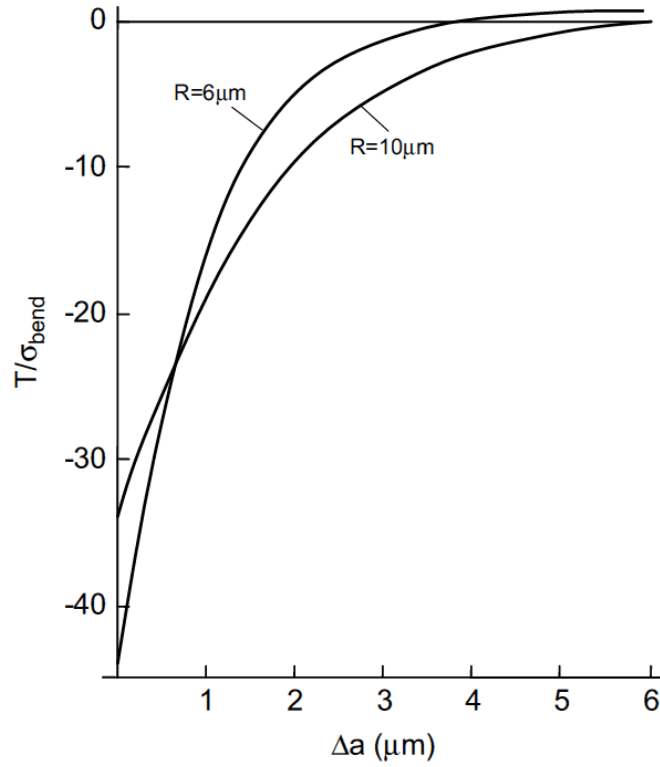


Figure 4.10 T-stress for small cracks emanating from narrow notches in a bending bar according to [117].

Since debonding generally leads to a more compliant structure, the steepness of the R -curve is increased during the very first $2 \mu\text{m}$ crack extension. The effect on the $K_R(\Delta a)$ -curves quickly becomes negligible for $\Delta a > 2 \mu\text{m}$.

Nevertheless, an effect on the bridging stresses must be expected for the special case of materials with steeply rising R -curves, such as with the present Si_3N_4 ceramic. It has been shown in [88] that the peak height of the bridging stresses in the crack-tip distance r is in a first-order approximation proportional to the steepness of the R -curve after a crack extension of $\Delta a = r$

$$\sigma_{br}|_{r=\Delta a} \propto -\frac{dK_R}{da} \quad (18)$$

resulting in maximum stresses after about 2 μm crack extension, i.e. in the region of significant T -influence. As the consequence of the T -stress, the bridging stresses obtained within the notch influenced region are generally increased relative to the $T \approx 0$ condition. In this special steeply rising R -curve case, the peak bridging stress falls in the T -stress influenced region and a higher peak stress is seen relative to the C(T) specimen in Fig. 4.3b.

As mentioned in section 4.1 the C(T) bridging stresses are further reduced in Fig. 4.3b due to the free surface effects of the COD method. Accordingly, it is expected that the $T = 0$ bridging stress distribution, which is expected to be a true material property, lies between the two curves in Fig. 4.3b.

4.5.3 *Bridging stresses from spectroscopy methods*

As expected, the bridging stress distributions for the fatigue cracks had lower peak stresses than those measured with monotonically increasing loading due the cyclic bridging degradation. This is seen by comparing Figs. 4.3 & 4.6. Also, the general shapes of the Raman measured bridging stress distributions appear reasonable and in agreement with the other methods. The measured location of the stress peak is also similar from specimen to specimen indicating a low degree of scatter in the distribution shape.

However, difficulties were encountered in measuring the magnitudes of the bridging stress profiles for silicon nitride using Raman spectroscopy. The peak bridging stresses from Raman spectroscopy demonstrate significant scatter and also a dependence on specimen color (Fig. 4.4b). The scatter tends to be more pronounced

in the darker samples (Fig. 4.4b). Furthermore, the average peak stress for the light grey colored samples was only ~36% that of the black samples (Fig. 4.6).

The increased scatter can be explained by the 50% increase of sampling depth and almost doubling of the sampling volume from the dark to light specimens (Fig. 4.7). When using a microprobe to measure bridging stresses it is important to recognize that bridges are discrete entities with variable individual bridging forces. Based on Fig. 4.7 nearly twice as many bridging grains were sampled in the light grey specimens as compared to the dark specimens. Sampling more grains per measurement allows for 1) more averaging of bridges carrying various loads and 2) more averaging of grains located between the bridges that bear zero load. With the smaller sampling volume the fluctuations in measurements will be exaggerated depending on the number of high, low, and zero load bearing grains measured. Doubling the sampling volume decreases this sampling error by averaging over more grains and better approximating the through thickness average. Thus, less scatter is observed with the light grey samples.

Additionally, the higher average peak stress measured for the dark samples (Fig. 4.6) can be rationalized by the fact that the microprobe sampling is confined to grains at or near to the surface. Here it is important to note that near surface bridges will be more compliant than subsurface bridges as described in section 4.1, thus giving a larger amount of strain at a given stress level. Furthermore, grains deeper inside the materials are confined on all sides by surrounding grains and will experience less strain at a given stress. The Raman spectroscopy technique is basically a measurement

of lattice strain which is then converted to stress by a calibration factor. Accordingly, the less constrained surface bridges will be expected to give an relatively high stress estimate based on the Raman shift. With a larger sampling volume more subsurface bridges are averaged with the surface bridges to give a value closer to the through thickness average for the light grey samples.

In contrast to the Si_3N_4 Raman results, it has been reported that the fluorescence spectroscopy method gives accurate agreement with the *R*-curve method for determining the bridging stress distribution of fatigue cracks in C(T) samples (Fig. 4.2). As mentioned above the *R*-curve method has the advantage of giving a through thickness average that is not significantly biased by the surface condition. Additionally, in [7] the *R*-curve was measured only with crack outside of the influence of the notch, so T-stress effects were negligible. The excellent agreement with the fluorescence results is explained by the fact that $\sim 2.5\%$ of the sample thickness was sampled by the fluorescence microprobe due to the translucent optical properties of Al_2O_3 . Accordingly, ample material was sampled to obtain an average distribution that roughly represents the through thickness average and agrees with the *R*-curve result. Accordingly, it is concluded that in the absence of T-stresses a bridging distribution can be determined that is a true material property. Furthermore, it can be independently measured by different techniques provided adequate through thickness sampling is utilized in the method. In the alumina case 2.5% of the thickness appears adequate.

4.5.4 Deducing the fatigue bridging stress distribution

The Si_3N_4 material used in the study represents a special class of materials where the R -curves rise very quickly over the first few micrometers of crack growth. This requires very specialized techniques to measure the fracture R -curve, $K_R(\Delta a)$, as described in [1, 60]. In fatigue it is essentially impossible to control fatigue crack propagation at these size scales, thus the direct measurement of the fatigue threshold R -curve as described in [7, 67, 119] is practically impossible. Nevertheless, understanding and predicting the fatigue failure behavior of these materials has technological importance [21, 22] and knowledge the bridging stress distribution for a fatigue crack can enable the calculation of the fatigue threshold R -curve via Eqs. (1)-(3). The fatigue threshold R -curve can then be used to predict fatigue behavior as demonstrated in [7].

In this regard, a new method for deducing a best estimate bridging stress distribution for a fatigue crack has been presented (Fig. 4.5). By using the best estimate of the distribution shape from the fracture R -curve and degrading the peak magnitude to match the measured fatigue behavior this method should be insensitive to many of the problems described above. Indeed, the problems described above focus largely on errors in the bridging stress peak magnitude, and in Fig. 4.5 the peak magnitude was independently determined from fatigue threshold experiments using Eqs. (1)-(3). Future work will focus on verifying the accuracy of fatigue predictions based on the deduced bridging distribution (Fig. 4.5) as has been done for Al_2O_3 in [7].

Alternatively one could attempt to improve the spectroscopy results by increasing the sampling volume similar to alumina; however, this is dependent on the optical properties of the material which is usually not a controllable variable. Another approach could be to increase the number of specimens sampled. Based on the results in Fig. 4.6 it may be suspected that with enough samples a reliable average might be attained; however, with such limited sampling volume some biasing of the surface stress state would always be retained making this alternative less attractive. Also, this approach would require more experimental time and material to be used. While increasing the laser power may be a way to decrease the data collection time, sample heating will occur giving unreliable Raman results. Furthermore, increasing the laser power will not increase the sampling volume as that is dependent solely on the absorption coefficient of the material. Overall, while it was instructive to use the Raman technique to verify the approximate bridging distribution shape, it does not appear to be reliable and/or time efficient as a stand-alone technique for determining the bridging stress distribution in the present Si_3N_4 where the sampling volume was severely limited to only 0.1 – 0.2% of the sample thickness. It is expected that Raman spectroscopy would be more useful when better penetration depth is achieved.

4.6 Conclusions

Based on a comparison of bridging stresses measured using *R*-curve, COD, and spectroscopy methods, the following conclusions may be made:

- The COD method is surface sensitive and gives a lower peak bridging stress compared to the *R*-curve technique which samples through the entire material

thickness. This effect is caused by reduced compressive residual stresses normal to the crystal length axis that affect the critical crack terminating angle Θ_{cr} and give increased debonding lengths ℓ . Grains acting as frictional bridges also undergo reduced friction stresses. These factors give a more compliant near surface bridging zone and lower the calculated bridging stress.

- When R -curves rise steeply over the first few micrometers of growth from a notch, an effect of negative T-stress is expected to raise the R -curve determined peak bridging stress. This effect is attributed to a reduction in the critical angle Θ_{cr} for grain debonding and the concurrent steepening of the R -curve.
- Spectroscopy methods only yield reliable bridging stress results if a reasonable through thickness volume of material is sampled. While 2.5% of the specimen thickness achieved using fluorescence spectroscopy appears adequate for Al_2O_3 , the 0.1 – 0.2% of the sample thickness achieved using Raman spectroscopy for Si_3N_4 appears inadequate.
- It is concluded that in the absence of T-stresses a bridging distribution $\sigma_{br}=f(\delta)$ can be determined that is a true material property. Furthermore, it can be independently measured by different techniques provided adequate through thickness sampling is utilized in the method. In the alumina case 2.5% of the thickness appears adequate.

- A new method has been proposed for determining the bridging stresses of fatigue cracks from 1) the bridging stress distribution for monotonically loaded cracks and 2) experimental fatigue data.

**Fatigue Endurance Strength Predictions for Silicon Nitride and
Materials Toughened by Grain Bridging Mechanisms**

R. B. Greene, S. Fünfschilling, T. Fett, M. J. Hoffmann, J. J. Kruzic

5 Fatigue Endurance Strength Predictions for Silicon Nitride and Materials Toughened by Grain Bridging Mechanisms

5.1 *Abstract*

Because of its attractive material properties like high hardness, high toughness, and excellent high temperature strength, materials like silicon nitride are becoming more common for use in high performance applications. However, there have been limited studies of the fatigue behavior of small cracks in silicon nitride and other materials toughened by grain bridging mechanisms. This study uses a fatigue threshold R-curve computed for silicon nitride doped with MgO and Y_2O_3 as sintering additives in order to develop a fatigue endurance strength prediction tool to aid in the design of products using the material. Cyclical fatigue experiments conducted on bend beams with induced semi-elliptical surface cracks were conducted to verify the prediction tool. The results show that no bend beams with this crack geometry failed below the predicted endurance level. It is expected that this method can be extended to create fatigue endurance strength predictions for other materials similarly toughened by grain bridging and other mechanisms.

5.2 *Introduction*

Extrinsically toughened materials exhibit different behaviors depending on the size of the crack length relative to a fully developed and fully toughened crack. This breaking of the law of similitude causes difficulties in predicting the endurance lifetime behavior for very small crack sizes.[11] Depending on loading, short cracks may at first grow faster than predicted by the Paris Law, but then may slow down or

arrest when the crack becomes functionally long. In materials that exhibit this behavior, such as those toughened via the crack bridging mechanism—these short cracks do not have a fully developed bridging zone. When the crack grows long enough in these materials, the bridging zone becomes fully developed—at this point, while new bridges are being formed older bridges are being destroyed through such mechanisms as frictional wear and eventually complete pull-out.[6, 30, 120] The bridging zone attains a constant length and moves along as the crack grows through the material. This is responsible for the plateau behavior of the resistance curves (R-curves) for these types of materials.[121]

The goal of this study is to develop a design tool for predicting the cyclical fatigue failure of silicon nitride ceramics. Specific to this study, predictions will be made for small semi-elliptical surface cracks in silicon nitride (Si_3N_4) bend-beams doped with the rare-earth oxide, Y_2O_3 and MgO (denoted as Mg-Y). This material forms elongated β -phase hexagonal grains with a mean diameter of $0.28\text{ }\mu\text{m}$ and an aspect ratio of ~ 7 and has a glassy weak intergranular film.[29] Figure 5.1 shows a micrograph of this silicon nitride. The weak film encourages intergranular fracture leaving intact the elongated grains to form bridges spanning the wake of the crack that are able to carry load reducing the stress felt at the crack tip, K_{tip} .[23] In silicon nitride these zone are quite short—on the order of $100\text{ }\mu\text{m}$, this makes studying the behavior of short cracks quite difficult and requiring non-conventional methods.

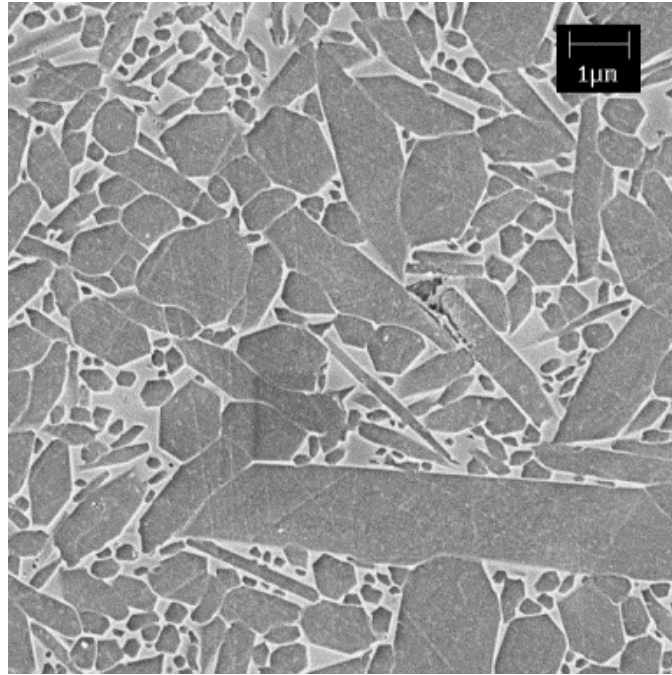


Figure 5.1 Scanning electron micrograph of silicon nitride doped with Mg-Y

Interest in silicon nitride for applications in the manufacturing industry is growing because of its great material properties. Silicon nitride has excellent hardness, toughness, and strength especially at elevated temperatures making them attractive materials for cutting and rolling tools. One recent example is the application of rolling of high strength alloy wires from steels and nickel-based super-alloys where cemented carbide rolls suffer wear and thermal fatigue cracking, leading to a degradation of wire quality.[21] Furthermore, it has been shown that under moderate loading silicon nitride rolls can give >10 times longer life and improved wire surface quality.[21] However, it has also been shown that the rolls can suffer fatigue failure at higher loadings, for example when rolling wires with high deformation resistance such as the super alloy wire Nicrofer S7020.[21, 22]

Predictions were formed based off the resistance curve developed for cyclical fatigue in Mg-Y doped silicon nitride (Fig. 5.2).[25] The prediction tool formed (Fig. 5.3) simply delineates a safe directive for allowable loads based on half of the initial surface flaw size. Loading below this line is considered safe for cyclic loading, loading above the line will likely guarantee eventual failure. Included on the plot is a dashed line denoting how a material not toughened by bridging would behave. The gap between the two lines represents the added loading potential that the toughened material has over the non-toughened material.

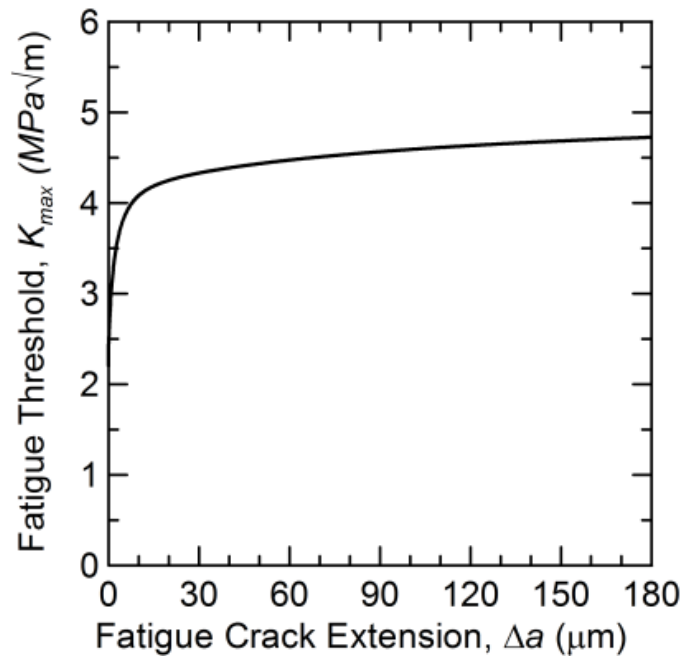


Figure 5.2 Fatigue Threshold R-curve for semi-elliptical surface cracks in silicon nitride bend beams.

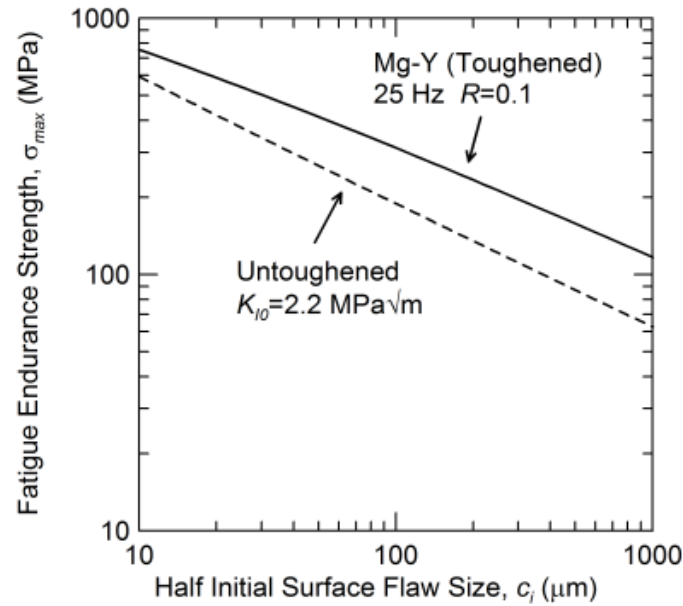


Figure 5.3 Fatigue endurance strength based on the half-initial surface flaw size, the dashed line represents a material that is not toughened by bridging, and the solid line represents the worst case cyclical fatigue loading for the Si_3N_4 Mg-Y doped toughened material assuming an a/c ratio of 1.

There is little previous study into lifetimes for silicon nitrides subjected to cyclical fatigue loading at room temperature. Ogasawara, et al. studied the probability of silicon nitride specimens failing after a certain number of cycles at maximum loads below the bending strength. However, this study ignored flaws in the material and any associated effects of crack sizes.[122] It is important to consider these issues when designing with materials such as silicon nitride. Another study by Choi et al. studied the maximum applied stress vs. lifetime of fatigue crack growth rates in silicon nitride. However, no attention was paid to the influence of initial flaw size on allowable fatigue endurance strengths.[123]

A previous study by Gallops, et al. on alumina assumed that the dimensions of the induced semi-elliptical crack would be suitably constant from sample to sample.[7]

Figure 5.4 shows a schematic of a bend beam with a semi-elliptical surface crack. Depth of the crack into the sample, a , and half-initial surface crack size, c , denote the dimensions of the crack. Assumptions were that the crack size ratio, a/c , would be about 0.5 however after examination of post-cracked specimens in the current study, it was determined that this ratio varied and was not predictable. Exact crack depth was sought to be eliminated as a factor since it cannot be measured unless the sample has failed. To make the prediction tool solely reliant on surface crack size, it was necessary to develop a range of worst and best case loading limits based on the extremes of the crack size ratio.

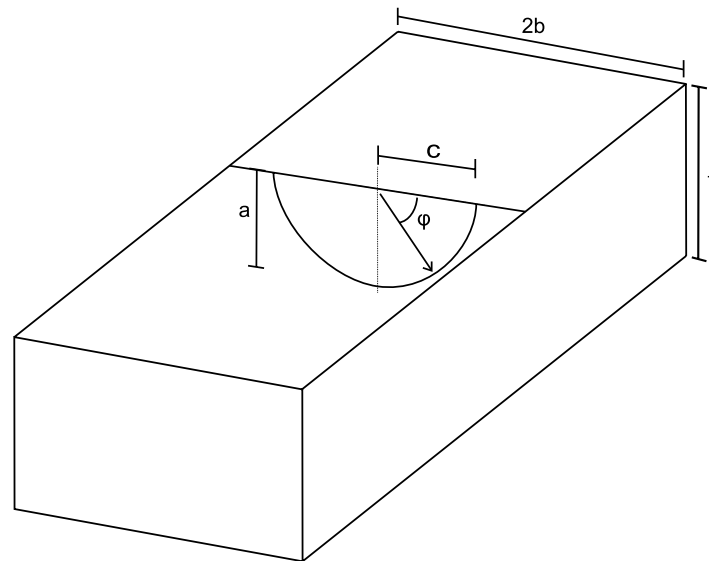


Figure 5.4 Depiction of dimensions of a bend beam with schematic of a semi-elliptical surface crack.

5.3 *Procedure*

5.3.1 *Material*

Endurance tests were conducted on a hot-isostatically pressed silicon nitride with 5 wt% Y_2O_3 and 2 wt% MgO as sintering aids. Full details on the processing of the silicon nitride may be found elsewhere [57], but briefly, powders were prepared by attrition milling in isopropanol and the slurries were subsequently dried and the powders sieved. Green bodies were uniaxially pressed and then subsequently cold-isostatically pressed with 400 MPa. The samples were sintered in a hot-isostatic-press (HIP) with a two-step sinter-HIP process, where closed porosity is obtained at low N_2 pressures during the first sintering step and full density was achieved during the subsequent HIP step at a maximum nitrogen pressure of 10 - 20 MPa. Full density (water immersion method) is defined here for relative densities greater than 99% of theoretical density, which was calculated by the rule of mixture based on the starting compounds.

5.3.2 *Sample Preparation*

Bend beam samples were cut from the bulk material with a nominal size of 3 mm x 4 mm x 50 mm. Samples were lapped parallel using a 600-grit silicon carbide slurry. One side was then lapped further with a 1000-grit slurry, then polished with a 3 μm and 1 μm diamond suspension.

In order to initiate pre-cracks in the samples they were indented in general accordance with ASTM Standard 1421 using a Knoop indenter.[124] Loads ranging

from 40 N with a dwell time of 60 seconds to 280 N with a dwell time of 30 seconds were selected to achieve a wide range of initial surface crack sizes, $2c$, from $\sim 100\ \mu\text{m}$ to $\sim 700\ \mu\text{m}$.

Indentation length, d , was measured using an optical microscope. The sides of the samples with the indents were then lapped and polished as before to remove the indentation and the accompanying residual stresses.[125] The optimal thickness of material removed was about 5 times the depth of the Knoop indent, h , in which $h = d/30$.

5.3.3 Crack Measurement

To suitably measure the pre-crack, the sample was treated with a fluorescing dye (Zyglo ZL-27A, Magnaflux, Glenview, IL) for at least 30 minutes to allow for full penetration. Excess dye was removed with acetone and the sample then treated with developer (Zyglo ZP-9F, Magnaflux) for at least 30 minutes. An optical fluorescence microscope was used to observe the cracks and measure their lengths.

5.3.4 Endurance Prediction Curve

To determine the fatigue endurance strength prediction curve the fatigue threshold R-curve needs to be computed. It is necessary to use the bridging stress distribution[7, 25, 88] for fatigue threshold to construct an R-curve for the proper geometry. Attempts at directly measuring the bridging stress distribution for silicon nitride using micro-Raman spectroscopy were inconclusive, so it was determined that it would be sufficient to use the maximum stress intensity at threshold, $K_{th,max}$,

measured for silicon nitride in cyclical fatigue crack growth experiments to scale down the static fracture R-curve determined by Fünfschilling.[1] Details of this study can be found in Greene, et al. 2012.[25]

Computing the endurance prediction curve follows that both equations 1 and 2 be satisfied. The applied stress intensity curve, $K_{max,app}$, must be equal and tangent to the fatigue threshold R-curve, $K_{max,TH}$, at each value of crack extension, Δa . $\sigma_{max,app}$ represents the critical externally applied stress corresponding to $K_{max,app}$. Loading above these conditions will result in unrestricted crack growth, loading below these conditions will result in a crack that grows a small amount then arrests.[121]

$$K_{max}^{app} = Y\sigma_{max}^{app}\sqrt{\pi a} = K_{max}^{TH}(\Delta a) \quad (1)$$

$$\left. \frac{dK_{max}}{da} \right|_{app} = \frac{dK_{max}^{TH}(\Delta a)}{da} \quad (2)$$

Y in Eqn. 1 represents the shape factor for a semi-elliptical crack, Q , in a bend beam and the stress-intensity boundary-correction factor, F , which depends on a/t , a/c , c/b and ϕ . [126] Referring to Figure 5.4, ϕ , denotes the angle from the surface where the shape factor equations analyze the stress intensity for the crack front; t and b are beam thickness and half-width respectively.

$$Y = \frac{H}{\sqrt{Q}} F\left(\frac{a}{t}, \frac{a}{c}, \frac{c}{b}, \phi\right) \quad (3)$$

Figure 5.5 depicts a simplified schematic of the process for creating the prediction curve. Crack extension, Δa , is varied so that stress, s , and initial crack length, a_i , can be solved for numerically.

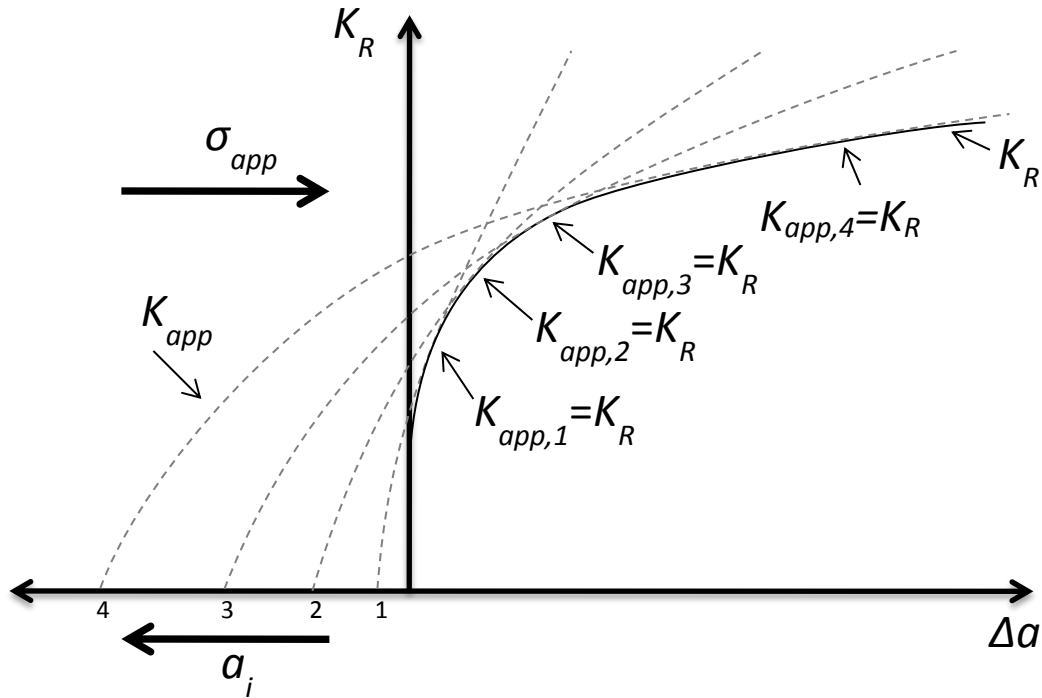


Figure 5.5 Schematic of the process of solving the system of equations 1 and 2 for the prediction curve

Because it was determined that it was not possible to exactly predict the crack ratio, a/c , a range of loading scenarios was formulated to account for this. Measurable a/c ratios ranged from 0.5 to almost 0.8. Figure 5.6 depicts a graph of the analysis done to determine the best and worst case scenarios. Different values of φ were chosen and equation 3 was used varying a/c from 0.2 to 1. Values of t and b chosen matched those of the dimensions of the bend beams used in this experiment. Best and worst case fatigue failure prediction curves were constructed based on the analysis that

at an a/c ratio of 1, crack driving forces are at a maximum at the surface ($\varphi = 0$) (worst case), and at an a/c ratio of 0.802 crack driving forces are at a minimum (best case).

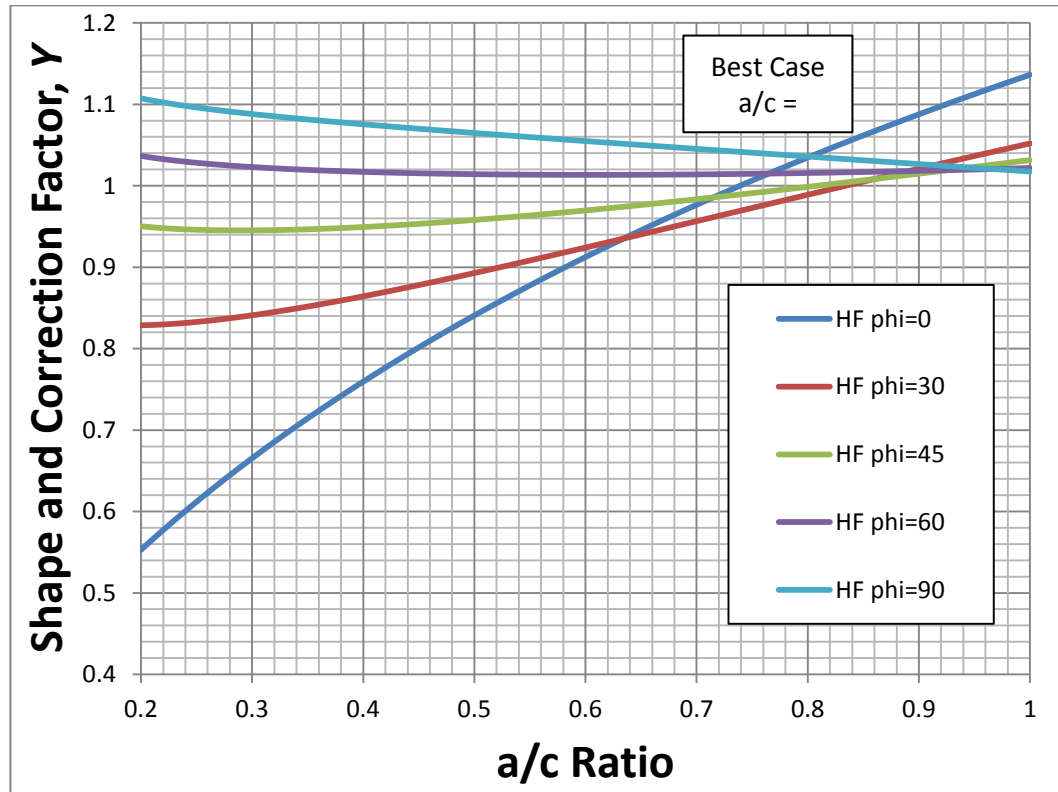


Figure 5.6 Chart depicting maximum and minimum shape and correction factors for the stress intensity in a semi-elliptical surface crack in a bend beam.

5.3.5 Loading Determination

Loading levels, σ_{max} , based on initial half-crack size were determined from the predicted endurance graph data. Two loading levels to ensure fatigue failure conditions were selected at loads 1/3 and 2/3 the difference between the worst-case static fracture[1] and the best-case fatigue endurance curves. One loading level to ensure endurance conditions was selected at loads 2/3 the difference between the worst-case scenario fatigue endurance curve and the curve representing an

non-toughened material. In certain cases, exact adherence to the loading levels was not possible. Such cases are when the load limits of the testing equipment were approached for very short crack lengths.

5.3.6 *Cyclical Fatigue Experiments*

Bend beams were cyclically loaded in four-point bending on a Bose ElectroForce 3200 dynamic test frame (Bose Corporation, Eden Prairie, MN). A support span of 40 mm and a loading span of 12.4 mm were used. A load ratio, $R = \sigma_{min}/\sigma_{max} = L_{min}/L_{max}$, of 0.1 was used for each and cyclically loaded at a frequency of 20 Hz using a sine wave form. Samples are assumed to pass endurance test conditions if they exhibit no failure after 10^7 cycles. One sample that was expected to fail but didn't was cycled longer until failure.

5.3.7 *Examination of crack shape post-failure*

Scanning electron and optical microscopes were used to attempt to visualize the cracks in the specimens post-failure. Because of the difficulty in imaging cracks in brittle materials, some equipment gave better results than others for different specimens.

A Quanta 600F scanning electron microscope (FEI Corp., Hillsboro, OR) was the primary imaging device used. A variety of techniques to visualize the surfaces were attempted. Chiefly, the microscope was operated under high vacuum with an accelerating voltage of 10 kV and a spot size of ~ 7 . Working distances ranged from 10 mm to 30 mm and the sample stage was tilted through a variety of angles to try to

make topical features more apparent. Both secondary and backscatter detectors were used. Samples for use in the SEM were prepared by trimming down excess in a high-speed diamond saw, cleaned in acetone in an ultrasonic cleaner, and mounted. Because they are non-conductive, they were coated for ~30 s in a sputter coater using a gold-palladium target. Some samples were also prepared for low-vacuum observations to avoid sputter-coating the samples so as not to obscure the fine details of the fracture surface. Operating conditions remained the same.

Imaging was also attempted optically, a Leica DMRM microscope (Leica Microsystems, Wetzlar, Germany) equipped with a digital capture device (Micropublisher 3.3 RTV, QImaging, Surrey, BC). This microscope has a reflective light source, but for added contrast, samples were lit from the side at a low angle. As an added benefit, if the originating semi-elliptical crack was out of plane from the bulk of the material, it could be brought into focus to more easily differentiate it. Dimensional measurements were conducted in software by built-in calibrations.

Lastly a stereomicroscope (Olympus, Tokyo, Japan) was used for optical imaging. A DinoEye USB eyepiece camera (Dino-Lite Europe, The Netherlands) was used for digital imaging. The microscope was calibrated using a micrometer slide in the JImage computer image processing software. Samples were side-lit using an incandescent bulb. Images later were processed by adjusting color levels to bring out contrast and using a desaturation filter to render into gray-scale. Dimensions were measured in JImage.

5.4 Results

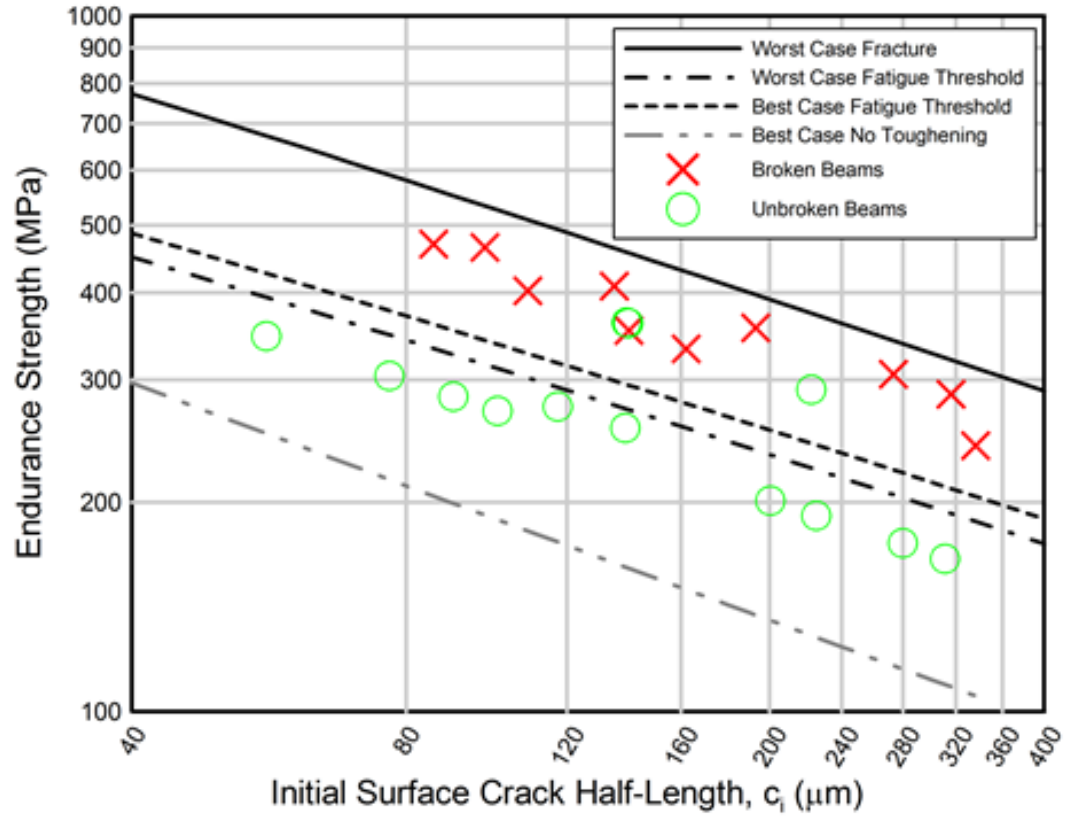


Figure 5.7 Plot showing the results of the four-point bending experiments to verify the developed fatigue strength endurance prediction tool for semi-elliptical surface cracks in silicon nitride bend beams. The failure below the best-case fatigue threshold line is due to a v-shaped crack.

5.4.1 Verifications

Figure 5.7 depicts the predicted fatigue endurance strengths vs. the half-initial surface crack lengths calculated for the various allowable a/c ratios. The solid curve at the top of the graph was calculated using the static fracture R-curve. Loading was kept below this line to ensure failure would not occur upon initial loading of the specimens. Two different loading levels were chosen in the fatigue failure zone, $1/3$ and $2/3$ the difference between fracture and the safe fatigue loading curves. The dashed and dashed-dotted lines in the center of the graph represent the uncertainty range due to unknown crack size ratio, a/c . Loading above this range was prescribed to encourage failure in the specimens as it should exceed the critical stress intensity levels for all values of a/c for semi-elliptical surface cracks. Loading below this range should ensure no failure in the specimens for the lifetime of 10^7 cycles. Loading above the curve for the non-toughened material ensures that the tests account for the rising R-curve behavior and accordingly increased toughness of the material due to development of the full grain-bridging zone.

Also depicted in Figure 5.7 are the results of the four-point bending fatigue experiments to verify the prediction tool. The circles represent beams that did not fail and the Xs represent failed beams. Above the safe-loading range, 77% of the samples tested failed. Three of the specimens loaded at the $1/3$ failure loading level experience no failure after 10^7 cycles. One of these specimens ($c_i = 140 \mu\text{m}$, $\sigma_{max} = 360 \text{ MPa}$) was cycled for $\sim 4 \cdot 10^6$ more cycles until failure occurred. Other specimens experienced failure after a large range of cycles. Those loaded at the $2/3$ loading level

generally failed quicker than those at the 1/3 loading level, anywhere from $\sim 50 \times 10^3$ cycles to $\sim 4 \times 10^6$ cycles. The lower loading level ranged from $\sim 2 \times 10^6$ to running out the experiment to the full 10^7 cycles. There is a pass rate of 100% for specimens loaded below the predicted safe loading level for fatigue.

This tool was developed solely for the geometry of a semi-elliptical surface crack in a bend beam. Upon post-failure inspection, there was a beam that did fail below this level. This beam was found to have a v-shaped surface crack which does not conform to the prediction criteria of a semi-elliptical crack.

5.4.2 *Crack Shape Analysis*

Imaging of bend beams post-experiment was conducted to gain an understanding of the actual a/c ratios that were being achieved with the Knoop surface indentations and subsequent lapping and polishing procedures. Previous experiments had assumed that ratios of 0.5 could be expected, but upon further inspection these ranged quite a bit. Fracture surfaces that could be imaged properly had ratios ranging from ~ 0.5 to ~ 0.8 . This revelation was what made necessary forming the fatigue threshold loading range to account for the uncertainty.

Figure 5.8 depicts a micrograph of a fracture surface from an SEM using a secondary electron detector. This sample had been sputter coated with gold-palladium and imaged under high vacuum. Tilting this specimen for better imaging was not necessary as the initial crack shape was readily apparent. Measuring this crack using the SEM software revealed that it had an a/c ratio of 0.51.

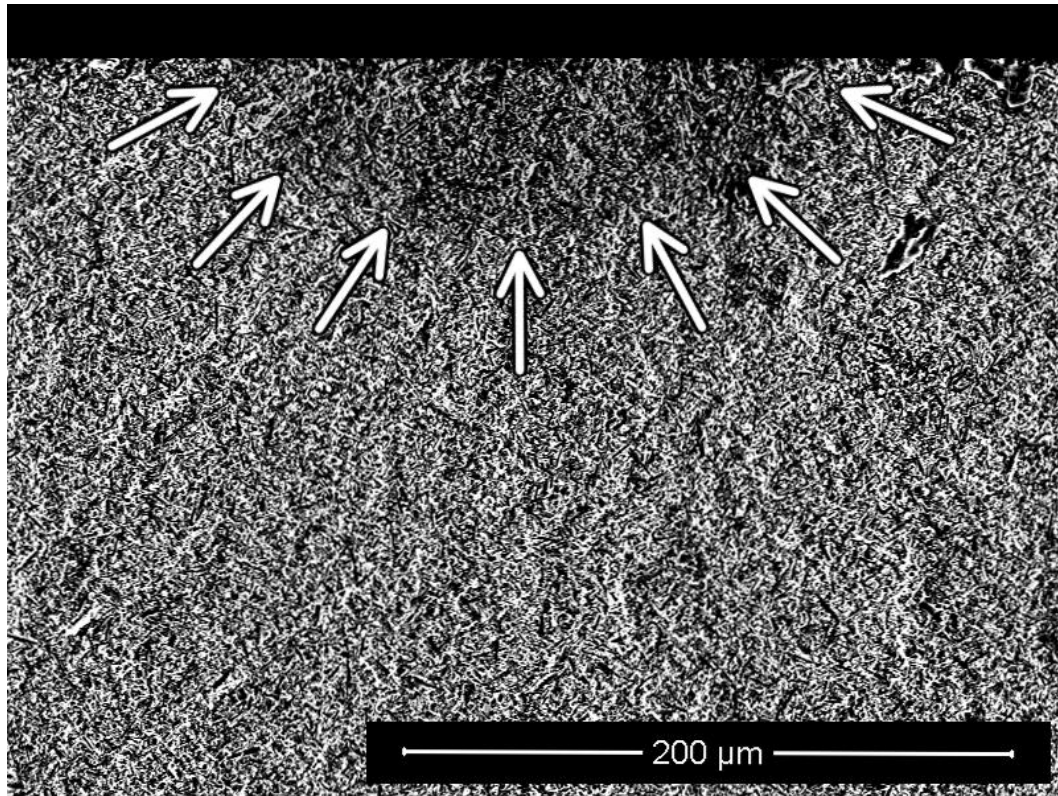


Figure 5.8 Secondary electron micrograph of a post-experiment fracture surface with the initial semi-elliptical surface crack having an a/c ratio of 0.51.

Figure 5.9 depicts an image of the fracture surface taken using an optical microscope. This specimen was loaded below the fatigue threshold endurance curve and completely ran out the experiment to 10^7 cycles. The specimen was statically fractured afterwards. Images taken with this microscope were calibrated using a micrometer slide. The calibration was taken using JImage and dimensional measurements were then able to be performed. This specimen has an a/c ratio of 0.78. The image was desaturated to remove color then contrast levels were altered in order to make the crack shape more apparent.

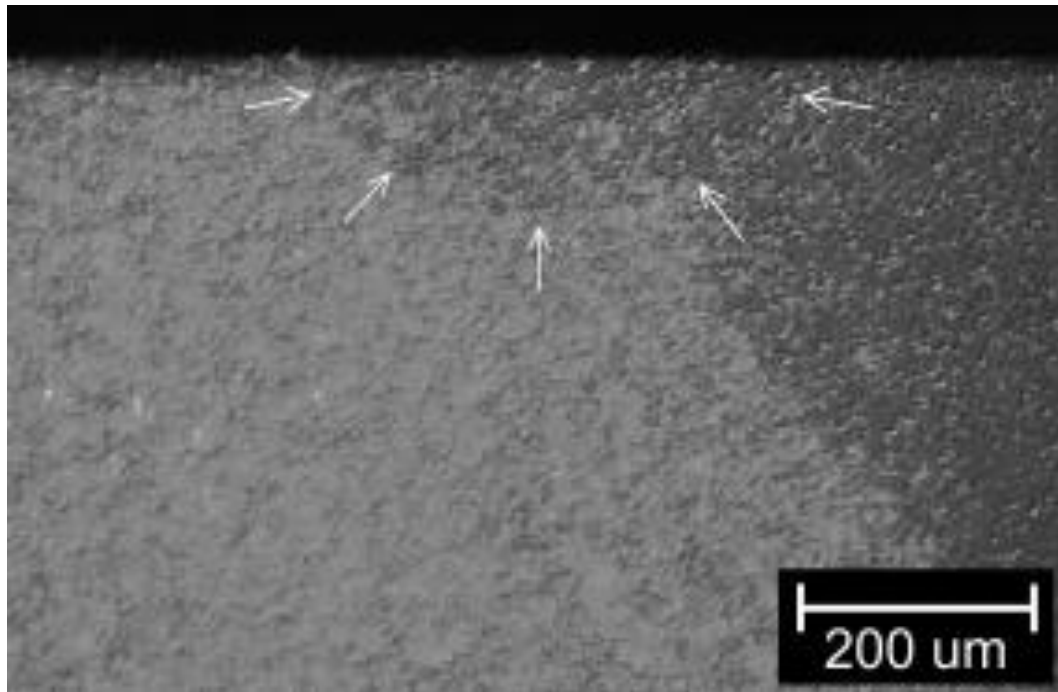


Figure 5.9 Optical image of a fracture surface from a specimen that did not fail during the experiment using the Olympus stereomicroscope with the DinoEye capture device, the specimen was statically fractured post-experiment.

Figure 5.10 depicts the fracture surface of the specimen that was loaded below the fatigue endurance level but failed. Imaging was done using the Leica microscope with the sample externally lit at a low angle of incidence to the fracture surface plane. The initial crack was slightly out of plane of the rest of the fracture surface allowing the crack to be kept in focus while the fracture surface was slightly out of focus. Upon inspection it was realized that the crack shape had a different geometry than that of what was predicted. The v-shaped flaw will experience higher stress concentrations at its depth that will accelerate crack growth compared to the smoother geometry of the semi-elliptical crack shape.

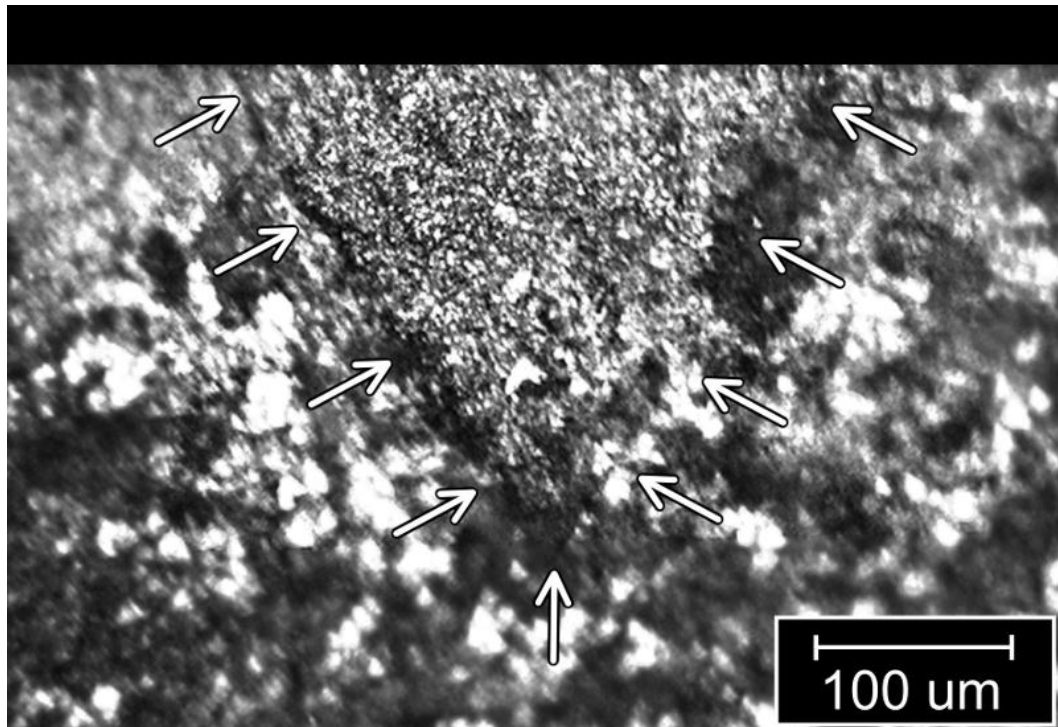


Figure 5.10 Optical image taken using the Leica microscope of the fracture surface of the specimen that was loaded below the endurance curve. This specimen failed due to the v-shaped surface crack.

5.5 Discussion

The verification of the fatigue strength endurance prediction tool developed in this study appears to be quite good. No specimens with semi-elliptical surface cracks that were tested below the fatigue threshold endurance level range failed. A high number of specimens loaded above the range (77%) did experience failure before 10^7 cycles. To see whether there was discrepancy in the prediction, one of these beams was cycled longer under the same loading conditions and failure did occur after an addition 4×10^6 cycles. This may signify that the lifetime condition of 10^7 cycles may actually be longer near the fatigue threshold.

From the above results this prediction tool would be suitable for design of components made from silicon nitride as long as proper geometry and crack shapes were assumed. The specimen that broke because it had a sharp v-shaped surface crack in it is a good example of why this is important. The v-shaped crack will experience higher stress intensities and thus faster crack growth for a given loading situation. Other geometries can affect the outcomes differently as well. The benefit of the way this prediction tool is designed, however, is that the R-curves for any crack shape and specimen geometry can be developed with relative ease and then be used to form a geometry specific endurance prediction tool.

When considering design based on material strengths it is common practice to incorporate a safety factor. For use in design, it is only necessary to compute the worst case fatigue threshold loading level ($a/c = 1$, $\phi = 0$). This would most likely mean that incorporating a safety factor based on that loading level would accommodate unforeseen issues with crack shape from specimen to specimen with this tool.

There is most likely uncertainty arising in this design tool from the fact that the fatigue threshold R-curve used for this study is actually computed from the R-curve for static fracture in the silicon nitride material and using the fatigue threshold stress intensity, K_{TH} , to do so. The K_{TH} calculated in a previous study by the author had scatter of about 0.22 MPa \sqrt{m} which would cause a fluctuation in the predictions. Fatigue threshold R-curves determined in other ways, such as direct fatigue threshold

experiments or using a measured bridging stress profile, also have the potential for uncertainty.[7] Again, incorporating a safety factor would accommodate possible uncertainty.

Other issues at hand with this tool are that it only accounts for the behavior of silicon nitride at normal laboratory conditions such as room temperature and moderate humidity. Silicon nitride and other materials can be sensitive to different environmental conditions like exposure to higher levels of humidity and direct exposure to water.[13, 31, 127] This exposure can give accelerated crack growth over what may be otherwise expected. Other materials may experience different additional toughening mechanisms, such as crack tip blunting, crack closure effects;[7] however, as long as an R-curve can be developed for that material a fatigue threshold endurance prediction can be constructed for it.

5.6 Conclusion

This study was conducted to explore the use of the fatigue threshold R-curve for silicon nitride for the creation of a fatigue threshold endurance prediction tool (Fig. 5.7). Based on initial flaw size in a material an appropriate maximum allowable stress for loading under cyclic fatigue conditions can be ascertained. These predictions were verified through four-point bending fatigue experiments conducted for loading conditions below and above the fatigue threshold endurance curve. All specimens adhering to the proper crack shape geometry loaded below the curve experienced no failure and 77% of the specimens loaded above the curve failed as

predicted before the lifetime expectancy of 10^7 cycles. One specimen was cycled longer at the same failure conditions and it eventually failed. It is suggested that proper safety margins be incorporated to account for uncertainty.

The method of creating this prediction tool developed here can be used as a tool for designing products that incorporate this and other materials toughened by grain bridging. In general, as long as a fatigue threshold R-curve can be measured for a material this method will apply.

6 Summary

The goal of this study was to develop fatigue strength endurance predictions for silicon nitride doped with MgO and Y_2O_3 as sintering additives. This brittle ceramic material is toughened via the grain bridging mechanism and behaves differently based on the size of the flaw relative to the size of the bridging zone.

Fatigue behavior was studied in Part I of this study to improve the understanding of the microstructure relates to the properties of the material under cyclical loading. Degradation of bridges is responsible for the decrease resistance to crack propagation under fatigue conditions. Crack growth is most dependent on the maximum stress intensity, K_{max} . Also this study allowed for the determination of the fatigue threshold, $K_{max,th}$.

In Part II of this study it was found that determination of the bridging stress profile for silicon nitride is a difficult process. Micro-Raman results proved inconclusive because they are extremely sensitive to specimen color and limited sampling volume through the material. Determining the actual profile would take many more specimens and measurements than is practical. It was then determined that a suitable approach was using the bridging stress profile determined from static fracture experiments and reducing it in such a manner that set the plateau value of the fatigue threshold R-curve, $K_{max,th}$, to that determined in Part I of this study.

Part III of this study involved using the developed fatigue threshold R-curve to construct a tool for the prediction of fatigue endurance strengths based on initial

surface-flaw size. Bend beam specimens with varied sizes of induced surface flaws were cyclically fatigued in four-point bending based on the loading suggestions of the developed endurance tool. None of the specimens cycled below the loading conditions suggested for safe fatigue operation experience failure before the stated lifetime of 10^7 cycles.

In summary, the work completed here to study the behavior of silicon nitride in fatigue show very promising results. It was determined that using bridging stress profiles to determine a geometry specific fatigue threshold R-curve was an appropriate method to develop a fatigue endurance prediction tool. This method can be extended to other geometries and materials that experience this type of toughening behavior and will thus allow for better design and safety considerations when considering those materials for development.

7 References

1. Fünfschilling, S., et al., *R Curves from Compliance and Optical Crack-Length Measurements*. Journal of the American Ceramic Society, 2010. **93**(9): p. 2814-2821.
2. Fünfschilling, S., et al., *Crack- tip toughness from Vickers crack-tip opening displacements for materials with strongly rising R- curves*. Journal of the American Ceramic Society, 2011. **94**(6): p. 1884-1892.
3. Wachtman, J.B., *Mechanical properties of ceramics*1996, New York: Wiley. xxii, 448 p.
4. Accuratus. *Materials – Silicon Nitride (Si₃N₄) Properties*. 2002 [cited 2012 May]; Available from: <http://accuratus.com/silinit.html>.
5. *Silicon Nitride (Si₃N₄) – An Overview*. 2001 [cited 2012 May]; Available from: <http://www.azom.com/article.aspx?ArticleID=53>.
6. Fünfschilling, S., et al., *Mechanisms of toughening in silicon nitrides: The roles of crack bridging and microstructure*. Acta Materialia, 2011. **59**(10): p. 3978-3989.
7. Gallops, S., et al., *Fatigue threshold R-curves predict small crack fatigue behavior of bridging toughened materials*. Acta Materialia, 2011. **59**(20): p. 7654-7661.
8. Kruzic, J.J., et al., *Fatigue threshold R-curves for predicting reliability of ceramics under cyclic loading*. Acta Materialia, 2005. **53**(9): p. 2595-2605.
9. Kruzic, J.J., R.M. Cannon, and R.O. Ritchie, *Crack-Size Effects on Cyclic and Monotonic Crack Growth in Polycrystalline Alumina: Quantification of the Role of Grain Bridging*. Journal of the American Ceramic Society, 2004. **87**(1): p. 93-103.
10. Kruzic, J.J., et al., *The Utility of R-Curves for Understanding Fracture Toughness-Strength Relations in Bridging Ceramics*. Journal of the American Ceramic Society, 2008. **91**(6): p. 1986-1994.
11. Jones, R., L. Molent, and S. Pitt, *Similitude and the Paris crack growth law*. International Journal of Fatigue, 2008. **30**(10–11): p. 1873-1880.
12. Satet, R.L., M.J. Hoffmann, and R.M. Cannon, *Experimental evidence of the impact of rare-earth elements on particle growth and mechanical behaviour of silicon nitride*. Materials Science & Engineering: A, 2006. **422**(1/2): p. 66-76.
13. De Arellano-López, A.R., et al., *Microstructure and room-temperature mechanical properties of Si₃N₄ with various α/β phase ratios*. Journal of Materials Science, 1998. **33**(24): p. 5803-5810.
14. Riedel, R., *Handbook of ceramic hard materials*2000, Weinheim ; New York: Wiley-VCH.
15. Milek, J.T., *Silicon nitride for microelectronic applications*. Handbook of electronic materials, v 3, 61971, New York,: IFI/Plenum.

16. Schwier, G., G. Nietfeld, and G. Franz, *Production and Characterization of Silicon Nitride Powders*, 1998.
17. Yanagida, H., K. Kōmoto, and M. Miyayama, *The chemistry of ceramics* 1996, Chichester ; New York: Wiley. xii, 263 p.
18. Wilcox, W.R., *Growth mechanisms and silicon nitride*. Preparation and properties of solid state materials 1982, New York: M. Dekker. vii, 224 p.
19. Whitney, E.D., *Ceramic cutting tools : materials, development, and performance*. Materials science and process technology series 1994, Park Ridge, N.J.: Noyes Publications. xxvi, 357 p.
20. Richerson, D.W. and P.M. Stephan, *Evolution of Applications of Si₃N₄-Based Materials*, 1998.
21. Danzer, R. and M. Lengauer, *Silicon nitride materials for hot working of high strength metal wires*. Engineering Failure Analysis, 2010. **17**(3): p. 596-606.
22. Harrer, W., et al., *Failure analysis of silicon nitride rings for hot rolling of highly alloyed steel and superalloy wires*. Engineering Failure Analysis, 2011. **18**(1): p. 138-147.
23. Lawn, B.R., *Fracture of brittle solids*. 2nd ed. Cambridge solid state science series 1993, Cambridge ; New York: Cambridge University Press. xix, 378 p.
24. Ritchie, R.O., *Mechanisms of fatigue-crack propagation in ductile and brittle solids*. International Journal of Fracture, 1999. **100**(1): p. 55-83.
25. Greene, R.B., et al., *A direct comparison of non-destructive techniques for determining bridging stress distributions*. Journal of the Mechanics and Physics of Solids, 2012. **60**(8): p. 1462-1477.
26. Fünfschilling, S., et al., *Bridging stresses from R-curves of silicon nitrides*. Journal of Materials Science, 2009. **44**(14): p. 3900-3904.
27. Fett, T. and D. Munz, *Stress intensity factors and weight functions*. International series on advances in fracture, 1997, Southampton, UK ; Boston, Mass. USA: Computational Mechanics Publications. 385 p.
28. International, A., *ASTM E647-08 - Standard Test Method for Measurement of Fatigue Crack Growth Rates, in Annual Book of ASTM Standards, Vol. 03.01*, 2010, ASTM International: West Conshohocken, Pennsylvania, USA.
29. Kruzic, J.J., et al., *Fatigue threshold R-curves for predicting reliability of ceramics under cyclic loading*. Acta Materialia, 2005. **53**(9): p. 2595-2605.
30. Gilbert, C.J., R.H. Dauskardt, and R.O. Ritchie, *Behavior of Cyclic Fatigue Cracks in Monolithic Silicon Nitride*. Journal of the American Ceramic Society, 1995. **78**(9): p. 2291-2300.
31. Okazaki, M., A. McEvily, and T. Tanaka, *On the mechanism of fatigue crack growth in silicon nitride*. Metallurgical and Materials Transactions A, 1991. **22**(6): p. 1425-1434.
32. Ferraro, J.R., K. Nakamoto, and C.W. Brown, *Introductory Raman spectroscopy*. 2nd ed 2003, Amsterdam ; Boston: Academic Press. xiii, 434 p.
33. Sergo, V., et al., *Stress Dependence of the Raman Spectrum of β -Silicon Nitride*. Journal of the American Ceramic Society, 1996. **79**(3): p. 781-784.

34. Pezzotti, G., et al., *In situ measurement of bridging stresses in toughened silicon nitride using Raman microprobe spectroscopy*. Journal of the American Ceramic Society, 1999. **82**(5): p. 1249-1256.
35. Becher, P.F., *Microstructural design of toughened ceramics*. Journal of the American Ceramic Society, 1991. **74**(2): p. 255-269.
36. Evans, A.G., *High toughness ceramics*. Materials Science & Engineering, 1988. **A105/106**: p. 65-75.
37. Lange, F.F., *Relation between strength, fracture energy, and microstructure of hot-pressed Si_3N_4* . Journal of the American Ceramic Society, 1974. **56**(10): p. 518-522.
38. Himsolt, G., et al., *Mechanical properties of hot-pressed silicon nitride with different grain structures*. Journal of the American Ceramic Society, 1979. **62**(1-2): p. 29-32.
39. Swanson, P.L., et al., *Crack-interface grain bridging as a fracture resistance mechanism in ceramics: I, Experimental study on alumina*. Journal of the American Ceramic Society, 1987. **70**(4): p. 279-289.
40. Mai, Y.-W. and B.R. Lawn, *Crack-interface grain bridging as a fracture resistance mechanism in ceramics: II, Theoretical fracture mechanics model*. Journal of the American Ceramic Society, 1987. **70**(4): p. 289-294.
41. Padture, N.P., *In situ-toughened silicon carbide*. Journal of the American Ceramic Society, 1994. **77**(2): p. 519-523.
42. Padture, N.P. and B.R. Lawn, *Toughness properties of a silicon carbide with an in situ induced heterogeneous microstructure*. Journal of the American Ceramic Society, 1994. **77**(10): p. 2518-2522.
43. Cao, J.J., et al., *In situ toughened silicon carbide with Al-B-C additions*. Journal of the American Ceramic Society, 1996. **79**(2): p. 461-9.
44. Becher, P.F., et al., *Microstructural design of silicon nitride with improved fracture toughness: I, Effects of grain size and shape*. Journal of the American Ceramic Society, 1998. **81**(11): p. 2821-2830.
45. Lathabai, S., J. Rödel, and B. Lawn, *Cyclic fatigue from frictional degradation at bridging grains in alumina*. Journal of the American Ceramic Society, 1991. **74**(6): p. 1348-1360.
46. Gilbert, C.J., R.H. Dauskardt, and R.O. Ritchie, *Behavior of cyclic fatigue cracks in monolithic silicon nitride*. Journal of the American Ceramic Society, 1995. **78**: p. 2291-2300.
47. Kruzic, J.J., R.M. Cannon, and R.O. Ritchie, *Crack size effects on cyclic and monotonic crack growth in polycrystalline alumina: Quantification of the role of grain bridging*. Journal of the American Ceramic Society, 2004. **87**(1): p. 93-103.
48. Gilbert, C.J., et al., *Cyclic fatigue in monolithic alumina: mechanisms for crack advance promoted by frictional wear of grain bridges*. Journal of Materials Science, 1995. **30**(3): p. 643-654.

49. Gilbert, C.J., et al., *Cyclic fatigue and resistance-curve behavior of an in situ toughened silicon carbide with Al-B-C additions*. Acta Metallurgica et Materialia, 1996. **44**(8): p. 3199-3214.
50. O'Brien, M.J., N. Presser, and E.Y. Robinson, *Failure analysis of three Si₃N₄ balls used in hybrid bearings*. Engineering Failure Analysis, 2003. **10**(4): p. 453-473.
51. Okazaki, M., A.J. McEvily, and T. Tanaka, *On the mechanism of fatigue crack growth in silicon nitride*. Metallurgical Transactions, 1991. **22A**: p. 1425-1434.
52. Choi, G., S. Horibe, and Y. Kawabe, *Cyclic Fatigue in Silicon-Nitride Ceramics*. Acta Metallurgica et Materialia, 1994. **42**(4): p. 1407-1412.
53. Choi, G., *Cyclic fatigue crack growth in silicon nitride: Influences of stress ratio and crack closure*. Acta Metallurgica et Materialia, 1995. **43**(4): p. 1489-1494.
54. Jacobs, D.S. and I.-W. Chen, *Mechanical and environmental factors in the cyclic and static fatigue of silicon nitride*. Journal of the American Ceramic Society, 1994. **77**(5): p. 1153-1161.
55. Fünfschilling, S., et al., *Mechanisms of toughening in silicon nitrides: Roles of crack bridging and microstructure*. Acta Materialia, 2011. **59**(10): p. 3978-3989.
56. Kovalev, S., et al., *Numerical evaluation of toughening by crack-face grain interlocking in self-reinforced ceramics*. Journal of the American Ceramic Society, 2000. **83**(4): p. 817-824.
57. Satet, R.L. and M.J. Hoffmann, *Influence of the rare-earth element on the mechanical properties of RE-Mg bearing silicon nitride*. Journal of the American Ceramic Society, 2005. **88**(9): p. 2485-2490.
58. *ASTM Standard E647, 2008e1, Standard Test Method for Measurement of Fatigue Crack Growth Rates*, 2008, ASTM International, West Conshohocken, Pennsylvania, USA. p. DOI: 10.1520/E0647-08E01, www.astm.org.
59. Fett, T., et al., *R-Curve Determination for the Initial Stage of Crack Extension in Si₃N₄*. Journal of the American Ceramic Society, 2008. **91**(11): p. 3638-3642.
60. Fünfschilling, S., et al., *Bridging stresses from R-curves of silicon nitrides*. Journal of Materials Science, 2009. **44**(14): p. 3900-3904.
61. Maxwell, D.C., *Strain based compliance method for determining crack length for a C(T) specimen*, 1987, Air Force Wright Aeronautical Laboratories.
62. Gilbert, C.J. and R.O. Ritchie, *Mechanisms of cyclic fatigue-crack propagation in a fine-grained alumina ceramic: the role of crack closure*. Fatigue & Fracture of Engineering Materials & Structures, 1997. **20**(10): p. 1453-1466.
63. Yuan, R., et al., *Ambient to high-temperature fracture toughness and cyclic fatigue behavior in Al-containing silicon carbide ceramics*. Acta Materialia, 2003. **51**(20): p. 6477-6491.
64. Foulk, J.W., et al., *A micromechanical basis for partitioning the evolution of grain bridging in brittle materials*. Journal of the Mechanics and Physics of Solids, 2007. **55**(4): p. 719-743.

65. Kruzic, J.J., et al., *The utility of R-curves for understanding fracture toughness-strength relations in bridging ceramics*. Journal of the American Ceramic Society, 2008. **91**(6): p. 1986-1994.
66. Kruzic, J.J., R.M. Cannon, and R.O. Ritchie, *Effects of moisture on grain-boundary strength, fracture and fatigue properties of alumina*. Journal of the American Ceramic Society, 2005. **88**(8): p. 2236-2245.
67. Gallops, S., T. Fett, and J.J. Kruzic, *Fatigue threshold R-curve behavior of grain bridging ceramics: Role of grain size and grain boundary adhesion*. Journal of the American Ceramic Society, 2011. **94**(8): p. 2556-2561.
68. Marshall, D.B., B.N. Cox, and A.G. Evans, *The Mechanics of Matrix Cracking in Brittle-Matrix Fiber Composites*. Acta Metallurgica, 1985. **33**(11): p. 2013-2021.
69. Nairn, J.A., et al., *Longitudinal Splitting in Epoxy and K-Polymer Composites - Shear Lag Analysis Including the Effect of Fiber Bridging*. Journal of Composite Materials, 1991. **25**(9): p. 1086-1107.
70. Bloyer, D.R., K.T. Venkateswara Rao, and R.O. Ritchie, *Fracture toughness and R-curve behavior of laminated brittle-matrix composites*. Metallurgical and Materials Transactions, 1998. **29A**: p. 2483-2496.
71. Bennison, S.J. and B.R. Lawn, *Role of interfacial grain-bridging sliding friction in the crack-resistance and strength properties of nontransforming ceramics*. Acta Metallurgica, 1989. **37**(10): p. 2659-2671.
72. Campbell, J.P., K.T. Venkateswara Rao, and R.O. Ritchie, *The effect of microstructure on fracture toughness and fatigue-crack growth behavior in γ -based titanium aluminide intermetallics*. Metallurgical and Materials Transactions, 1999. **30A**: p. 563-577.
73. Kruzic, J.J., J.H. Schneibel, and R.O. Ritchie, *Ambient- to elevated-temperature fracture and fatigue properties of Mo-Si-B Alloys: Role of microstructure*. Metallurgical and Materials Transactions, 2005. **36A**(9): p. 2393-2402.
74. Kruzic, J.J., et al., *Crack blunting, crack bridging and resistance-curve fracture mechanics in dentin: Effect of hydration*. Biomaterials, 2003. **24**(28): p. 5209-5221.
75. Nalla, R.K., et al., *Mechanistic aspects of fracture and R-curve behavior of human cortical bone*. Biomaterials, 2005. **26**(2): p. 217-231.
76. Foote, R.M.L., Y.W. Mai, and B. Cotterell, *Crack-Growth Resistance Curves in Strain-Softening Materials*. Journal of the Mechanics and Physics of Solids, 1986. **34**(6): p. 593-607.
77. Raddatz, O., G.A. Schneider, and N. Claussen, *Modelling of R-curve behaviour in ceramic/metal composites*. Acta Materialia, 1998. **46**(18): p. 6381-6395.
78. Fett, T., et al., *Evaluation of bridging parameters in alumina from R-curves by use of the fracture mechanical weight function*. Journal of the American Ceramic Society, 1995. **78**(4): p. 949-951.

79. Fett, T., et al., *Different R-Curves for Two- and Three-Dimensional Cracks*. International Journal of Fracture, 2008. **153**(2): p. 153-159.
80. Hu, X.Z., E.H. Lutz, and M.V. Swain, *Crack-Tip-Bridging Stresses in Ceramic Materials*. Journal of the American Ceramic Society, 1991. **74**(8): p. 1828-1832.
81. Hu, X.Z. and Y.W. Mai, *Crack-Bridging Analysis for Alumina Ceramics under Monotonic and Cyclic Loading*. Journal of the American Ceramic Society, 1992. **75**(4): p. 848-853.
82. Walls, D.P. and F.W. Zok, *Interfacial Fatigue in a Fiber-Reinforced Metal-Matrix Composite*. Acta Metallurgica Et Materialia, 1994. **42**(8): p. 2675-2681.
83. Geraghty, R.D., J.C. Hay, and K.W. White, *Fatigue degradation of the crack wake zone in monolithic alumina*. Acta Materialia, 1999. **47**(4): p. 1345-1353.
84. Hay, J.C. and K.W. White, *Grain-Bridging Mechanisms in Monolithic Alumina and Spinel*. Journal of the American Ceramic Society, 1993. **76**(7): p. 1849-1854.
85. White, K.W. and J.C. Hay, *Effect of Thermoelastic Anisotropy on the R-Curve Behavior of Monolithic Alumina*. Journal of the American Ceramic Society, 1994. **77**(9): p. 2283-2288.
86. Fett, T., *Evaluation of the bridging relation from crack-opening-displacement measurements by use of the weight function*. Journal of the American Ceramic Society, 1995. **78**(4): p. 945-948.
87. Fett, T., *Determination of Bridging Stresses and R-Curves from Load-Displacement Curves*. Engineering Fracture Mechanics, 1995. **52**(5): p. 803-810.
88. Fünfschilling, S., et al., *First- and second-order approaches for the direct determination of bridging stresses from R-curves*. Journal of the European Ceramic Society, 2010. **30**(6): p. 1229-1236.
89. Fett, T., et al., *Bridging stresses in sintered reaction-bonded Si₃N₄ from COD measurements*. Journal of the European Ceramic Society, 2005. **25**(1): p. 29-36.
90. Gilbert, C.J. and R.O. Ritchie, *On the quantification of bridging tractions during subcritical crack growth under monotonic and cyclic fatigue loading in a grain-bridging silicon carbide ceramic*. Acta Materialia, 1998. **46**(2): p. 609-616.
91. Pezzotti, G., et al., *In-situ determination of bridging stresses in Al₂O₃/Al₂O₃-platelet composites by fluorescence spectroscopy*. Journal of the European Ceramic Society, 1999. **19**(5): p. 601-608.
92. Sorensen, L., et al., *Bridging tractions in mode I delamination: Measurements and simulations*. Composites Science and Technology, 2008. **68**(12): p. 2350-2358.
93. Studer, M., K. Peters, and J. Botsis, *Method for determination of crack bridging parameters using long optical fiber Bragg grating sensors*. Composites Part B-Engineering, 2003. **34**(4): p. 347-359.

94. Fett, T., et al., *Bridging stress determination by evaluation of the R-curve*. Journal of the European Ceramic Society, 2000. **20**(12): p. 2143-2148.
95. Buchanan, D.J., R. John, and D.A. Johnson, *Determination of crack bridging stresses from crack opening displacement profiles*. International Journal of Fracture, 1997. **87**(2): p. 101-117.
96. Cox, B.N. and D.B. Marshall, *The Determination of Crack Bridging Forces*. International Journal of Fracture, 1991. **49**(3): p. 159-176.
97. He, J. and D.R. Clarke, *Determination of the piezospectroscopic coefficients for chromium-doped sapphire*. Journal of the American Ceramic Society, 1995. **78**(5): p. 1347-1353.
98. Dauskardt, R.H. and J.W. Ager, *Quantitative stress mapping in alumina composites by optical fluorescence imaging*. Acta Materialia, 1996. **44**(2): p. 625-641.
99. Pezzotti, G., et al., *In situ measurements of frictional bridging stresses in alumina using fluorescence spectroscopy*. Journal of the American Ceramic Society, 1998. **81**(1): p. 187-192.
100. Belnap, J.D. and D.K. Shetty, *Micromechanics of crack bridging in sapphire epoxy composites*. Composites Science and Technology, 1998. **58**(11): p. 1763-1773.
101. Pezzotti, G., et al., *Measurement of microscopic bridging stresses in an alumina molybdenum composite by in situ fluorescence spectroscopy*. Journal of the American Ceramic Society, 1999. **82**(5): p. 1257-1262.
102. Belnap, J.D. and D.K. Shetty, *Interfacial properties of sapphire/epoxy composites: Comparison of fluorescence spectroscopy and fiber push-in techniques*. Composites Science and Technology, 2005. **65**(11-12): p. 1851-1860.
103. Bennett, J.A. and R.J. Young, *A strength based criterion for the prediction of stable fibre crack-bridging*. Composites Science and Technology, 2008. **68**(6): p. 1282-1296.
104. Pezzotti, G., *In situ study of fracture mechanisms in advanced ceramics using fluorescence and Raman microprobe spectroscopy*. Journal of Raman Spectroscopy, 1999. **30**: p. 867-875.
105. Pezzotti, G., et al., *Raman microprobe evaluation of bridging stresses in highly anisotropic silicon nitride*. Journal of the American Ceramic Society, 2001. **84**(8): p. 1785-1790.
106. Dassios, K.G., et al., *Direct in situ measurements of bridging stresses in CFCCs*. Acta Materialia, 2003. **51**(18): p. 5359-5373.
107. Pezzotti, G. and S. Sakakura, *Study of the toughening mechanisms in bone and biomimetic hydroxyapatite materials using Raman microprobe spectroscopy*. Journal of Biomedical Materials Research, 2003. **65A**(2): p. 229-236.
108. Preuss, M., et al., *Measurements of fibre bridging during fatigue crack growth in Ti/SiC fibre metal matrix composites*. Acta Materialia, 2003. **51**(4): p. 1045-1057.

109. Fett, T. and D. Munz, *Stress Intensity Factors and Weight Functions* 1997: Computational Mechanics Publications, Southampton, UK. 408.
110. Fünfschilling, S., et al., *Determination of the crack-tip toughness in silicon nitride ceramics*. Journal of Materials Science, 2009. **44**(1): p. 335-338.
111. ASTM, *ASTM E647 – 08 - Standard Test Method for Measurement of Fatigue Crack Growth Rates*, in *Annual Book of ASTM Standards, Vol. 03.01: Metals-Mechanical Testing; Elevated and Low-temperature Tests; Metallography* 2010, ASTM International, West Conshohocken, Pennsylvania, USA. p. DOI: 10.1520/E0647-08E01
112. Deans, W.F. and C.E. Richards, *A simple and sensitive method of monitoring crack and load in compact fracture mechanics specimens using strain gages*. Journal of Testing and Evaluation, 1979. **7**(3): p. 147-154.
113. Dowling, N.E., *Notched member fatigue life predictions combining crack initiation and propagation*. Fatigue of Engineering Materials and Structures, 1979. **2**: p. 129-138.
114. Palazotto, A.N. and J.G. Mercer, *Crack considerations in a notched compact tension specimen*. Engineering Fracture Mechanics, 1990. **37**(3): p. 473-492.
115. Sternberg, S.R., *Biomedical Image Processing*. Computer, 1983. **16**(1): p. 22-34.
116. Fett, T., G. Rizzi, and D. Munz, *T-stress solution for DCDC specimens*. Engineering Fracture Mechanics, 2005. **72**(1): p. 145-149.
117. Fett, T., *Stress intensity factors, T-stresses, weight functions*. Vol. IKM50. 2008: Universitätsverlag Karlsruhe, Karlsruhe. 362.
118. Fett, T. and D. Munz, *Influence of narrow starter notches on the initial crack growth resistance curve of ceramics*. Archive of Applied Mechanics, 2006. **76**(11-12): p. 667-679.
119. Pippan, R., et al., *Fatigue threshold and crack propagation in γ -TiAl sheets*. Intermetallics, 2001. **9**(1): p. 89-96.
120. Gilbert, C.J., R.H. Dauskardt, and R.O. Ritchie, *Microstructural mechanisms of cyclic fatigue-crack propagation in grain-bridging ceramics*. Ceramics International, 1997. **23**(5): p. 413-418.
121. Munz, D., *What Can We Learn from R-Curve Measurements?* Journal of the American Ceramic Society, 2007. **90**(1): p. 1-15.
122. Ogasawara, T., N. Hirosaki, and Y. Akimune, *Statistical Analysis of the Fatigue Life Distribution of Monolithic Silicon Nitride*. Journal of the American Ceramic Society, 1994. **77**(2): p. 514-518.
123. Choi, G. and S. Horibe, *The Evaluation of Cyclic Fatigue Crack Growth Rate by Stress Intensity/Life Test in Silicon Nitride*. Journal of Materials Science Letters, 1998. **17**(10): p. 797-799.
124. *Standard test methods for determination of fracture toughness of advance ceramics at ambient temperature*, 2010, ASTM International: West Conshohocken, PA.
125. Lube, T., et al., *A Residual Stress Intensity Factor Solution for Knoop Indentation Cracks*. International Journal of Fracture, 2012. **175**(1): p. 65-71.

126. Newman Jr, J.C. and I.S. Raju, *An empirical stress-intensity factor equation for the surface crack*. Engineering Fracture Mechanics, 1981. **15**(1–2): p. 185-192.
127. Kruzic, J.J., R.M. Cannon, and R.O. Ritchie, *Effects of Moisture on Grain-Boundary Strength, Fracture, and Fatigue Properties of Alumina*. Journal of the American Ceramic Society, 2005. **88**(8): p. 2236-2245.